Title

Evaluation of Type I Hot Corrosion Resistance of Marinized Materials Through Low Velocity Burner Rig Testing

Author

Soto Leytan, Kliah Natalia

Publication Date

2019

UNIVERSITY OF CALIFORNIA,
IRVINE

Evaluation of Type I Hot Corrosion Resistance of Marinized Materials Through Low Velocity Burner Rig Testing

DISSERTATION

submitted in partial satisfaction of the requirements
for the degree of

DOCTOR OF PHILOSOPHY

in Materials Science and Engineering

by

Kliah Natalia Soto Leytan

Dissertation Committee:
Professor Daniel Mumm, Chair
Professor Julie Schoenung
Associate Professor Lorenzo Valdevit

2019

DEDICATION

To

My dad who has been my inspiration throughout my life,

My entire family who have made it possible for me to pursue my dreams,

John for bringing happiness and joy to my life,

My friends and lab mates for countless hours of help and support,

Would not have made it without you.

“Cuando quieres algo, todo el universo conspira para que realices tu deseo” – Paulo Coelho

TABLE OF CONTENTS

LIST OF FIGURES

LIST OF TABLES

Page

LIST OF EQUATIONS

Page

ACKNOWLEDGMENTS

I would like to express the deepest appreciation to my advisor and committee chair, Professor Daniel R. Mumm, who has been not only a great research advisor, but also an advocate for me and my career goals. Thank you for providing me with the tools to become a better a scientist. Working with you I have learned not only about hot corrosion, but also about compassion. I am infinitely thankful to have had an advisor that I could look up to and respect. Thank you for everything!

I would also like to thank my committee members, Professor Julie Schoenung, Professor Lorenzo Valdevit, Professor Vince McDonell, and Professor AJ Shaka for taking the time to sit through my degree examinations and for their insightful feedback.

I want to acknowledge and thank our collaborators, Professor Vince McDonell and Max Venaas, at the Advanced Power and Energy Program (APEP) at UCI for their contribution to this research. They provided invaluable combustion expertise, countless hours of burner rig upkeep and maintenance, and helpful insight with regards to burner rig improvements.

A very special thank you to my friends and lab mates who inspired me, helped me, challenged me, and ultimately pushed me to the finish line. Kara Phillips Bridges for all the help support and entertainment in the lab, and for your unconditional friendship. Kenta Ohtaki for all your help with materials characterization and sample preparation, and for always keeping things fun in the office. Maryam Zahiri Azar for all the TEM work. Everyone in the Mumm Lab: Madhura Basu Majumder, Amir Saeidi, Tim Montalbano, Kyle McDevitt, and Joberto Lee. A special thanks to my undergraduate students Kunthea Deng and Phuong Nguyen for their amazing work ethic.

In addition, I would like to thank everyone at UCI who helped me through my degree. Thank you to the staff at the Irvine Materials Research Institute for their guidance and help with materials characterization. Thank you to the staff in the materials science and engineering department for always being welcoming, friendly, and helpful. A special thanks to Yi-San for all the amazing work she does! Thank you to the ChAMP program for an amazing opportunity.

I thank our program manager Dr. Dave Shifler of the Office of Naval Research for funding this multi-year program that allowed me to pursue my PhD (ONR Award N00014-14-1-0637). I thank Dr. Lou Aprigliano for sharing his knowledge in the field, and our industry collaborators, Rolls Royce, for providing samples for evaluation. I thank the Department of Materials Science at University of California, Irvine and the Schlumberger Foundation for providing additional funding.

CURRICULUM VITAE

EDUCATION

University of California, Irvine (UCI) Irvine, CA
Ph.D. Materials Science and Engineering 2019
Thesis: "Evaluation of Type I Hot Corrosion Resistance of Marinized Materials Through Low Velocity Burner Rig Testing"
Advisor: Prof. Daniel R. Mumm
M.S. Materials Science and Engineering 2014

Occidental College Los Angeles, CA
B.A. Physics and Mathematics 2012

FELLOWSHIPS & AWARDS

Schlumberger Foundation Faculty for the Future Award	2015-2016
Miguel Velez Scholarship	2015
AGS Travel Grant, University of California Irvine	2015
Gordon Research Conference Student Stipend	2014
Graduate Student Fellowship, University of California Irvine	2013-2014

PEER REVIEWED PUBLICATIONS

- McDonell, V; Zhao, Y.; Soto Leytan, K; Samuelsen, S; *Investigation of Hydrogen-Air Research Flame Color Emission,* International Journey of Hydrogen Energy, SUBMITTED FOR REVIEW

PRESENTATIONS

- Presentation: *Evaluation of Type I Hot Corrosion Resistance of Marinized Materials through Low Velocity Burner Rig Testing* – TMS 2018, Phoenix Arizona
- Poster: *Effect of Fuel Content on Type I Hot Corrosion Attack in Low Velocity Burner Rig and Development of an Automated Image Analysis Sample Assessment Protocol for Evaluating Extent of Attack* – High Temperature Corrosion and Protection of Materials 2016, Les Embiez, France.
- Presentation: *Automated Image Analysis for Determining the Extent of Hot Corrosion Attack in Evaluating Potential "Marinized" Turbine Hot Section Materials* – MS&T 2015, Columbus OH.
- Poster: *Low Velocity Burner Rig Study of Hot Corrosion in Turbine Components* – Gordon Research Conference 2015, New London, NH.
- Poster: *Automated Image Analysis Sample Assessment Protocol for Evaluating Extent of Hot Corrosion Attack in Burner Rig Tests* – Faculty for the Future Forum 2015, Boston MA.
- Poster: *Hot Corrosion of Shipboard Turbine Components in a Low Velocity Burner Rig Using Alternative Fuels* – Solid State Studies of Ceramics, Gordon Research Conference, South Hadley, MA, 2014.

LEADERSHIP

UCI Mumm Laboratory Safety Representative 2014-2016, 2018-2019
- Responsible for ensuring up to date standard operating procedures, chemical inventory and waste management, as well as the ongoing training of new students in the lab.

TEACHING

ASM Materials Camp 2018 July 2018

- Helped organize and supervise a one-week summer camp for high school students.

Principles of Materials Science and Engineering (ENGR 54) Fall 2016, 2017

- Assisted professor in introductory course on materials science and engineering, mainly in grading assignments, teaching weekly discussion sessions, and holding weekly office hours.

Solar Cup 2009-2012, 2014

- Helped organize Solar Cup, an event put up by the metropolitan water district of southern California, where high schools form teams and build a boat that runs on solar power. This is a yearlong process that culminates with a competition at Temecula, CA.
    - Previous to the competition: Provide workshops and school visits in order to help the participating high schools succeed in the boat building process.
    - During the competition: Provide safety checks for mechanical and electrical components of the boats before competing in the water.

ABSTRACT OF THE DISSERTATION

Evaluation of Type I Hot Corrosion Resistance of Marinized Materials Through Low Velocity Burner Rig Testing

By: Kliah Soto Leytan
Doctor of Philosophy in Materials Science and Engineering
University of California, Irvine, 2019
Professor Daniel Mumm, Chair

With utilization of gas turbine engines in power generation, aerospace and marine propulsion applications, the materials that enable those gas turbine technologies are exposed to a wide range of service temperatures and material exposure environments resulting in application dependent degradation modes. The most severe types of degradation are seen in the hottest section of the turbine with its combined interaction of external contaminants and high temperatures. Although specialized coatings have been developed to try to alleviate the degradation experienced, hot corrosion continues to be a concerning, life-limiting factor, particularly in the case of marine turbines, and it is, therefore, the focus of this study. This work presents the evaluation of new candidate materials for improved marine turbine performance at higher operating temperatures. Three different areas of work are discussed. First, the current methodology for the evaluation of hot corrosion attack in pin-shaped samples, typical of burner rig testing, is presented, and its shortcomings are discussed. A new sample assessment protocol

based on image analysis was established and validated. Next, a new nickel-based superalloy and three doped variations, intended to replace current blade and vane substrates, were evaluated under type I hot corrosion conditions in a low-velocity burner rig (LVBR). The tests included both long-term and short-term exposures as well as pre-oxidized and bare materials. Scanning electron microscopy and energy dispersive spectroscopy were used to study the attack mechanisms as a function of doping material and concentration.

It was found that different dopants affected the hot corrosion resistance by promoting the incorporation of certain elements, which changed the types of sulfides and oxides, protective or non-protective, that formed. Silicon was found to be an effective dopant at increasing hot corrosion resistance through two mechanisms: a) by promoting chromia formation and suppressing the activity of titanium, resulting in a more protective oxide able to slow down internal sulfidation, and b) by promoting a different coarsening behavior of the internal sulfides. Co-doping with hafnium and silicon had a synergistic effect where the presence of hafnium enhanced the effects of silicon, and the overall hot corrosion resistance was significantly improved, even though hafnium doping, by itself, had poor performance.

The third area of work is focused on the performance, compatibility, and hot corrosion resistance of substrate-coating material pairs evaluated in a LVBR. The coatings that were evaluated included several commercially available diffusion coatings, and both commercially available and new developmental candidate overlay coatings. In the case of diffusion coatings, it was observed that the formation of topologically closed pack (TCP) phases and elemental segregation along the interdiffusion zone (IDZ) are crucial, limiting factors determining the lifespan of the coating. In the case of overlay coatings, initial observations provided evidence for substrate-dependent performance. However, upon closer inspection, it was revealed that this

dependence was a function of differing initial microstructures most likely originating in processing variations. The best performing coatings, evaluated on multiple substrates, were comprised of a modified NiCrAlY and a platinum modified CoCrAlY. As a direct result of this work, new substrate and coating materials with enhanced performance were selected for implementation in the next generation of marine turbine engines, and the testing and sample evaluation framework developed will continue to guide future material selection efforts. The study of commercially processed substrates and coatings led to key findings pointing to the importance of coating microstructure control and prevention of unwanted phase formation and elemental segregation.

CHAPTER 1: Introduction

1.1 Motivation

Current technology takes advantage of the high temperature strength and toughness of nickel-based superalloys, which are utilized in most components in the hot sections of turbine engines. In order to preserve the integrity of the engine and protect the nickel-based parts from harsh environments, protective coatings have been put in place. However, increased pollution levels and the need to operate gas turbine engines in varying environments have led to accelerated degradation mechanisms affecting turbine materials. A specifically harsh mechanism is hot corrosion, which is a degradation mechanism characteristic of salty (marine) environments. The presence of salt and high temperature prompts a process in which molten salt infiltrates metal coatings and/or substrates and causes a series of reactions that result in material loss, sulfidation, deep penetration of salt constituents into the metal, and ultimately mechanical failure. Sulfate salts of sodium, calcium, and potassium, as well as vanadates and carbonates have all been shown to cause hot corrosion in superalloys. However, in marine gas turbines the most common deposit is Na_2SO_4. The source of this deposit can vary, as sodium and sulfur can be present in the fuel as impurities, or NaCl and/or sulfates can be ingested through the turbine intake air [1].

Hot corrosion in turbine engines affects the world’s economy, security, and energy efficiency, and yet the state-of-the-art technology is still based upon empirical research that is decades old. According to a 2013 Department of Defense report, corrosion related spending is estimated to be \$20.8 billion annually [2]. The Navy alone spends \$6.14 billion annually in corrosion related maintenance and, according to the 2008 naval board of inspection and survey report, the number one issue encountered in ships is corrosion control [3].

The hot corrosion of turbine parts and its impact on marine propulsion and power generation have been a severe problem for over 90 years [4-6]. Current protective coatings offer some relief against hot corrosion, but the inevitable infiltration of salt through the coating and into the substrate compromises the functionality of the engine hardware. Continuous testing and evaluation of new materials is required due to the constant need for higher energy efficiency and therefore, higher operating temperatures within turbines, which will only exacerbate the already existing degradation problems. Consequently, it is imperative to continue the advancement of hot corrosion prevention technology. One of the biggest challenges when studying new materials for turbine applications is that of reproducing the exact environment within gas turbines engines. The most accurate experimental test protocols are based on burner rig systems, as they most closely reproduce (in a laboratory environment) the actual gas turbine environments by exposing samples to: a) combustion by-products of shipboard and aero-turbine fuels, b) constant flow of contaminants, such as salt water, and c) thermal-cycling aimed to reproduce engine cycles [7].

1.2 Background

1.2.1 Turbine Engines

Gas turbine engines are used in a wide variety of applications, from powering the vast majority of commercial and military aircraft as well as military naval fleets to their use in power generation plants. A cross-section of a Pratt and Whitney turbine engine [8] is shown in Figure 1, from left to right, the stages of a turbine engine are [9]:

a. The inlet where outside air is guided to the next stage.

b. The compressor is comprised of alternating rows of stationary and rotating blades called stators and rotors along the shaft. Air flows along the direction of the shaft, and in modern axial-flow compressors, it can be compressed to 24 times its initial pressure. Compressed air is then guided to the next stage.

c. The combustor is where the compressed air is mixed with fuel and burned. Fuel is atomized and introduced into the combustor through spray nozzles, and an electric igniter is used to begin combustion, which raises the temperature of the gases. These high-temperature, high-pressure gases flow from the combustor to the next stage.

d. The turbine is comprised of alternating stator and rotor rows. The hot gases leave the combustor and pass through the turbine where they are partially expanded. The turbine is responsible for turning the shaft that drives the compressor, it also powers the fuel pump and other accessories. The turbine shaft can be attached to a generator or used for propulsion, depending on the application.

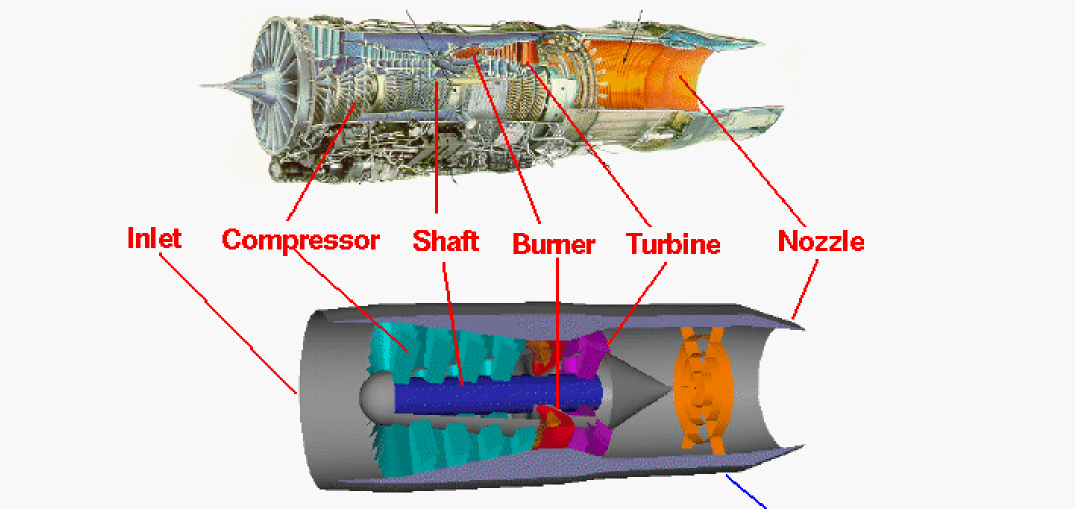

FIGURE 1. Pratt and Whitney turbine engine: Image and computer drawing of the inside of a jet engine highlighting the different stages [8].

1.2.1.1 Degradation in Turbine Engines

Gas turbines are used in a wide variety of applications having different temperature requirements as well as different environments. As such, different types of turbines experience distinct types of degradation and make use of specialized technology to try to alleviate some of this degradation. A summary of the differences in main degradation modes among different types of turbines is shown in Table 1 [10]. According to this data for turbines used in marine applications, hot corrosion is the number one concern regarding degradation of materials, and it will be the focus of this study.

TABLE 1. Comparison of degradation modes according to gas turbine application [10].

	Oxidation	**Hot Corrosion**	**Interdiffusion**	**Thermal Fatigue**
Aircraft Engines	Severe	Moderate	Severe	Severe
Land-based power generation	Moderate	Severe	Moderate	Light
Marine Engines	Moderate	Severe	Light	Moderate

1.2.1.1.1 Marine Turbine Environment

Turbine engines are very sensitive to the quality of the air around them due to the large amount that they consume (around 685 kg/s for the GE 9391G) [11]. Even though incoming air can often be cleaned by different filtering devices in power generation turbines, impurities in the air can find their way to the hot sections of the turbine. In the case of marine turbines, unfiltered air quality can contain up to 2,600 ppm of Na_2SO_4, 19,000 ppm of NaCl and other seawater-derived species that can further aggravate an already corrosive environment [12]. From the different filtering mechanisms, it is expected that the salt intake be reduced to around 10 ppm which, as shown by several studies [13-17], is enough for the turbine environment to be corrosive.

Another important factor in determining the environment within the turbine is of course the fuel used. Contaminants in the fuel affect both combustion efficiency as well as materials' lifetime [18]. It is therefore very important to ensure the use of fuel that is both high quality as well as consistent. The U.S. Navy ships use Marine Diesel which corresponds to NATO Specification F-76, or the U.S. equivalent MIL-F016884 [19,20], which specifies the maximum sulfur content to be 1.0 wt.%. This was recently reduced to 0.5 wt.% under MIL-F-16884L [21].

Although aero and power generation turbines can often operate at temperatures as high as 1200 °C [22, 9], marine turbines usually operate at lower temperatures. At full power the turbine can reach temperatures in the 900s °C, while it stays closer to 700 °C when idling [12].

1.2.2 Hot Corrosion

Hot corrosion is a deposit-induced accelerated oxidation [23, 24]. It is influenced by many factors, such as gas composition, deposit composition, metal/coating composition, amount of deposit, substrate microstructure, type of coating, gas velocity, geometry, erosion, temperature, etc. However, temperature is often used to classify hot corrosion into low temperature attack, or Type II hot corrosion, and high temperature attack, or Type I hot corrosion [25]. In both cases degradation is accelerated and therefore deviates from the established oxidation rate as a function of temperature, shown in Figure 2 [12].

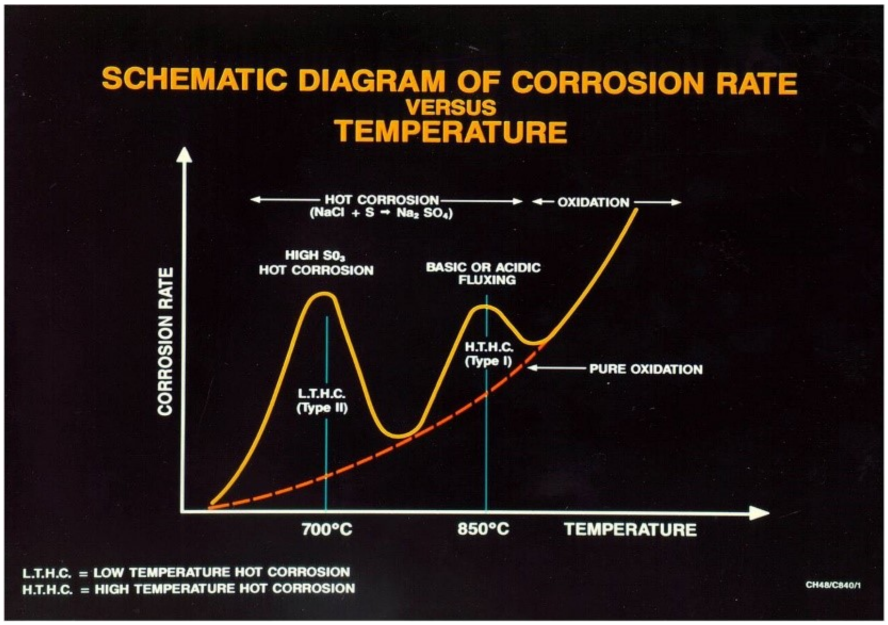

FIGURE 2. Schematic diagram of corrosion and oxidation rates as a function of temperature [12].

1.2.2.1 Type I Hot Corrosion

This type of attack is observed at temperatures above the melting point of Na_2SO_4, 884 °C, and is usually associated with 900 °C. At these higher temperatures, sodium sulfate is in liquid form and can deposit on the surfaces of turbine parts.

High temperature attack was observed in the 1960s in aircraft gas turbines with temperatures around 900 °C and mainly Na_2SO_4 deposits [28]. Due to the large presence of sulfides within the metal, this type of attack was also known as sulfidation [27]. Following the observation of this new phenomenon, Bornstein and DeCrescente set out to determine the role of sulfur in this type of attack and performed a series of experiments making use of alloy B-1900 [28, 29]. Through their studies they showed that when sulfur alone was present no hot corrosion attack took place. However, when the same amount of sulfur, this time in the form of Na_2SO_4, was present, significant hot corrosion attack followed. This observation led them to conclude that hot corrosion attack took place due to the presence of Na_2O which destroyed the protective oxide scale through the following fluxing reaction,

$$NiO + Na_2SO_4 \leftrightarrow 2Na^+ + NiO_2^{2-} + SO_3 \qquad (1)$$

Closer examination of this fluxing process done by Rapp and Goto [30] lead to a proposed mechanism where a negative solubility gradient across the molten deposit resulted in the oxide being dissolved at the oxide/salt interface (where solubility was at its highest), and later reprecipitated out in the deposit towards the salt/gas interface (where solubility was lower). Experiments carried out by Rapp were able to determine oxide solubilities as a function of the activity in Na_2O in the Na_2SO_4 deposit. Similar to how pH is used to describe aqueous solutions, the thin layer of molten Na_2SO_4 can be described by an acid-base chemistry as follows [31]

$$Na_2O + SO_3(g) = Na_2SO_4; \quad \log k\ (1200K) = -16.7 \qquad (2)$$

And therefore,

$$\log a_{Na_2O} + \log a_{SO_3} = -16.7 \qquad (3)$$

where a stands for the activity of each species.

The first term of equation (3) is a quantitative measure of the melt basicity, while the second term indicates the acidity. Figure 3 shows the solubility curves as a function of the melt's basicity that were obtained by Rapp [32-35].

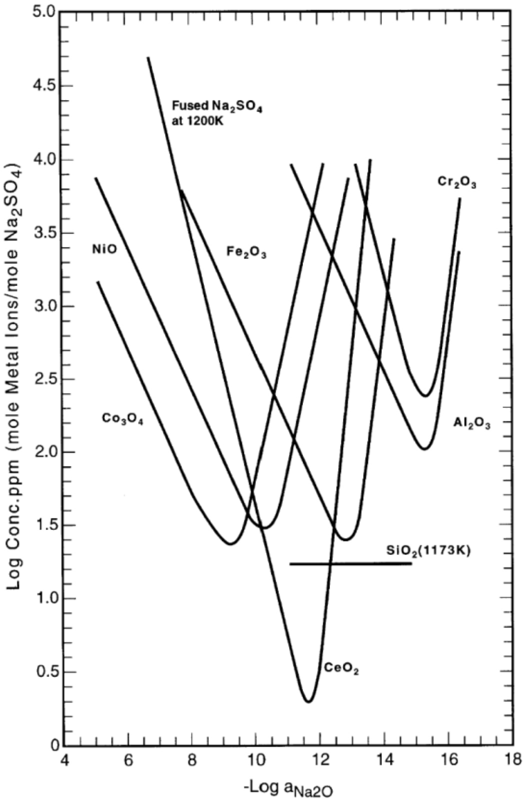

FIGURE 3. Compilation of measured solubilities for several oxides in fused pure Na_2SO_4 at 1200 K obtained by Rapp [32-35].

Looking for an explanation to the increase in melt basicity and finding that Na_2SO_4 did not decompose fast enough in air or oxygen following equation (4), Goebel and Pettit proposed that the presence of a thin layer of molten Na_2SO_4 separating the protective oxide from the gas phase creates an oxygen gradient across the melt [24].

$$Na_2SO_4 = Na_2O + SO_3 \tag{4}$$

A direct result of this oxygen gradient is the increase of sulfur activity at the oxide/salt interface, making it possible for sulfur to penetrate the protective oxide scale and start the sulfidation of the metal alloy underneath. At the boundary of the oxide/salt interface, sulfur is leaving the melt to form metal sulfides, and oxygen is being utilized to oxidize the metal alloy as follows [25]:

$$Na_2SO_4 = Na_2O \text{ (in } Na_2SO_4\text{)} + \frac{3}{2}O_2 \text{ (to form oxide layer)} + \frac{1}{2}S_2 \text{ (to form metal sulfide)} \qquad (5)$$

According to equation (5), the basicity of the melt is highest at the oxide/salt interface, and it decreases towards the salt/gas interface. Because the dissolution of the protective oxide happens under basic conditions [36], this basicity gradient also corresponds to an oxide solubility gradient which dictates that the oxide layer wants to dissolve at the oxide/salt interface and later reprecipitate (as non-protective oxide precipitates) near the salt/gas interface.

Therefore, type I hot corrosion can be thought of as an oxidation/sulfidation process that occurs through basic fluxing and dissolution of the protective oxide scale by molten sulfate deposits. It is characterized by extensive internal sulfidation, non-protective porous oxides dispersed in the salt, and even uniform attack. Furthermore, even though the exact role of sulfur in the gas phase is not well understood, it is accepted that the driving force behind type I is not the gas phase, but the interaction of the metal alloy and the molten Na_2SO_4 [12].

1.2.2.2 Type II Hot Corrosion

This type of attack is observed in the temperature range of 650 °C to 800 °C. It was first observed in the 1970s [37]. The proposed mechanism requires Na_2SO_4, which is still in solid form, to form a liquid solution of Na_2SO_4-MSO_4 (where M stands for Ni or Co, depending on the base metal) by converting oxides to sulfates through interaction with SO_3 from the combustion gas. [35, 38, 39] Attack is dependent on the formation of this low temperature eutectic and therefore requires a high partial pressure of SO_3 in the gas. The localized nature of this type of attack produces a very distinctive pitted morphology, where the pits correspond to the areas where the eutectic formed.

1.2.3 Materials

The extreme conditions within turbines require that its components be made of specialized materials capable of withstanding high temperature, while retaining mechanical strength, toughness, creep resistance, stability, and resistance to both oxidation and hot corrosion [40]. The need for this type of material is currently being filled by nickel-based superalloys and a series of highly specialized protective coatings.

1.2.3.1 Nickel-based Superalloys

Nickel-based superalloys are used not only in turbine engines, but also in other extreme environments such as power plants, chemical processing plants, and rocket engines.

In marine turbine engines, nickel-based superalloys are typically used in the turbine sections where the gas temperature reaches its highest point. The development of superalloy technology has led to alloys capable of withstanding average temperatures of 1050 °C with short exposures to temperatures as high as 1200 °C, which reaches about 90% of the material's melting point [41]. The different properties of nickel-based superalloys can be tailored by modifying both the composition and the microstructure of the alloy.

1.2.3.1.1 Microstructure

Nickel-based superalloys have a specific microstructure comprised of a matrix, called γ, and a coherently precipitating intermetallic phase, called γ', shown in Figure 4. The matrix γ, has an FCC nickel-based austenitic structure, while γ' has an ordered $L1_2$ structure and a Ni_3Al composition [40]. This γ – γ' microstructure slows down dislocation movement and increases creep resistance.

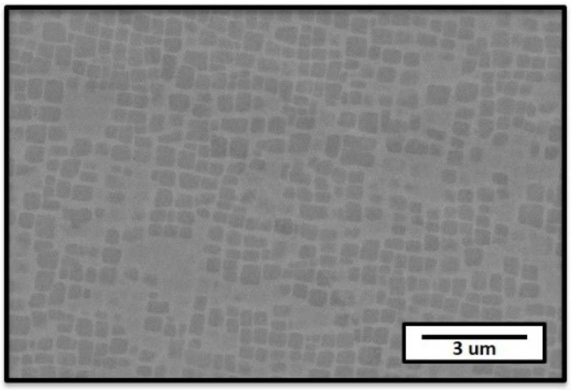

FIGURE 4. Backscattered SEM image showing typical γ – γ' microstructure of nickel-based superalloy. γ shown in light, while γ' is shown in dark.

Other phases that can be present in nickel-based superalloys include [42]:

a) Gamma double prime (γ") is a phase present in nickel-iron based alloys. It has a BCT structure and a composition of Ni_3Nb. This phase is used to strengthen nickel based superalloys at lower temperatures, and it is unstable above 650 °C.

b) Carbides are formed when carbon that is added in very small amounts (under 0.2 wt.%). It combines with reactive elements such as tantalum, titanium, hafnium or niobium, to form metal carbides. Carbides strengthen grain boundaries, reduce grain boundary sliding, and can tie up elements that can promote phase instability during service.

c) Borides are present when boron is added in small amounts to improve creep-rupture. Borides are hard particles that are observed at grain boundaries.

d) Topologically closed-packed phases (TCPs) are unwanted phases that can form either during heat treatment, or more commonly during service. They are composed of close-packed layers of atoms parallel to {1 1 1} planes of the γ matrix and appear as long plates or needles. Susceptibility to TCP phase formation increases with increasing levels of body-centered cubic transition metals such as tantalum, niobium, chromium, tungsten and molybdenum.

Other important microstructural features that can be observed in nickel-based superalloys include dendrites, dendritic segregation, and eutectic pools. During casting processes, the thermal conditions during solidification are critical to the final structure and properties of the material [42]. The primary and secondary arm spacings are controlled by the cooling rates, and therefore so is the segregation of the constituent alloying elements [40]. Dendritic segregation can have detrimental effects on grain defect formation during solidification, therefore heat treatment of cast alloys is aimed to homogenize the material and minimize these effects. However, depending on the composition of the alloy the level of homogeneity that can be achieved varies. As the last constituents to solidify, eutectic pools are often found in the interdendritic or intergranular regions. They typically contain γ'-formers, carbides, and borides.

1.2.3.1.2 Composition

Although γ-nickel is the major constituent in nickel-based superalloys, they can contain up to approximately 40 wt. % of other alloying elements. These elements are added to improve the performance of superalloys both mechanically as well as chemically. The elements in superalloys can be classified by whether they prefer to segregate to the γ matrix or the γ' precipitates as follows [43].

a. γ -matrix: nickel, chromium, cobalt, tungsten, molybdenum, rhenium
b. γ'-precipitates: aluminum, titanium, niobium, tantalum
c. minor alloying elements: hafnium, zirconium, boron, carbon

Hot corrosion resistance is achieved by the addition of chromium, while oxidation resistance is achieved by the addition of aluminum. Strengthening of the γ' phase is achieved by additions of titanium, tantalum and niobium, while strengthening of the γ matrix is achieved by additions of molybdenum, tungsten, niobium, and rhenium. For polycrystalline superalloys boron, carbon, hafnium, and zirconium can be added to strengthen grain boundaries [44].

1.2.3.1.3 Processing

Superalloys can be produced by three different processing routes: 1) casting, 2) powder processing, and 3) wrought processing. All three types of superalloy processing start with the fabrication of large ingots by vacuum induction melting (VIM) which acts as initial feedstock for all future processes [40].

1.2.3.1.3.1 Casting

Investment casting is the primary casting process for the fabrication of turbine components requiring complex shapes, this includes vanes and blades. Cast superalloys can be made in a wider range of compositions than wrought alloys.

In order to cast any part, an exact wax replica or pattern of the part must be produced. A ceramic mold is then fabricated by progressive buildup of ceramic layers around this mold. A heat treatment is used to remove the wax from the mold and the VIM ingot is remelted and poured into the mold in a pre-heated vacuum chamber. The single-used mold can be removed after the part has reached room temperatures. Different microstructures can be achieved through different casting processes. Equiaxed casting is the simplest type of casting as it solidifies uniformly throughout their volume. The resulting microstructure is polycrystalline with no preferred grain orientation. Different processes have been developed in order to create more complex structures, such as directionally solidified and single crystal alloys [45].

All cast superalloys are exposed to three heat treatment steps [42]:

i) Solution treating is performed with the goal of dissolving all the phases in the as cast microstructure and homogenizing the material. It is therefore performed at a temperature above the γ' solvus temperature.

ii) Stabilization heat treatment is meant to optimize the γ' size and morphology as well as to decompose the larger as-cast carbides into finer grain boundary carbides.

iii) The aging treatment is used to precipitate more γ' as fine precipitates.

1.2.3.1.3.1.1 Directionally Solidified

Pratt and Whitney Aircraft (PWA) pioneered the development of directionally solidified (DS) technology [46, 44]. Before DS technology, turbine blades were made as isotropic polycrystal or equiaxed castings. However, it was observed that component failure often occurred at the grain boundaries due to creep, thermal fatigue and/or oxidation. Therefore, PWA worked to enhance the creep-rupture resistance of nickel-based superalloys by orienting the grain boundaries parallel to the applied-stress direction. In order to do so, the dendrites must grow from one end of the casting to the other end. Consequently, a thermal gradient bounded by the liquidus and solidus temperatures of the alloy is established and passed through the casting. The rate is critical since it must be fast enough to avoid macro-segregation but also slow enough to avoid nucleation ahead of the solid-liquid interface.

1.2.3.1.3.1.2 Single Crystal

Aligning the grain boundaries resulted in great improvements to the mechanical properties of superalloys. Therefore, the next step in the improvement of superalloys was for PWA to completely remove grain boundaries from the microstructure. In the 1970s PWA showed that incorporation of grain boundary strengtheners such as boron, hafnium, zirconium, and carbon was causing lower incipient melting temperatures. Therefore, in single crystals the complete solutioning of the γ’ phase along with appreciable solutioning of the γ/γ’ eutectic phase was achieved without causing incipient melting of the alloy [47-49]. Consequently, single crystal alloy PWA 1480 achieved an increase of 25 to 50 °C in temperature capability when compared to commercially used DS alloys.

1.2.3.1.3.2 Powder Metallurgy

Powder techniques are used extensively in superalloy production, especially for high strength gas turbine disk alloys, which contain high levels of refractory elements such as tungsten, titanium, tantalum, molybdenum, and niobium. Increasing the amount of refractory elements can increase the alloy's strength, but it makes conventional processing routes impractical due to severe segregation within the ingot and susceptibility to cracking due to limited ductility.

During powder processing the VIM ingot is gas or vacuum atomized, and the resulting powders are collected. The powders are then consolidated by either extrusion or hot isostatic pressing (HIP). When HIP is used the alloy is heated to a temperature slightly below the γ' solvus under a hydrostatic pressure of up to 310 MPa [40]. When extrusion is used, the superalloy powder is hot extruded through dies subjecting the material to a thermomechanical process. Due to the presence of plastic deformation, the extruded temperatures must stay below γ' solvus temperature at all times. Some of the advantages of this process include minimal segregation, reduced inclusion sizes, and ability to use a composition high in γ'-formers [42]

1.2.3.1.3.3 Wrought

Wrought alloys are produced by first remelting the original VIM ingot. This is necessary due to the macro-segregation, and formation of shrinkage cavities that take place during the solidification of the VIM ingot. In order to avoid these problems during remelting, secondary melting processes, such as electro-slag remelting, electron beam cold hearth refining, and vacuum arc remelting, are used. Following remelting the deformation process can begin where hot-working is applied in order to refine the microstructure and yield isotropic properties. Parameters such as temperature, strain, strain rate, etc. all play a role in achieving the desired microstructure and properties [42].

1.2.3.2 Protective Coatings

Nickel based superalloys provide the high temperature mechanical properties necessary for turbine parts. However, their chemical stability and resistance to extreme corrosive environments is less than ideal [50]. Relying on one single material to provide both mechanical properties as well as protection against corrosion has thus far been proven impossible. Therefore, protective coatings, optimized for the specific environment that they will be exposed to, are often applied to turbine parts. In the case of marine turbines, this environment is one with high levels of sulfur and saltwater, which results in a highly corrosive environment.

To protect against this highly corrosive environment, there are different types of coatings, varying in both composition and application mode. The most commonly used are diffusion and overlay.

1.2.3.2.1 Diffusion Coatings

Diffusion coatings are produced by aluminum enrichment of the surface through diffusion [51]. The coating's basis is the intermetallic compound β-NiAl which possesses an ordered BCC or a B2 (space group Pm3m) structure [52]. β-NiAl can exist over a wide range of compositions at high temperatures. Its role is to act as a reservoir of aluminum and therefore promote the formation of a protective alumina scale during high temperature exposures.

Diffusion coatings can be applied through different methods, such as pack cementation, chemical vapor deposition, slurry coatings, electrophoretic deposition, etc. However, the most popular technique due to both its simplicity and cost effectiveness is pack cementation [53].

1.2.3.2.1.1 Pack Cementation Aluminide Coatings

This process requires that the parts to be coated be immersed in a powder mixture containing Al_2O_3, aluminum particles, and activators (ammonium halide). When this mixture is heated to temperatures above 800 °C, aluminum halides form and diffuse through the pack mixture and deposit aluminum metal on the substrate. One disadvantage of this process is that aluminide coatings need to be tailored to the specific substrate they will be applied to.

Within this type of aluminide coatings, two categories can be defined based on the activity of aluminum maintained at the surface of the substrate [53]:

a) In low activity or outward diffusion, the coating forms mainly through the outward diffusion of nickel and the resulting β-NiAl is nickel-rich.
b) In high activity or inward diffusion, the coating forms mainly through the inward diffusion of aluminum, and the resulting coating includes both Ni_2Al_3 and β-NiAl.

Throughout the years, there have been various attempts at improving the performance of aluminide coatings that have resulted in doped versions of these coatings such as, silicon-containing aluminides, chromized and chrome-aluminides, and platinum modified aluminide coatings. The most widely used is the Pt-modified aluminide, which increases hot corrosion resistance and oxide adhesion [54].

1.2.3.2.1.2 Slurry Coatings

This type of process was developed in the 1970s and 1980s, after the development of pack cementation [55, 56]. Slurry coatings can be applied through immersion, painting or spraying methods which makes them advantageous for large parts. The applied slurry contains a metal powder, an activator, and a binder [57, 58]. After coating application, a low temperature

(300-450 °C) heat treatment is necessary to burn out the binder. This is followed by a high temperature (600-1100 °C) heat treatment where the metal powder reacts and diffuses into the substrate forming the coating.

1.2.3.2.1.3 Electrophoretic Deposition Coatings

The Allison electrophoretic process (AEP) was developed by the Allison Engine Company (later acquired by Rolls Royce) in the 1980s [59]. The process relies on applying an electrical potential to two electrodes immersed in a dispersion of charged particles so that the particles can be deposited onto one of the electrodes. This process differs from electroplating in that it allows particles of any composition, rather than ions, to be deposited [60].

1.2.3.2.2 Overlay Coatings

Overlay coatings differ from aluminides in that they are much more versatile in two main respects: i) they allow for a wider variety of compositions, and ii) they allow for more independence from the substrate and don't need to be tailored for them [51].

Overlay coatings are also known as MCrAlY, where M can stand for Fe, Ni, Co, or both Ni, and Co. They contain at least 4 elements and therefore require different processing techniques than those used for aluminides, such as air plasma spray (APS), low pressure plasma spray (LPPS), and electron beam physical vapor deposition (EBPVD) [61, 62].

MCrAlY coatings have a two-phase microstructure of β+γ, where β acts as an aluminum reservoir during high temperature exposures, and γ improves thermal fatigue resistance by increasing ductility [63]. During turbine use, aluminum is depleted out of the β phase to form the thermally grown oxide (TGO) on the surface of the coating, and to the substrate by interdiffusion. The depletion of aluminum leads to the dissolution of β phase decreasing the overall volume fraction of the phase, which is often used to measure coating lifetime [64].

The composition of MCrAlY coatings is tailored to improve their application-specific performance. For marine turbines, the main constituent is nickel, cobalt, or both, with cobalt providing higher hot corrosion resistance. Overall, chromium provides corrosion and oxidation resistance, while aluminum is added in quantities around 10 wt.% to extend oxidation life [65]. Yttrium is added in small amounts to increase oxide adhesion, by preventing the segregation of sulfur to the oxide substrate interface [67]. Other elements have been found to have a positive effect on MCrAlY coatings as follows: tantalum has been shown to increase oxidation resistance, rhenium can improve cyclic oxidation and thermal-cycle fatigue, silicon can improve cyclic oxidation resistance, and hafnium plays a similar role to that of yttrium [66-68].

1.2.4 Low-Velocity Burner Rig

A crucial step to understanding hot corrosion is the ability to recreate it in a controlled lab setting. Given the extreme conditions within a turbine engine this is no easy task. The study of hot corrosion has evolved through the years, and the experimental setups currently in use can be rather complex [69-71]. However, the first observations were carried out in relatively simple systems. The most popular studies involve the use of the crucible test, the spray-on method, or burner rig facilities. The crucible test is one where the sample being investigated is completely submerged in a crucible containing the molten salts of interest (in this case Na_2SO_4) and held at high temperatures in a furnace for a set period of time [72]. The sample is then retrieved and characterized. Although this type of experiment was helpful in understanding the degradation taken place under molten salt attack, it was not representative of the environment within a turbine. Therefore, the obtained results could not easily be extrapolated to more application-based technologies. Consequently, new experimental setups were explored, and the spray-on method was developed [73]. In this test the sample being investigated was sprayed with a known amount of a salt solution and subsequently exposed to high temperatures. Depending on the experiment, salt could be re-applied periodically. Samples could then be analyzed, and the hot corrosion attack evaluated. This experimental setup was a needed improvement from the crucible test, but it still failed to incorporate the combustion environment as well as a more representative salt delivery system.

In 1969, the naval ship research and development center published the first document detailing the construction and operation of a burner rig facility along with accompanying specimen evaluation techniques [74]. Since its development, naval research has relied heavily on burner rigs to evaluate potential turbine materials. Early studies were focused on determining the optimal parameters for burner rig operation such that the resulting hot corrosion attack would reproduce what is seen in a real turbine [16]. These parameters have been kept constant throughout many navy-based and navy-sponsored studies for easy comparison of results between different tests.

In its most simple form, a burner rig is an experimental setup that burns fuel to produce a high temperature corrosive environment. There are several types of burner rigs, which are categorized by their ability to recreate the actual velocity and/or pressure of a gas turbine [16]. The types of burner rigs are: (1) low-velocity, atmospheric pressure; (2) high-velocity, atmospheric pressure; and (3) high-velocity, high pressure.

The simplest type is the first one, where there is no recreation of the actual velocity or pressure of the turbine engine, only the corrosion environment. Even in these simplified conditions, the same type of hot corrosion seen in field turbine blades can be recreated. This is because the combustion environment and contaminant flux rate deposition are what allows burner rigs to truly simulate gas turbine conditions and to yield consistent results [16].

To achieve this complex environment three main processes must be coordinated. A set temperature must be achieved and maintained during the entirety of the test, a specific combustion environment must be established and stabilized, and periodic thermal-cycling must be completed. Some burner rigs rely on a flame to achieve both the combustion environment as well as the high temperature. However, this type of temperature control can be unreliable and not as versatile. Therefore, the use of a resistive element furnace is preferred. This requires the design of a special furnace with an exposure chamber capable of withstanding corrosive environments. The ability to thermal-cycle samples also requires a specially designed furnace that allows for samples to be easily moved in and out of the exposure chamber. Although early designs relied on humans to manually move the samples in and out of the exposure chamber, newer designs have been able to automate this process resulting in more reliable and periodic cycles. The combustion environment must remain the same throughout tests and therefore requires a lot of attention. Parameters that need constant monitoring include air-to-fuel ratio, contaminant flow, and fuel flow. By constructing a robust system capable of monitoring and correcting these parameters a reliably reproducible combustion environment can be established.

Burner rig testing facilities have greatly improved the study and understanding of hot corrosion. They have allowed for more realistic hot corrosion testing in lab environments. Among the various experimental setups developed through the years, burner rigs have been found to most nearly approximate the operating conditions of a gas turbine engine [75]. Their versatility also makes them a great tool for researching new materials for increasingly changing environments. The fuel, temperature, cycles, contaminant type, and contaminant levels can all be modified to adapt the resulting environment according to new technological demands.

CHAPTER 2: Experimental Methods

2.1 Samples and Pre-Exposure Procedures

All samples tested in burner rig exposures were provided by Rolls Royce. Samples are of a pin geometry, with a length and diameter of 63.5 and 3.175 mm respectively. This geometry is shown in Figure 5.

All samples were catalogued and individually labeled. Prior to exposure, the diameter of all samples was measured at three different heights of interest using a Keyence LS-7030 optical micrometer and a graduated rotating sample holder assembly. Each pin was held by the rotating assembly and the diameter was measured at 10° increments, for a total of 18 unique diameter values. The positions of such measurements along the pin, which correspond to the cross-section locations, are shown in Figure 5. The physical setup used to make such measurements is shown in Figure 6.

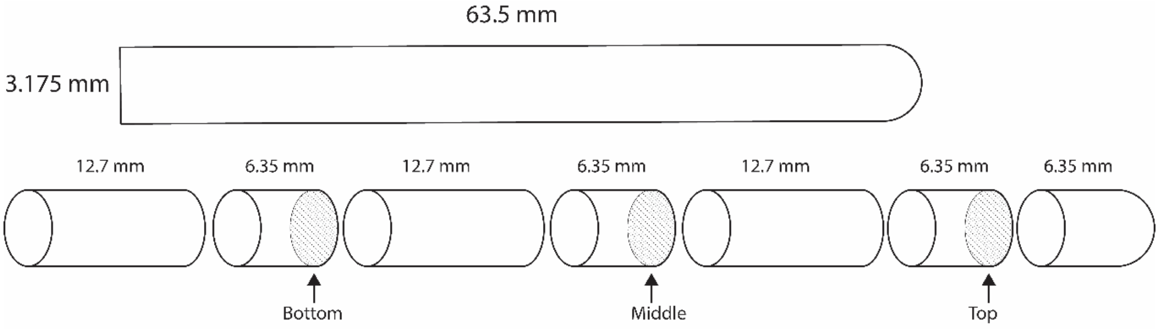

FIGURE 5. Schematic of sample geometry and location of cross-sectional analysis.

FIGURE 6. Experimental setup used for pre-exposure sample measurements. Keyence LS-7030 optical micrometer.

2.2 Burner Rig Testing

2.2.1 Burner Rig Design

The low-velocity burner rig (LVBR) at UCI was based on a similar system operated at NSWC-Carderock [74]. However, it was modified to allow for 1) fully automated thermal-cycling, and image acquisition, 2) operation at higher temperatures, and 3) programmed operation. The rig can be divided into different sections, described below:

a) Exposure Chamber and Sample Geometry: the exposure chamber in the rig accommodates a carousel cup holding up to 27 samples in the sample geometry described previously, as shown in Figure 7. The carousel rotates at 29 rpm for the duration of the test. The exposure chamber is connected to the burner and exhaust with refractory ceramic tubes ensuring a contained environment.

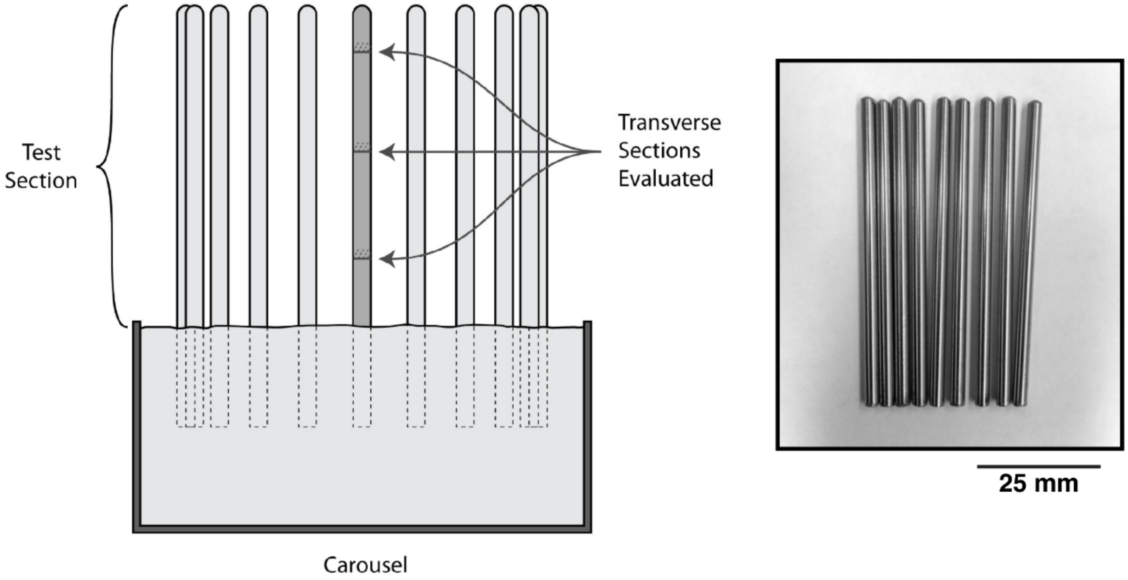

FIGURE 7. Schematic of the carousel cup that holds the samples during exposure, and sample geometry.

b) Burner and Combustor Arm: The burner is designed to be used with various commercial fuels such as NATO F-76 or JP-5. The system can run at air-to-fuel ratios over the range of 15:1 to 60:1, and it is designed so that there is no flame impingement on the samples. The system is equipped with a contaminant feed that allows different contaminants to be introduced into the combustion gasses. For the purpose of hot corrosion studies, the contaminant is synthetic sea water. The combustor was designed and is currently being maintained by our collaborators Vince McDonell and Max Venaas in the advanced power and energy program at UCI.

c) Thermal Control: To recreate turbine conditions, samples need to be exposed to high temperatures, and in order to obtain reproducible results, the temperatures need to be constant. For this reason, high temperatures are obtained by having the exposure chamber inside a resistively heated, high-temperature furnace rather than relying on the flame from the combustion to provide heat. The high-temperature furnace facilitates oxidation conditions and rapid thermal-cycling by making use of molybdenum disilicide ($MoSi_2$) heating elements.

d) Thermal-Cycling: To recreate the cycles of real turbines, samples are cycled out of the exposure chamber and allowed to cool down to room temperature for one hour. Samples are not actively cooled during this time, instead they are allowed to sit at ambient temperature. The cycle is achieved by a motorized assembly that moves the samples out of the furnace to a viewing position where samples can be visually examined at the end of each cycle. Cycles are set to be 24 hours long, with 23 hours spent inside the exposure chamber.

e) Controls, Data Acquisition and Automation: The automation of thermal-cycling and data acquisition is achieved by using a modular PC-based DAC system based on hardware and software from National Instruments. Communications are controlled through a LabVIEW program deployed to a CompactRIO modular system, which provides a rugged real time controller to enable consistent long-term reproducibility. This setup enables communications and control of mass flow controllers, furnace controllers, motors, fuel valves, and image acquisition of samples during the cool down period.

2.2.2 Burner Rig Parameters

Although extremely versatile, the burner rig was run with consistent experimental parameters for all the data presented in this work. The conditions are shown in Table 2.

TABLE 2. Parameters for burner rig operation.

Temperature	900°
Fuel Type	F-76 with 0.5 wt. % sulfur
Fuel Flow	6 mL/min
Contaminant Type	ASTM sea water
Salt Dilution	10:01
Salt Flow	0.4 mL/min
Air/Fuel Ratio	30:1
Number of cycles	44 for coated samples
	22 for bare samples
Cycle Length	24 hours
Cool down length	1 hour

During each run, 27 total samples were tested: 5 different material groups, each with 5 identical samples for a total of 25, and 2 control pins. A notch was machined at the bottom of each pin in order to keep track of the pin location with respect to the sample holder. The notch as well as its alignment is shown in Figure 8b. The bottom uncoated part of the pins was buried in a ceramic carousel that acted as the sample holder. An example carousel is shown in Figure 8a.

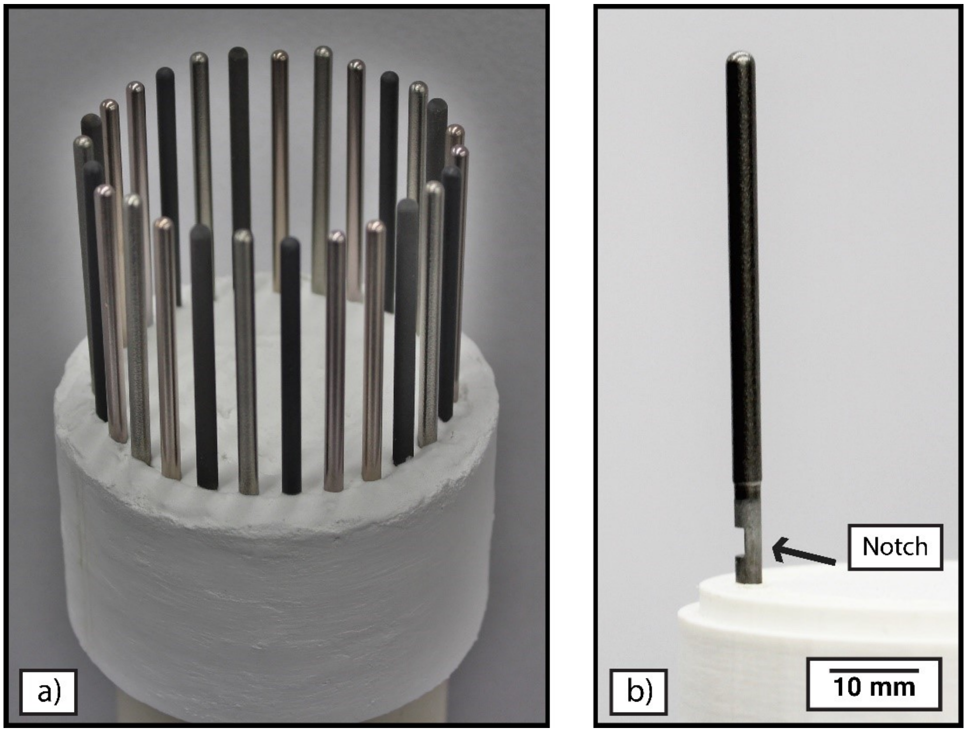

FIGURE 8. a) Sample holder shaped like a carousel holding 27 samples, b) Notch machined on samples to keep track of their location with respect to the sample holder.

2.3 Post-Exposure Sample Preparation

After testing, each sample was first washed in DI water, followed by acetone and ethanol. Each pin was dipped in epoxy multiple times until a layer of about 1-2 mm was formed, and then cut at three different areas of interest (top, middle, and bottom). Subsequently, samples were cold mounted, and standard metallographic procedures were followed in order to obtain three polished cross-sections of each pin as shown in Figure 9. The specific polishing steps followed are shown in Table 3.

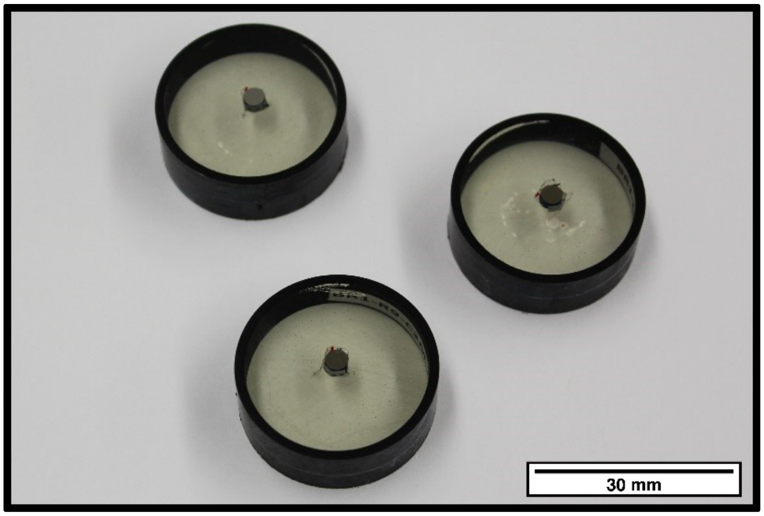

FIGURE 9. Top, middle and bottom cross-sections of one pin, mounted in epoxy and prepped for SEM analysis.

TABLE 3. Polishing steps for sample preparation.

Particle Size (µm)	Grit	Surface	Lubricant	Approx. Time (min)
35	P400	SiC	Water	10-25
30.2	P600	SiC	Water	10-25
21.8	P800	SiC	Water	15-20
18.3	P1000	SiC	Water	15-20
15.3	P1200	SiC	Water	7-15
8.4	P2500	SiC	Water	7-15
6		Cloth	Diamond Suspension	10
3		Cloth	Diamond Suspension	10
1		Cloth	Diamond Suspension	10
0.25		Cloth	Diamond Suspension	15
.02-.06		Cloth	Colloidal Silica	5-12

2.4 Materials Characterization

2.4.1 Scanning Electron Microscopy

All scanning electron microscopy (SEM) characterization was performed on a FEI Magellan 400 XHR at the UC Irvine Materials Research Institute. A concentric backscattered detector (CBS) was used to collect qualitative chemical information through the detection of backscattered electrons (BSE) which produces composition-based contrast. Quantitative elemental composition as well as elemental maps were obtained through the use of energy dispersive spectroscopy (EDS) analysis.

2.4.2 Scanning Transmission Electron Microscopy

All scanning transmission electron microscopy (STEM) work presented was acquired on a JEOL JEM-2800 transmission electron microscope at the UC Irvine Materials Research Institute, with the help of post-doctoral researcher Maryam Zahiri.

CHAPTER 3: Development of an Automated Image Analysis Protocol for Burner Rig Exposures of Pin Shaped Samples

3.1 Introduction

The hot corrosion of metallic overlay coatings and its impact on marine propulsion and power generation have been a severe problem for over 90 years [4-6]. Continuous testing and evaluation of new materials is required due to the constant need for higher energy efficiency and therefore higher operating temperatures within turbines. One of the biggest challenges when studying new materials for turbine applications is that of reproducing the exact environment within gas turbine engines. The most accurate experimental test protocols are based on burner rig systems, as they most closely reproduce (in a laboratory environment) the actual gas turbine environments by exposing samples to [16]:

a) combustion by-products of shipboard and aero-turbine fuels,

b) constant flow of contaminants, such as saltwater, and

c) thermal-cycling aimed to reproduce engine cycles.

Developing the correct experimental setup is, although extremely important, only half of the battle. Accurate sample characterization and processing protocols, capable of extracting critical and complete information from experimental samples, are equally critical. Therefore, this chapter focuses on the improvement of sample characterization processes and techniques used after hot corrosion exposures, mainly in burner rigs. When performing measurements and extracting information from any sample, geometry of the sample plays a critical role. Historically, most burner rig tests are performed on cylindrical shaped samples or, less often, on coupon shaped samples [75]. In this particular geometry, the protective coating, which is the area of interest, is less than 10% of the total diameter of the sample. This type of sample geometry reproduces the substrate-coating ratio seen in turbine parts and is therefore preferred during testing and evaluation of turbine materials. Close examination of the corrosion profile and the protective coating, therefore, requires high resolution techniques, while observations of the entire sample would require much lower resolution techniques. This makes it hard to place individual features and behaviors along the coating and corrosion profile within the larger context of the entire sample. The goal of the proposed protocol is to address this difficulty and is therefore optimized for cylindrical-shaped samples that produce circular cross-sections with small coating-substrate ratios.

The following results will be presented for the benefit of improving characterization protocols and not a full report of corrosion measurements. Further examination of hot corrosion behaviors can be found in the following chapters.

3.2 Experimental Methods

All samples used to showcase the sample analysis protocol developed and detailed in this section were:

a) prepared following the pre- and post- exposure procedures detailed in Chapter 2, and
b) exposed to type I hot corrosion conditions making use of the experimental setup described in Chapter 2.

All SEM images shown were collected with a FEI Magellan 400 XHR SEM. All algorithms and programs were written and implemented in Matlab 2017 and making use of the computer and vision system toolbox, as well as the free software Image Alignment Toolbox (IAT).

3.3 Results and Discussion

3.3.1 Previous Methods of Hot Corrosion Evaluation

In 1969, the naval ship research and development center published the first document detailing the construction and operation of a burner rig facility along with accompanying specimen evaluation techniques [74]. That report suggested that two measurements be taken on a cross-section of a burner rig exposed sample. The measurements were to be 90° apart and consist of two values: surface loss, and deepest penetration. Figure 10 depicts the original schematic from this document explaining the parameters of interest.

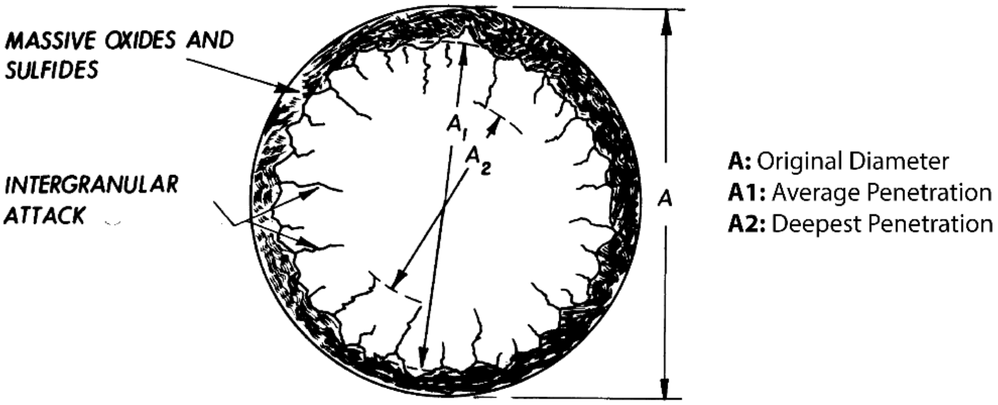

FIGURE 10. Schematic published by the naval ship research and development center in 1969, detailing how to measure hot corrosion resistance [74].

Since the publication of these guidelines, very few changes have been made to the way quantitative evaluation of hot corrosion attack is done. There has been some improvement in the optical microscopes used to perform the measurements, and the number of measurements has increased from only two to a maximum of eighteen. However, there have been no major efforts to improve the quality and quantity of data obtained from burner rig exposed samples.

Procedures used to measure material loss due to corrosion that are based on the original guidelines described above face several challenges, which are reflected in the final data as well as the size of the error associated with it. These procedures are based on at most 18 measurements taken around the circumference of the sample. Through these measurements, only about 25% of the sample's interface is accounted for in the resulting data. There is no guarantee that the 25% measured is representative of the entire sample and that no critical information was missed. Furthermore, the collected measurements are done by implementing an approximation of the circumference as a straight line, which introduces further error into the data. In addition, accuracy of the raw measurement is limited by the resolution of the optical microscope and the precision of the microscope's stage.

3.3.2 New Method for Hot Corrosion Evaluation

With the previously mentioned challenges in mind, a new sample assessment protocol was developed. This novel approach seeks to solve the existing challenges and produce more accurate and more complete data. It can measure 100% of the sample's circumference, as opposed to only 25%. It obtains higher accuracy measurements by moving to a scanning electron microscope (SEM), a higher resolution microscope. Furthermore, it eliminates unnecessary error by avoiding any straight-line approximations. High-resolution imaging of the corroded coating and adjacent substrate enables analysis of the corrosion attack and coating microstructure within the macroscopic context of the sample as a whole. All improvements are achieved by acquiring overlapping SEM images of the entire circumference of the sample and following an in-house automated image analysis algorithm that extracts the information of interest.

The process starts with SEM image acquisition and follows with a complex set of image analysis algorithms. This method can be further divided into 3 more sections. The first section processes each image individually to extract the corrosion profile from each image [76]. The second section makes use of image feature recognition and matching in order to stitch all images together and recreate the cross-section as well as the extracted profile. The third section extracts numerical values from the stitched image of the extracted profiles. Each step of the process is further explained in more detail in the following segments.

3.3.2.1 Image Collection

The first step is to collect overlapping, backscattered SEM images of the entire circumference of the sample. A couple different approaches were considered. The first approach involved simply performing a concentric rotation of the sample after an image is taken. This way, the orientation of the sample's surface would remain the same in all images. The second approach avoided any rotation and instead performed and xy-move of the sample. In this case the orientation of the sample's surface does not remain the same for all images. The second approach, although requiring more images to go around the circumference, was deemed more appropriate for the type of image stitching being performed because it reduced error due to stitching. During the image stitching part of the process, image recognition is used to detect matching features. Through a series of computations, the geometric transformation necessary to match those two features is calculated. In the case of the second approach the transformation can be restricted to a rigid one, where no rotational movements are allowed. In the case of the first approach, rotation must be accounted for, and can be a source of error during the stitching part of the algorithm. Therefore, overlapping images were collected by performing xy-moves of the sample. This was done in such a way that the resulting images had at least 10% overlap.

It is of course very important that all images are collected under the exact same conditions so that the feature recognition algorithm can identify the same feature in different images and match them up. The horizontal field width must be set so that the smallest feature of interest can be accurately captured. The resolution must be high enough to capture relevant data, the only downside to collecting at higher resolutions is the time constraint. Sample preparation is very important as well, due to the cumulative nature of this process, small amounts of drifting will result in large data error and discrepancies.

3.3.2.2 Image Processing Section I – Profile Extraction of Individual Images

An in-house MATLAB program is utilized to process images as follows:

i. A threshold algorithm is applied to the original image, which results in a binary image (Figure 11b).
ii. A succession of closing and inversion algorithms are applied in order to obtain a two-region binary image, where the region boundary corresponds to the corrosion profile (Figure 11c-f).
iii. An erosion step is applied in order to obtain an image that differs from the previous one by a one-pixel line that corresponds to the region boundary or corrosion profile (Figure 11g).

iv. The eroded picture is subtracted from the non-eroded picture, and the result is the one-pixel line that divides the two regions in the image. This line corresponds to the corrosion profile of the sample (Figure 11h-i).

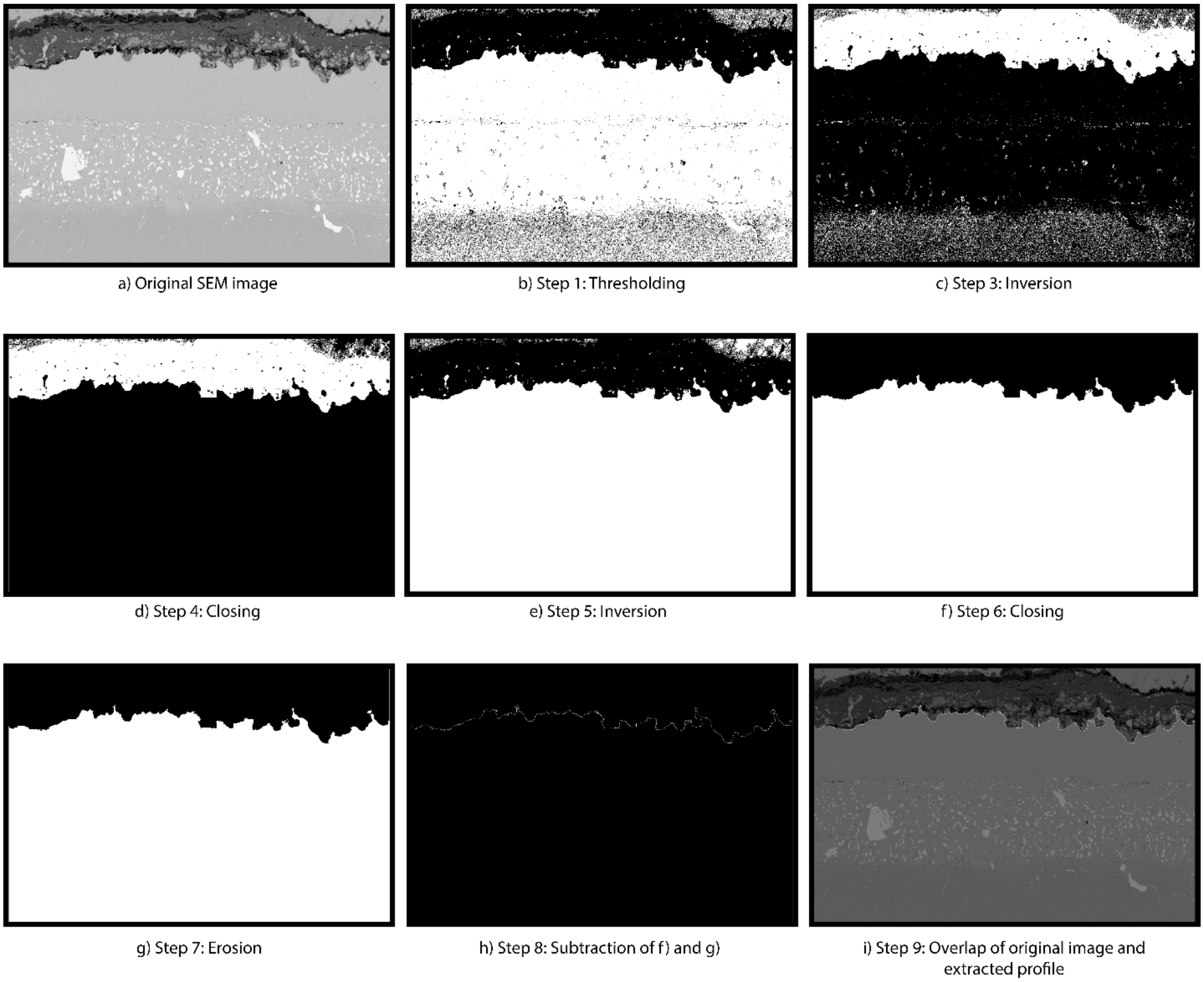
a) Original SEM image
b) Step 1: Thresholding
c) Step 3: Inversion
d) Step 4: Closing
e) Step 5: Inversion
f) Step 6: Closing
g) Step 7: Erosion
h) Step 8: Subtraction of f) and g)
i) Step 9: Overlap of original image and extracted profile

FIGURE 11. Outline of steps followed during Image Processing Section I.

This step results in two sets of images. The first one containing the original SEM images, and the second containing binary images with the corresponding extracted one-pixel thick corrosion profile.

3.3.2.3 Image Processing Section II – Image Stitching

After individual processing, each original SEM image is parsed through, and making use of image feature recognition, unique features are extracted along with their locations. The extracted features of adjacent images are compared, if a match is found the geometric transformation that would align the features is calculated. The series of obtained transformations is applied to all images in order to arrive at one final stitched image. The same transformations are also applied to the set of binary images containing the extracted profiles, and a second stitched image is obtained. The first image is a stitched image of the original SEM images, while the second one is one of only the extracted profiles, both shown in Figure 12. The stitching algorithm does not resize or warp images; it simply applies a Euclidean transform, which allows conservation of the pixel to micron relationship. As a consequence of not resizing images, the size of the resulting image is around 14,000 x 14,000 pixels.

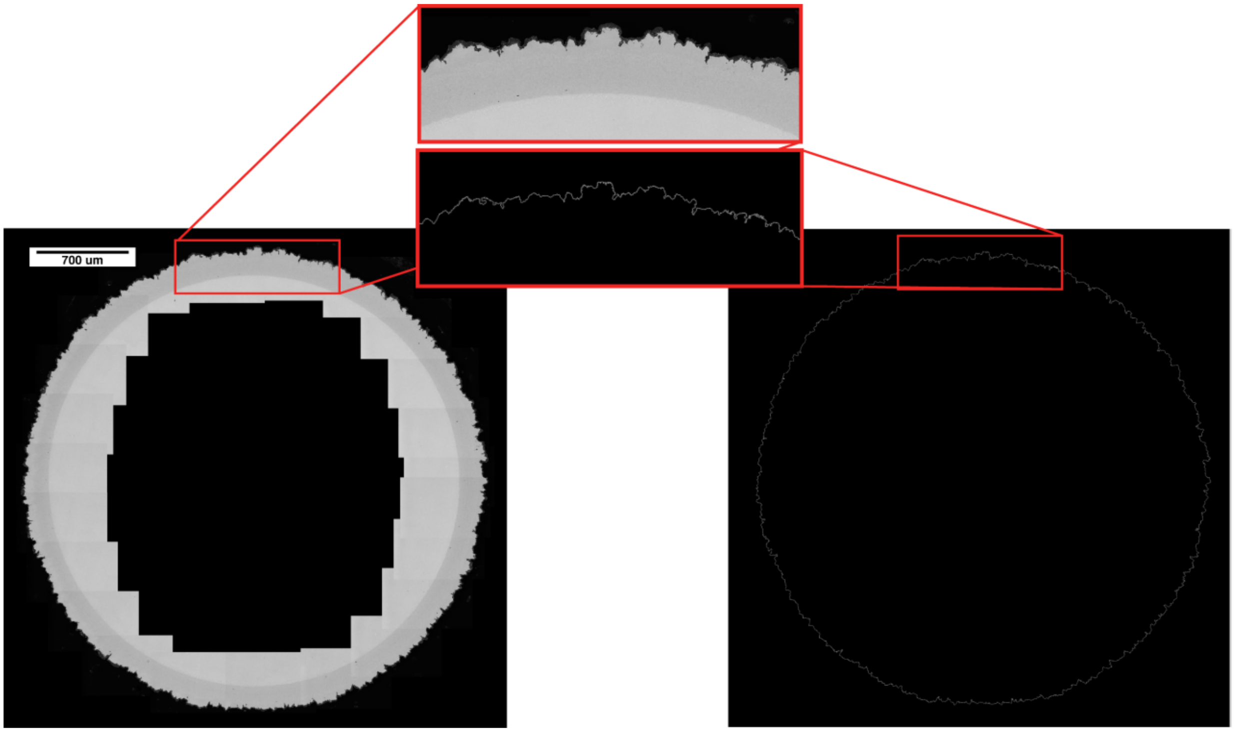

FIGURE 12. Final product of Image Processing section II, containing all SEM images stitched together and the corresponding corrosion profile.

3.3.2.4 Image Processing Section III – Data Extraction and Processing

Following individual analysis and stitching, data extraction is performed. The center of the pin must be located in order to arrive at any meaningful conclusions regarding coating material lost during the hot corrosion attack. The center is found by using the substrate/coating interface as a reference and approximating to a perfect circle (shown in blue in Figure 13). Using the coordinates of the center, the radius of the corrosion profile at every single point along the sample's circumference is extracted (shown in orange in Figure 13).

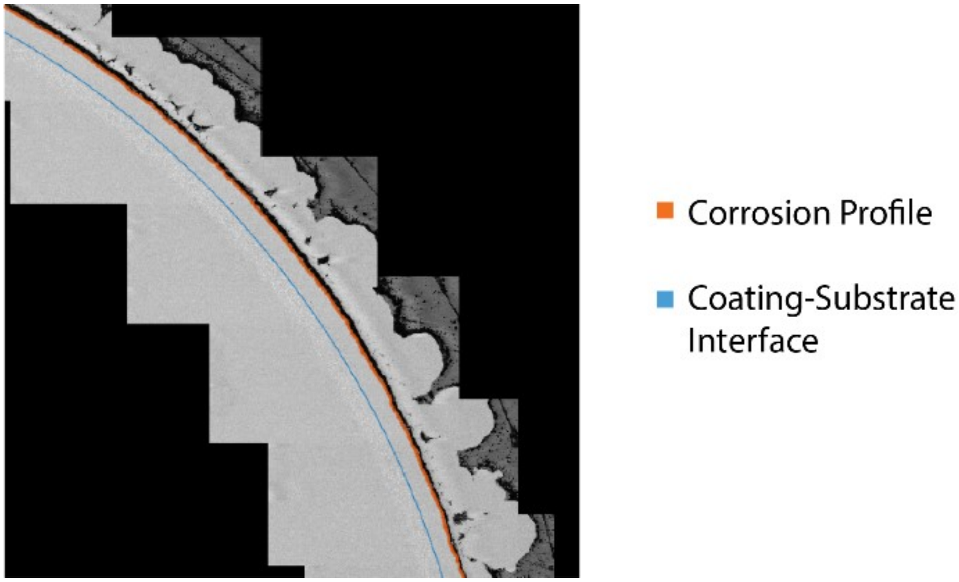

FIGURE 13. Reconstructed image showing the substrate/coating interface in blue and the corrosion profile in orange.

This step produces a very large data set that can be used to extract the average, maximum, minimum and all other relevant statistics of the corrosion profile. However, it is most useful for visualization of the attack's shape and extent, which was not possible with previous protocols.

Several aspects of the corrosion attack, which were previously hard to characterize, are now easily observed and quantified. There can be great non-uniformity of the attack with respect to angular position along the circumference of the pin. This indicates preferential attack with respect to the location of the sample within the exposure chamber and sample holder. This data as a function of angular location coupled with position tracking of the sample can provide further insight into corrosion mechanisms as a function of gas flow direction.

Sample comparison is made much easier, and relevant to engine conditions. Rather than comparing two numbers, the entire corrosion front (shape and extent) can be compared and offer more insightful information. Localized attacks, such as the one shown in Figure 14, are easily identifiable in the resulting graph, and later mapped in the stitched image of the sample, or vice-versa. A direct comparison of the previous analysis method and the newly developed sample assessment protocol is presented in Appendix A.

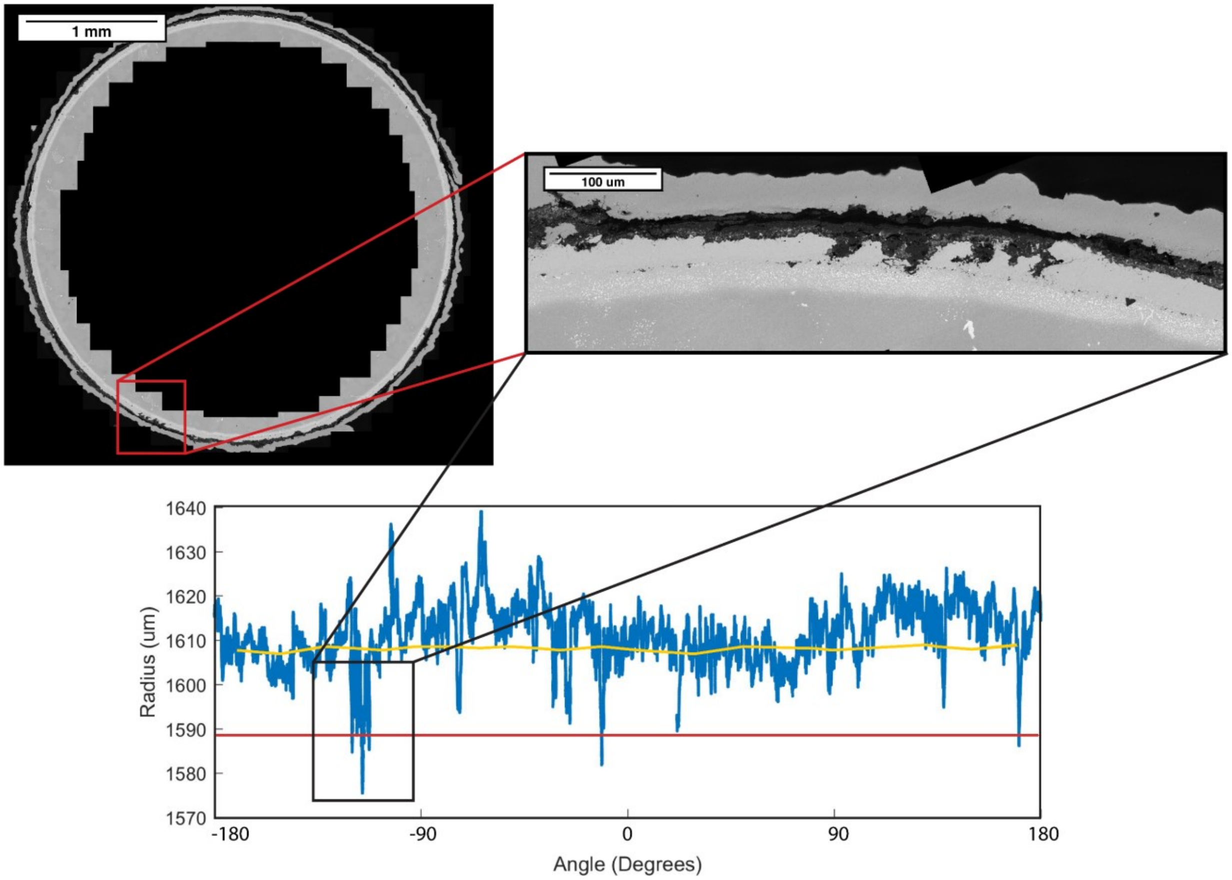

FIGURE 14. Example of a reconstructed cross-section with corresponding corrosion profile. Localized attack is highlighted in both cases and magnified. Extracted corrosion profile shown in blue, sample radius pre-exposure shown in yellow, and substrate/coating interface shown in red.

3.3.3 Case Studies

During development and evaluation of this new sample analysis protocol, different attack morphologies and phenomena were observed. In each case, the new protocol facilitated the identification and study of the attack nature and microstructural details. Some of the more common cases encountered are described below.

3.3.3.1 Uniform Attack

The simplest attack morphology observed was experienced by overlay coatings. In this case, the attack was very uniform along the circumference of the pin, and there was not a significant amount of material loss. An example of this case is shown in Figure 15.

Even for the simplest case, previously ignored data can be extracted and used to further characterize the hot corrosion attack. Values, such as tortuosity, roughness, standard deviation, etc., are all readily available for comparison purposes and provide a quantitative way to evaluate the morphology of the attack and nature of the coating/oxide interface.

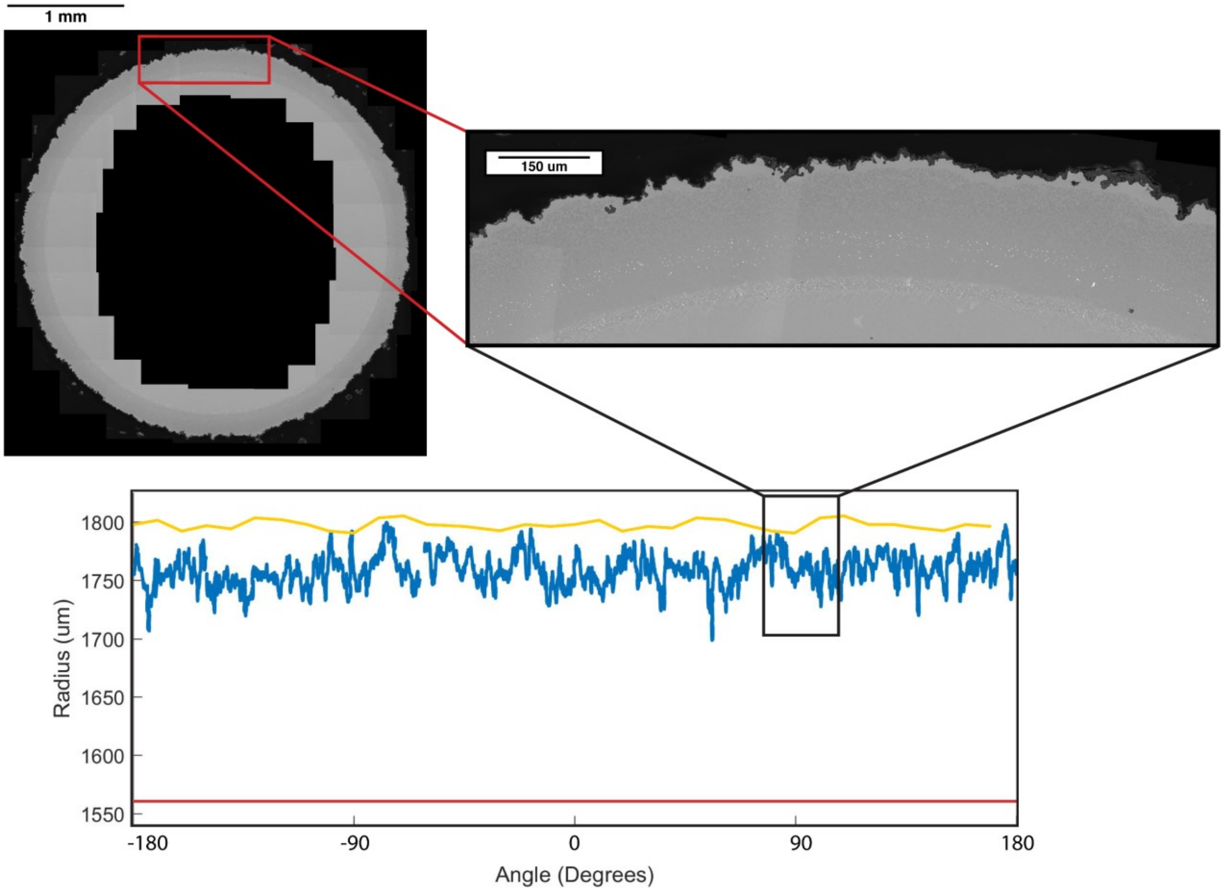

FIGURE 15. Example of a reconstructed cross-section with corresponding corrosion profile. where uniform attack can be observed. Extracted corrosion profile shown in blue, sample radius pre-exposure shown in yellow, and substrate/coating interface shown in red.

3.3.3.2 Non-Uniform Attack with Significant Singularities

The second case of interest is one where the attack is not uniform, and it exhibits preferential attack in certain areas leading to singularities along the profile, as shown in Figure 16. For this case, visualization of the entire corrosion profile in the context of the entire sample is critical. Determining the relationship between substrate microstructure and coating performance is made easier by the ability to a) quickly identify singularities in the extracted profile, and b) map those singularities on the stitched image. Knowledge of the pin’s position within the exposure chamber allows matching of accelerated attack areas to a location within the chamber.

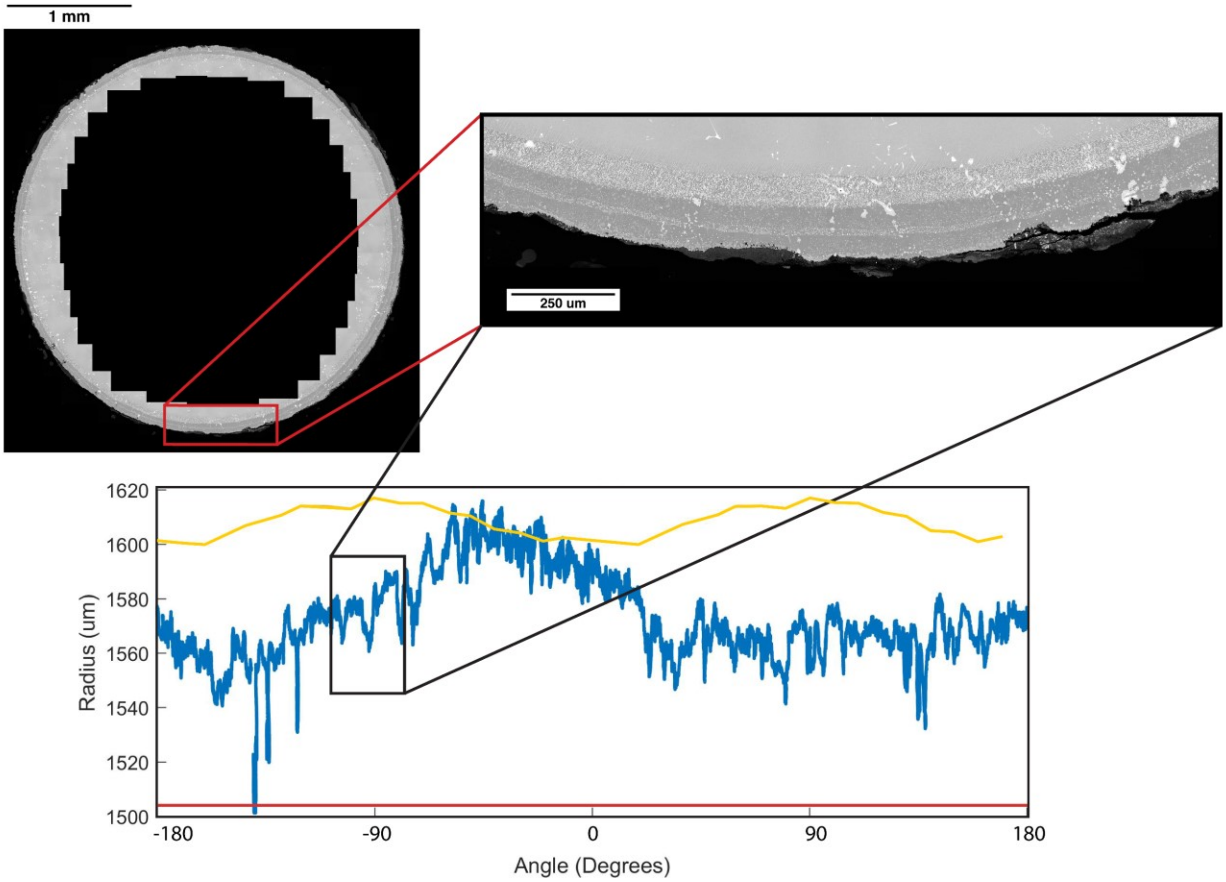

FIGURE 16. Example of a reconstructed cross-section with corresponding corrosion profile where non-uniform attack with significant singularities can be observed. Extracted corrosion profile shown in blue, sample radius pre-exposure shown in yellow, and substrate/coating interface shown in red.

3.3.3.3 Non-Uniform Attack with Swelling

The third case exemplifies the importance of imaging the complete cross-section and extracting the entirety of the profile. During analysis, it was discovered that platinum-modified nickel aluminide diffusion coatings undergo a significant amount of swelling before extensive corrosion can be observed. The swelling was preferential, with all samples only experiencing it on two opposing quadrants. This preferential behavior can be analyzed within the context of the entire sample (substrate microstructure), as well as its positioning within the exposure chamber (gas flow), both of which are readily available through the delineated protocol. Further analysis and discussion of the swelling phenomenon can be found in Chapter 5. An example of this case is shown in Figure 17.

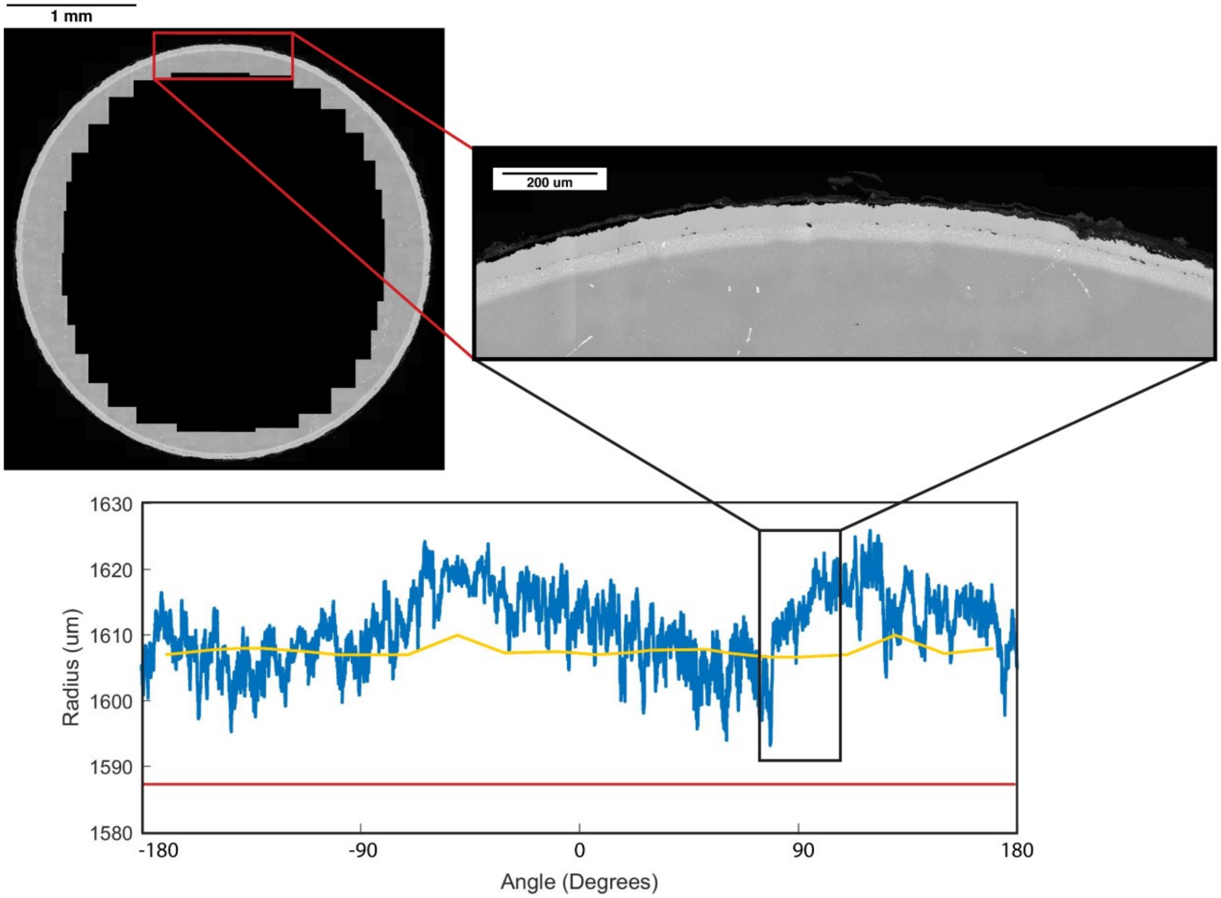

FIGURE 17. Example of a reconstructed cross-section with corresponding corrosion profile where non-uniform attack with swelling can be observed in the areas where the extracted corrosion profile (blue) is larger than the measured pre-exposure radius (yellow). The substrate/coating interface is shown in red.

3.4 Conclusions

It has been established that current procedures for the evaluation of hot corrosion attack on burner rig exposed samples are all based on antiquated techniques due for an upgrade to match technological advances. Several shortcomings of current sample evaluation procedures were highlighted: only about a quarter of the sample's interface is accounted for, which might not be representative of the entire sample, and the measurements collected are done so through the approximation of the circumference as a straight line. In addressing the concerns listed, a new way of assessing and analyzing corrosion resistance of cylindrical shaped samples exposed to burner rig experiments was developed. The focus of the new procedure was to obtain high magnification details of the corrosion profile while still retaining information of the sample as a whole, which was achieved through the stitching of multiple high-resolution SEM images. The new protocol proved to deliver more accurate and more complete information regarding the corrosion of burner rig samples. Image processing and analyzing was used to extract a one-pixel thick line corresponding to the corrosion profile, which allowed measurements to be performed at every point around the circumference of the sample. This large data pool was used for visualization of the corrosion front, which revealed previously unexplored aspects of the attack, such as overall and local shape, uniformity, tortuosity, etc.

Details regarding the nature of the corrosion attack were made easily accessible through the new sample analysis protocol. It is our goal that results obtained from this type of analysis can aid in the search for improved gas turbine materials as well as in the development of the necessary testing techniques.

CHAPTER 4: Evaluation of a New Substrate Material and the Role of Dopants in its Hot Corrosion Resistance

4.1 Introduction

The energy needs of our society are not only constantly increasing, but also constantly evolving. It is no longer enough to merely meet those needs at any cost; it is now imperative that we meet our energy needs in a conscientious way that ensures the well-being of our planet. In the gas turbine field this means reaching higher operating temperatures and higher energy efficiencies. Furthermore, advancements in both technology and our understanding of the different environments within a turbine have opened the door for the use of highly specialized materials optimized not only for temperature, but also for environment. Therefore, there is a continuous need to constantly search and evaluate new materials with better performance.

Nickel based super-alloys are used as substrates for the hot-sections parts of gas turbines [40]. Due to the high operating temperatures and the potential contaminants from the environment protective coatings are often applied to their surface. These coatings are application-specific and, although facing challenges of their own, can provide good protection against the different types of degradation that materials experience, such as extreme high temperature, erosion, hot corrosion, etc. [51]. Hot corrosion is a degradation mechanism characteristic of salty (marine) environments where the presence of salt and high temperature prompts a process in which molten salt infiltrates the turbine part and causes a series of reactions that result in material loss, sulfidation, deep penetration of salt constituents into the part, and ultimately mechanical failure [27]. Sulfate salts of sodium, calcium, and potassium, as well as vanadates and carbonates have all been shown to cause hot corrosion in superalloys. However, in marine gas turbines the most common deposit is Na_2SO_4. The source of this deposit can vary, as sodium and sulfur can be present in the fuel as impurities, or NaCl and/or sulfates can be ingested through the turbine intake air [12].

Due to the presence of a protective coating, the hot corrosion resistance of nickel-based superalloys used as substrates has not been a priority in the past. However, higher operating temperatures have resulted in the use of internal cooling, where air is pushed through the blade's cooling channels as shown in Figure 18 [77]. These cooling channels are small and deep enough that applying a protective coating to the surface is not an option and are therefore targets for hot corrosion attack [78]. Furthermore, the root of the blade, shown in Figure 18, where the blade is attached to the rotating shaft is usually not coated and can therefore serve as an initiation point for hot corrosion attack that undercuts the protective coating. Consequently, the search for efficiency improvements, no matter how small, has shifted interest back to the hot corrosion resistance of substrate materials.

Hot corrosion attack experienced during the lifetime of a turbine is not constant. Temperatures fluctuate depending on the engine's needs, the level of contaminants in the intake air varies depending on location, etc. Therefore, it is entirely possible that a turbine part could first experience an oxidation step where no salt deposits have formed, followed by hot corrosion attack with molten salts. It is therefore also important to investigate the effect, if any, that short oxidation exposures have on the subsequent hot corrosion resistance of substrate materials.

With that in mind, this work aims to evaluate the hot corrosion resistance of new substrate materials with the goal of aiding the development of better performing alloys as well as improving the current understanding of hot corrosion attack of nickel-based superalloys.

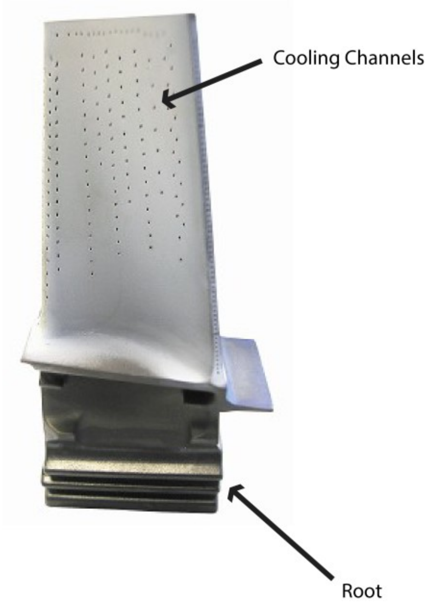

FIGURE 18. Image of a turbine blade where the root and cooling channels, both uncoated areas susceptible to hot corrosion attack, are highlighted [77].

4.2 Experimental Methods

4.2.1 500-hour Exposures

The type I hot corrosion resistance of four new candidate materials optimized for the high temperature section of gas turbines is evaluated alongside that of five commercially available superalloys. The sample geometry and sample preparation are detailed in Chapter 2.

The four new candidate materials consist of a base alloy, Alloy1, and 3 doped versions, doped with hafnium, silicon, and hafnium-silicon. The list of all materials and their compositions are given in Table 4. The exact composition of Alloy1 is not provided, due to it being proprietary, a maximum wt. % allowed is provided instead. Doping level is kept under 1 wt. %.

*TABLE 4. Substrate composition in wt. %. *For Alloy1 only maximum wt.% is provided.*

Substrate	**Ni**	**Cr**	**Co**	**Mo**	**Al**	**Ti**	**Ta**	**W**	**Zr**	**C**	**B**	**Hf**	**Re**	**Nb**
CMSX-4	61.7	6.5	9	0.6	5.6	1	6.5	6	-	-	-	-	3	-
CM186LC	62.6	6	9	0.5	5.7	0.7	3	8	0.01	0.07	0.02	1.4	3	-
IN-738	60.5	16	8.5	1.7	3.5	3.5	1.7	2.5	0.05	0.09	0.01	-	-	2
IN792Hf	60.1	12.3	8.9	1.8	3.4	3.9	4	4.4	0.05	0.12	0.01	1	-	-
MM509	10	23.4	54.8	-	-	0.2	3.5	7	0.5	0.6	-	-	-	-
Alloy1*	65	15	12	5	6	6	7	5	-	-	-	-	-	-

4.2.2 10-hour Exposures

4.2.2.1 Sample Geometry and Preparation

For the shorter exposure as well as the pre-oxidation studies a different sample geometry was utilized. The pin-shaped samples described in Chapter 2 were cut using a Logitech APD1 high-speed saw into buttons having a diameter and height of 3.175 mm and 3 mm respectively. The main face of the button was polished using the polishing procedures detailed in Chapter 2 to a roughness of 1 micron.

Post-exposure, samples were first mounted on an SEM stub and sputter coated with carbon using a LEICA 200 sputter coater for analysis of the surface of the oxide, both through SEM imaging as well as EDS compositional analysis. Subsequently, samples were cold mounted in epoxy resin transversely in order to characterize the cross-section of the oxide. Mounted samples were polished using the procedures described in Chapter 2 and prepared for SEM analysis. Figure 19 shows the geometry of the samples as well as the cross-section imaged.

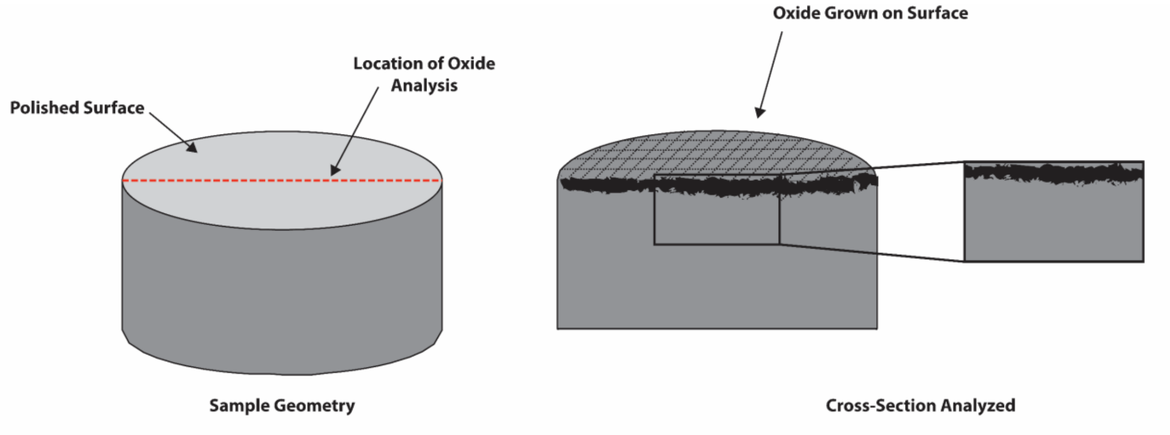

FIGURE 19. Schematic of sample geometry and location of cross-sectional analysis for the shorter exposures.

4.2.2.2 Pre-Oxidation Conditions

Pre-oxidation exposures were carried out making use of the burner rig furnace as a bottom loading furnace. Utilizing a bottom loading furnace allows for samples to be introduced to the exposure temperature in a very limited amount of time. During the introduction of the samples into the furnace, temperature deviated from the target temperature on average by 10 °C, and the samples were pushed into the furnace at a speed of 2.54 mm/s. Two different pre-oxidation conditions were used, both taking place at 900 °C and only varying on the length of exposure. The two different pre-oxidation conditions, PreOx1 and PreOx2, had exposure lengths of 15 minutes and 1 hour respectively.

4.2.2.3 Quantitative Measurements of Oxide Parameters

Four parameters of interest were measured directly from high resolution SEM images making use of ImageJ. These values were collected along a cross-section 518 microns in length.

Oxide thickness was measured from one edge of the outer oxide layer to the other edge, not including any internal oxidation. Internal oxidation was measured from the oxide/substrate interface to the innermost point of internal oxidation. In both cases 15 measurements were collected, and an average and standard deviation values were calculated.

Crack to crack length was determined by measuring the distance between adjacent vertical cracks. Delamination percent was determined by measuring the distance where the oxide had completely detached or where a horizontal crack was present at the oxide/substrate interface. The length of all the measured delaminated zones was added and a percentage was calculated. For both cases, the distance analyzed was kept constant, and the necessary measurements to cover such distance were carried out.

4.3 Results and Discussion

4.3.1 Characterization of the As-Processed Microstructure

The initial microstructure of the four new substrate materials exhibited many differences despite having compositional variances of under 1 wt. %. At the macro scale, shown in Figure 20, the degree of interdendritic segregation varies with dopant. Alloy1 shows a high degree of elemental segregation along the different parts of the dendrite. The addition of hafnium increases this segregation and therefore, the non-uniformity. Adding silicon helps the uniformity, but surprisingly, it is the addition of both hafnium and silicon that helps the uniformity the most.

A second feature notable at the macro scale is the presence of γ-eutectic, represented by the bright phase in the backscattered electron images. The phase is present in all four alloys, but it is more prevalent in Alloy1+Hf. The γ -eutectic is rich in nickel, titanium, and tantalum, indicating that the solubility of these elements in both the matrix, γ, and the precipitates, γ’, was lower than the concentration of said elements. In the case of Alloy1+Hf, the γ-eutectic is also rich in hafnium, which could hint to an over-doping of hafnium. There have been extensive studies discussing the reactive element effect [79-86]. In the case of hafnium, it has been showed for oxidation conditions that while small amounts of hafnium can be extremely beneficial for the formation of a protective oxide with good adhesion properties, larger amounts of hafnium can be detrimental [87]. Gheno’s work [88] focused on determining hafnium tolerance levels as a function of alloy composition. Where the tolerance level defines the line where hafnium addition transitions from being beneficial to detrimental. Although many studies have been done on the effect of hafnium doping under oxidation conditions, not enough work has been done on analyzing how these results translate to a corrosive environment, where there is not only oxidation happening, but also sulfidation and dissolution of oxides.

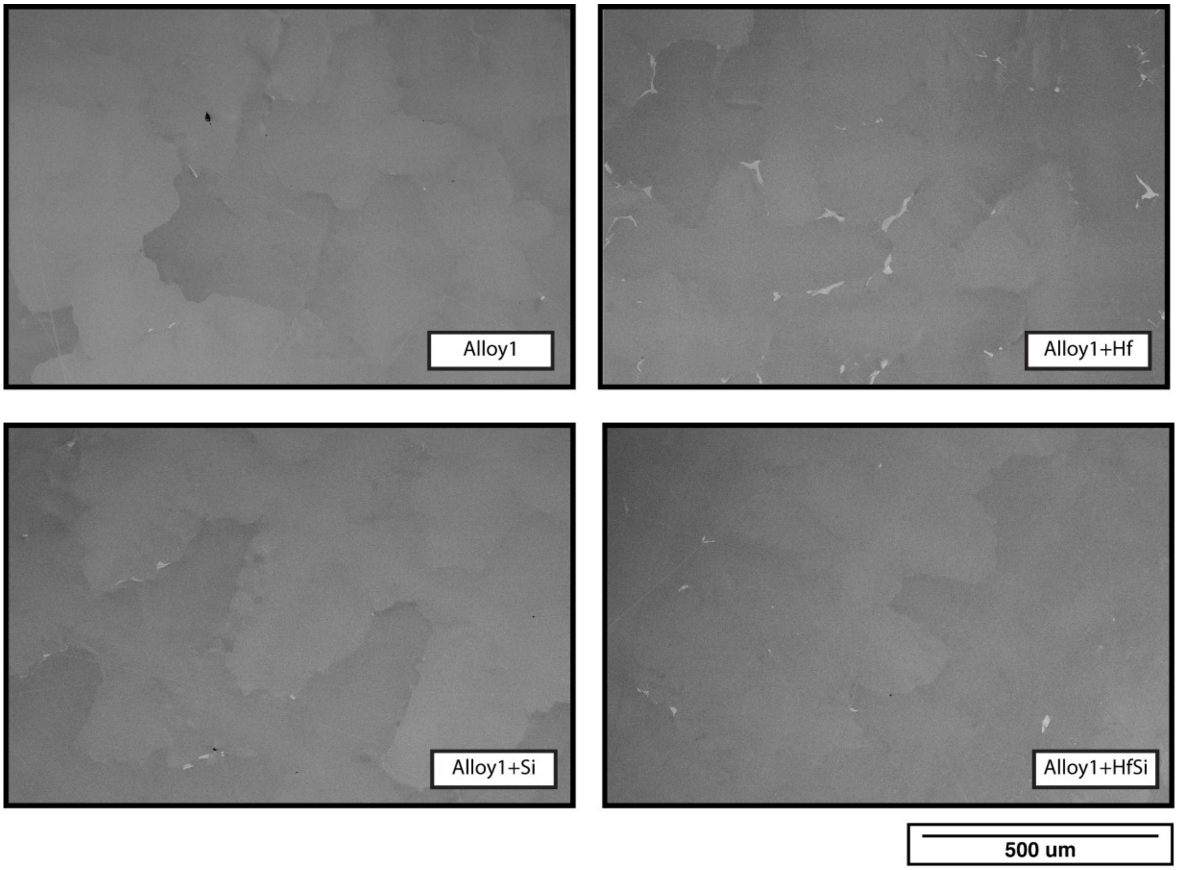

FIGURE 20. Low-magnification, backscattered SEM images of cross-sections of Alloy1 and its doped variations where the as-processed microstructure shows dendritic and interdendritic elemental segregation.

At the micro scale, differences in the shape of the γ' precipitates can be observed in Figure 21. Alloy1 shows cuboidal γ' precipitates, while the doped versions exhibit deviations from cuboidal. The addition of hafnium results in less cuboidal and slightly smaller precipitates. The addition of silicon results in less cuboidal and slightly larger precipitates, while the addition of both hafnium and silicon results in less cuboidal precipitates that create highly directional paths in the γ matrix. This is evidence of potential change in lattice mismatch between the γ-matrix and the γ'-precipitates. The shape of the γ'-precipitates is expected to be spherical for mismatches smaller than 0.2%, cuboidal for mismatches of 0.5 to 1%, and plate-like for mismatches above 1.25% [42]. Therefore, the elongation of the γ'-precipitates observed in Alloy1+Hf, Alloy1+Si, and Alloy1+HfSi is most likely a result of an increase in the lattice mismatch caused by the segregation of dopants to the γ' phase.

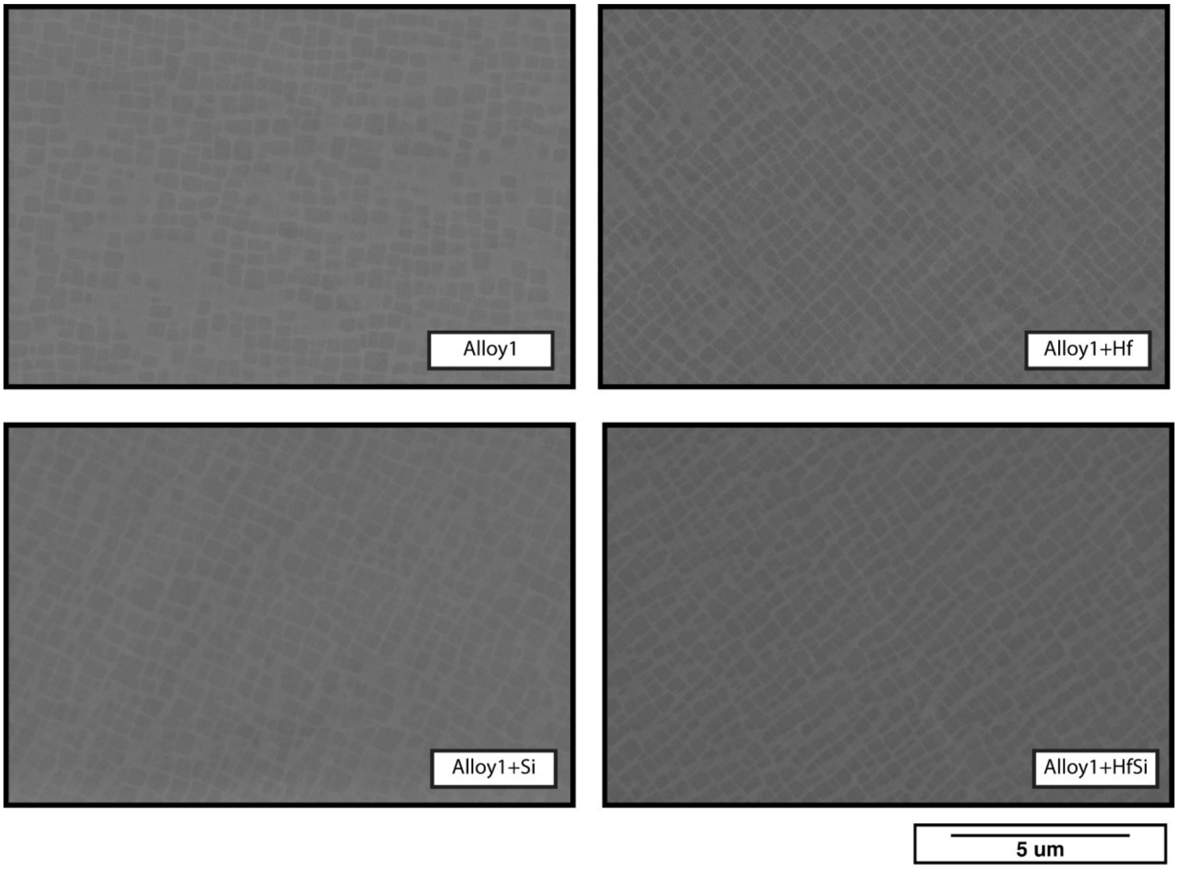

FIGURE 21. High-magnification, backscattered SEM images of cross-sections of Alloy1 and its doped variations showing the different γ – γ' microstructures.

The initial analysis revealed both different microstructures and elemental segregation behavior among the four different materials. These differences are important to keep in mind as we study their hot corrosion behavior. Differences in hot corrosion resistance can be due to the active role of the dopants during the hot corrosion attack, or due to the role that dopants had during casting and/or heat treatment leading to a different microstructure.

4.3.2 500-hour Low-Velocity Burner Rig Exposure

The four new substrate materials along with the commercially available superalloys were evaluated under long-term exposures, which provide valuable information regarding substrate lifetime and mode of attack.

4.3.2.1 Quantitative Analysis of Hot Corrosion Resistance

The hot corrosion resistance of bare superalloys was evaluated by measuring the cross-sectional area of the unaffected substrates in the exposed samples and comparing them to the cross-sectional area of the samples before exposure. A value of diameter loss was also calculated by fitting a circle to the remaining unaffected substrate in the exposed areas and comparing its diameter to the diameter of each sample before exposure.

The performance of the new superalloys was compared to that of commercial superalloys: IN738, IN792Hf, and MM509, as shown in Table 5. CMSX-4 and CM186LC although tested, were not used for this comparison since they exhibited extreme corrosion with little unaffected remaining substrate. However, they are the subject of further studies focused on the role of carbides in hot corrosion not discussed in this work. The commercially available IN738 is used as a standard for comparison purposes, while the IN792Hf is included due to having a similar composition to that of the new materials. MM509 was included as an example of a cobalt-based superalloy.

TABLE 5. Material loss and performance summary of all substrate materials tested.

Substrate Material	Total Area Loss (mm^2)	St. Dev. (mm^2)	Diam. Loss (mm)	St. Dev. (mm)
IN738	0.633	0.1	0.247	0.1
IN792Hf	1.264	0.4	0.411	0.1
MM509	0.634	0.1	0.228	0.0
Alloy1	1.546	0.5	0.527	0.2
Alloy1+Hf	1.904	0.8	0.651	0.3
Alloy1+Si	1.119	0.5	0.362	0.2
Alloy1+HfSi	0.985	0.4	0.283	0.1

Commercially available and widely used superalloys, IN738 and MM509, had the highest hot corrosion resistance, losing the least material to the attack. They also showed uniformity of attack across different samples and different positions along each sample demonstrated by the low values of their corresponding standard deviations. The new candidate materials, although not as high performing as the above-mentioned alloys, were comparable to one commercial alloy, IN792Hf.

The results summarized in Table 5 show that although the new candidate materials did not exhibit improved hot corrosion resistance, the doped variations did show some interesting results worth analyzing. Alloy1 and its 3 variations were further studied to understand the differences in hot corrosion resistance and the mechanisms behind it.

4.3.2.2 Qualitative Analysis of Hot Corrosion Resistance

By the end of the 500-hour exposure, the differences in behaviors were apparent simply by looking at the different materials. Figure 22 shows what the pin-shaped samples looked like after the exposure and before any sample preparation. In the case of Alloy1+Hf, the attack has been much more severe than that of the other samples.

FIGURE 22. Image of Alloy1 and its doped variations post-exposure.

When determining the hot corrosion resistance, or extent of attack, the worst attacked area was used for measurements, since it is the limiting factor in the lifetime of a part while in use. While examining the four different materials, two types of worse attack, or highest degree of corrosion were observed. Both attacks resulted in substantial material loss, but the corrosion products differed.

a) The first case, shown in Figure 23a, exhibits extreme internal sulfidation with the penetration depth reaching the hundreds of microns. In this case, oxidation is not as extreme, and the resulting oxide is thinner, and in some cases less porous.

b) In the second case, shown in Figure 23b, there is extensive hot corrosion attack resulting in rampant oxidation and formation of very thick, porous, and non-protective oxides. In this case internal sulfidation is observed, but the sulfidation front is contained.

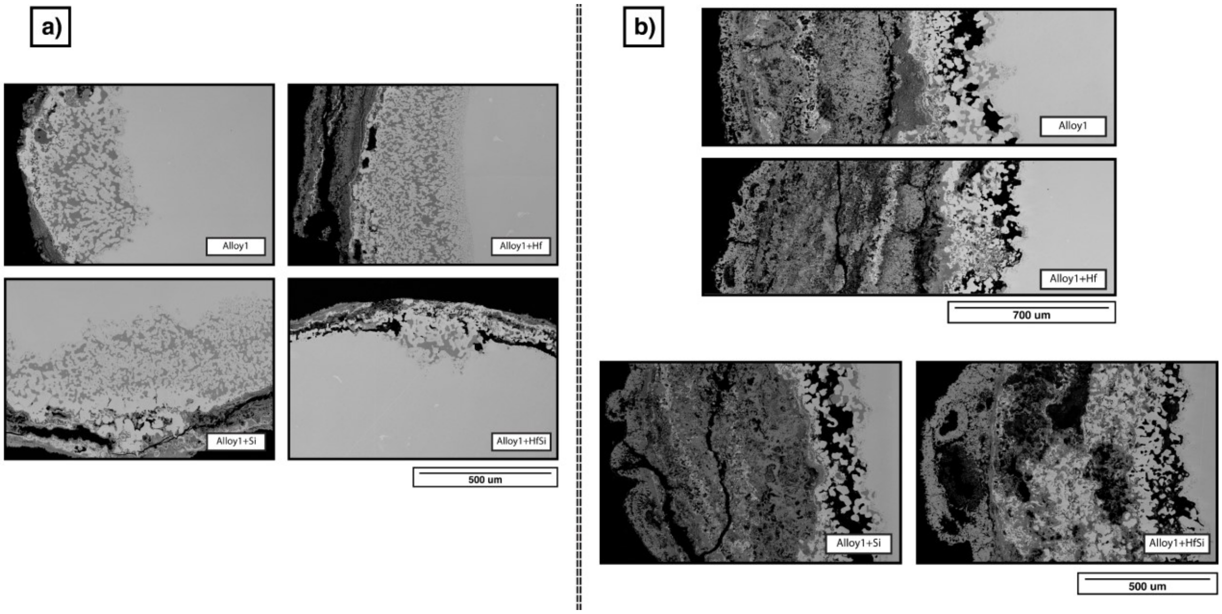

FIGURE 23. Backscattered SEM images of cross-sections of Alloy1 and its doped variations showing the highest degree of a) sulfidation attack, and b) rampant oxidation attack.

In order to understand the effect that the different dopants had on the hot corrosion resistance of Alloy1 their sulfidation and oxidation behavior were more closely examined.

4.3.2.3 Sulfidation Behavior

A more detailed analysis of the sulfidation resistance of Alloy1 and its three variations was performed to understand the different behaviors showcased in Figure 23a. A total of 15 cross-sections (top, middle, and bottom of 5 pins) per material were analyzed and, based on the most highly sulfidized area, they were categorized into 5 different groups as follows:

a) ‘Least sulfidation’ refers to the samples that had the best behavior overall.

b) ‘Slightly larger sulfides’ refers to samples where internal sulfidation is starting to be more significant and some initial coarsening of sulfides is present.

c) ‘Sulfidation attack has started’ refers to samples where a particular area has started to form significant internal sulfides.

d) ‘Sulfidation attack has spread’ refers to samples where a clear attack spot has been established and sulfidation is spreading through extensive coarsening.

e) ‘Too far gone’ refers to samples where the attack is so extensive that it has spread throughout the sample deeming most of the material unusable.

The results of this categorization are shown in Figure 24, where clear trends in hot corrosion resistance can be observed. The distribution for Alloy1 is right shifted, with most samples exhibiting sulfidation attack that has spread, indicating low sulfidation resistance. Alloy1+Hf is further right shifted, indicating that the addition of hafnium was detrimental for the sulfidation resistance of Alloy1. Some improvement is observed in Alloy1+Si indicative of silicon having a beneficial effect for sulfidation resistance. However, the overall distribution is still right shifted. A significant left shift is observed for the case of Alloy1+HfSi, which indicates that although hafnium alone had a detrimental effect, and silicon had only a small beneficial effect, when combined, both of these dopants greatly improve the hot corrosion and sulfidation resistance of the base superalloy.

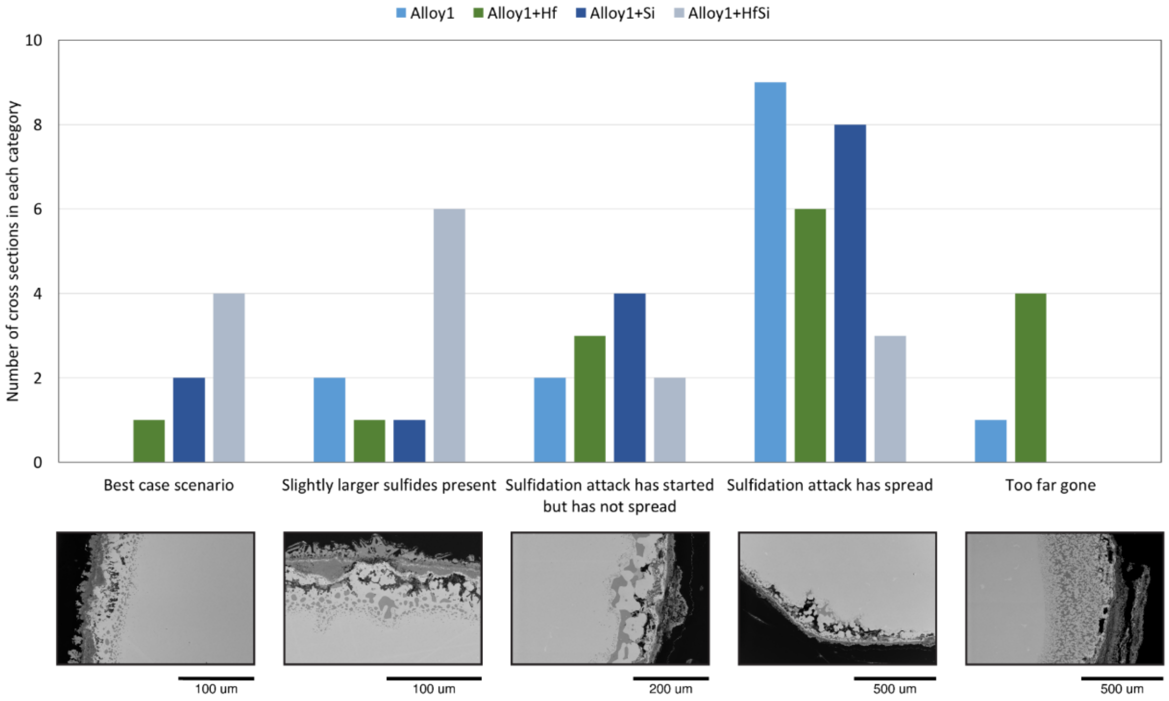

FIGURE 24. Summary of sulfidation behavior among Alloy1 and its doped variations.

Further analysis of the attacked areas revealed that Alloy1 and Alloy1+Hf experience very similar extreme internal sulfidation, characterized by rapid growth of sulfides with no directionality or preferred coarsening behavior. On the other hand, Alloy1+Si and Alloy1+HfSi exhibited higher sulfidation resistance, slowing down the attack by having sulfides coarsening tangential to the surface. These two different behaviors are shown in Figure 25a-d.

The sulfidation behaviors differ not only macroscopically but also at a smaller scale. As shown in Figure 25e, it is obvious that the behavior of the γ – γ’ microstructure at the sulfide front is different. In the case of Alloy1 and Alloy1+Hf, a clear boundary between the sulfide and the unaffected substrate is established, and the alloy retains its original γ – γ’ microstructure. Whereas in the case of Alloy1+Si and Alloy1+HfSi, there appears to be a gradient of dissolution of the γ’ near the sulfide front rather than a clear boundary.

Furthermore, sulfides in Alloy1 although mainly chromium sulfide, do incorporate some titanium, tantalum, and nickel. The addition of hafnium increased the amount of these elements present in the chromium sulfides, while the addition of silicon lowered it. Adding both hafnium and silicon decreased their content the most and exhibited the best hot corrosion resistance. The compositional differences of the sulfides formed for Alloy1 and Alloy1+HfSi are shown in Figure 25a-d.

The elements being incorporated in the rapidly penetrating sulfides, identified through EDS analysis, observed in Alloy1 and Alloy1+Hf are γ’ formers. The presence of these elements in the sulfides as well as the large penetration depths points to the easy and quick dissolution of the γ- γ’ structure. As the attack progresses, chromium is removed from the substrate and incorporated in both the oxides and the sulfides. The removal of enough chromium from the substrate can disrupt the γ- γ’ structure causing the γ’ precipitates to dissolve releasing titanium, and tantalum that are now free to sulfidize. The amount of chromium that would need to be removed from the substrate to disrupt its structure is dependent upon the stability of both the γ matrix phase and the γ’ precipitate phase. In this case, silicon acts as a stabilizer, allowing for the γ’ phase to be stable along a wider range of compositions and therefore preventing the release of large amounts of γ’ formers and their incorporation into the sulfides.

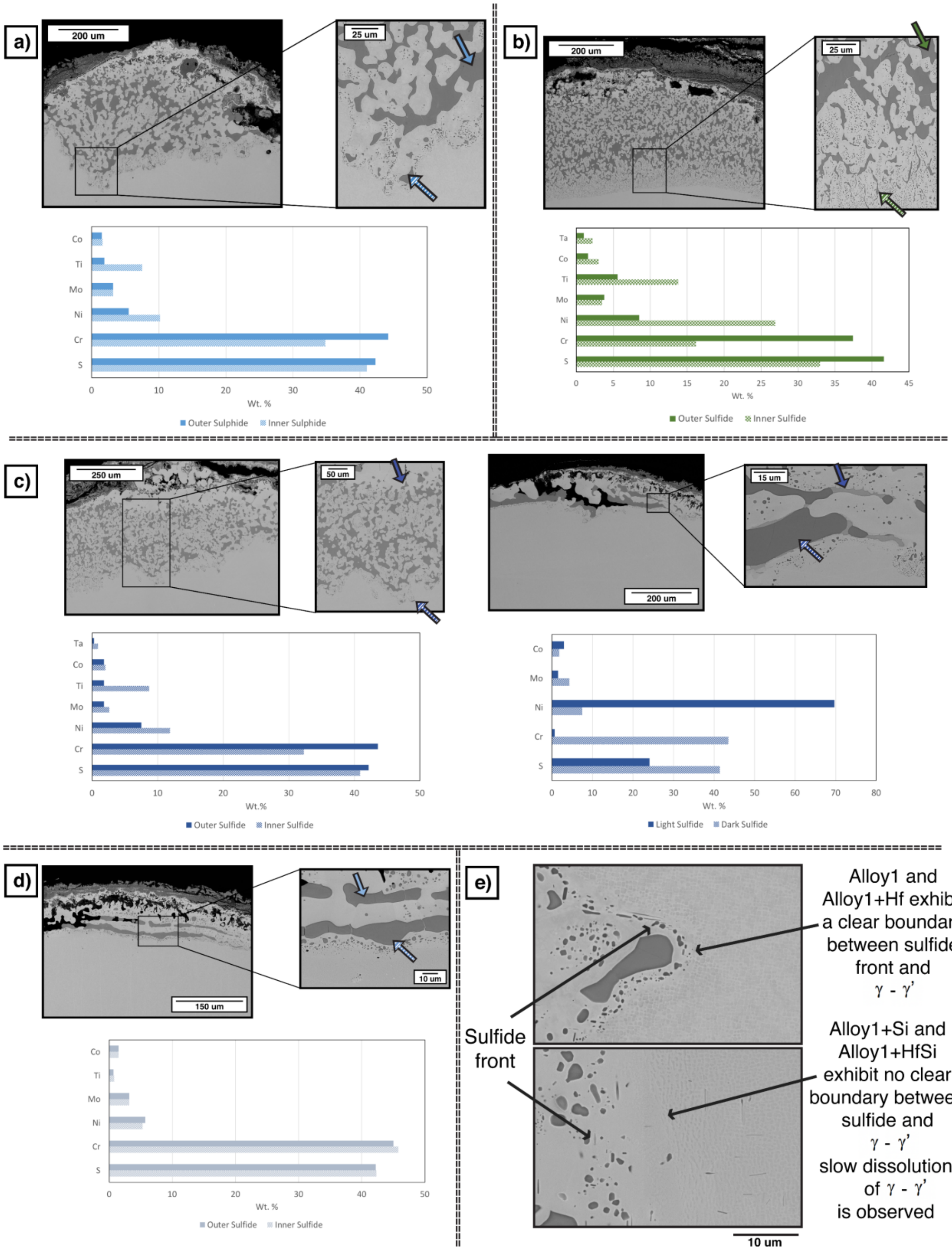

FIGURE 25. Backscattered SEM images and elemental analysis of the internal sulfidation attack observed in a) Alloy1, b) Alloy1+Hf, c) Alloy1+Si where two different morphologies of attack where observed, d) Alloy1+HfSi, and e) microstructural differences exhibited by the different materials at the sulfide front.

4.3.2.4 Oxidation Behavior

Sulfidation resistance is key in the overall hot corrosion resistance of any alloy. However, the first layer of protection is provided by the thermally grown oxide, and it therefore plays a very critical role in preventing and/or slowing down the hot corrosion attack. Figure 26a and 26b shows EDS maps for Alloy1 and Alloy1+HfSi, respectively. Alloy1, although forming a continuous chromia layer, also incorporates significant amounts of titanium and tantalum into the oxide layer. Alloy1+HfSi on the other hand shows significantly lower amounts of titanium and tantalum along that oxide layer. Oxide grains rich in titanium are present along the outer edge of the oxide scale in Alloy1+HfSi, but the continuous protective layer has significantly less titanium than the one seen in Alloy1. Figure 26 shows that the compositional differences seen along the oxide layer are consistent with those seen in the internal sulfides. The sulfidation-oxidation attack experienced during hot corrosion makes it so that once incorporated into the internal sulfides, tantalum, titanium and nickel can diffuse outward, and due to their fast kinetics, contribute to the overgrowth of a non-protective oxide layer on the surface of the sample. The fast formation of this non-protective oxide promotes further inward diffusion of sulfur into the substrate exacerbating the internal sulfidation of the superalloy and its overall consumption.

The average composition of the continuous oxide layer was measured through EDS for all four materials, and it is summarized in Figure 27. The hot corrosion resistance of the four materials matches the trends observed in the chromium and titanium contents with the best performing alloy having the most chromium and the least titanium.

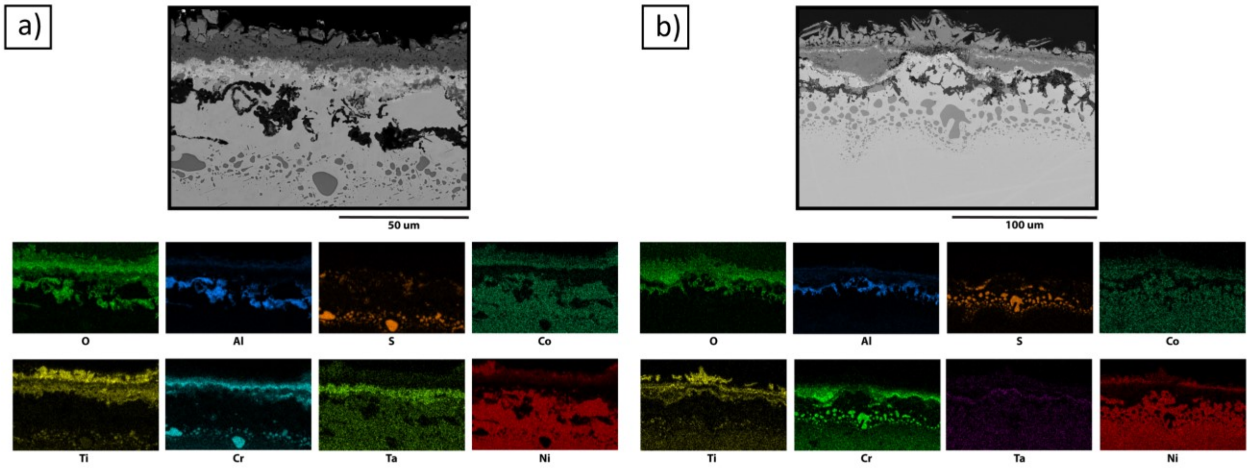

FIGURE 26. Backscattered SEM images and EDS maps of the oxide formed on a) Alloy1, and b) Alloy1+HfSi.

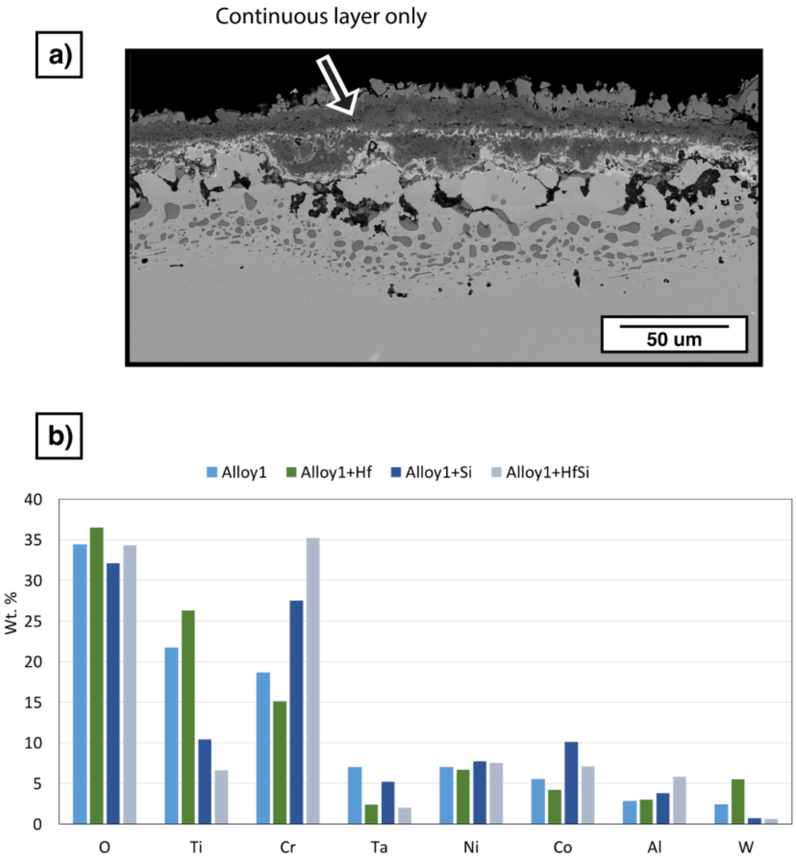

FIGURE 27. a) Backscattered SEM image of the oxide formed on Alloy1+HfSi where the continuous oxide layer, the part that was analyzed for elemental composition is highlighted, b) Summary of the oxide's elemental analysis.

Composition of the oxide is not the only important aspect when evaluating the quality of a protective oxide layer, the morphology is equally important. Small differences in the overall morphology of the oxide formed are observed and showcased in Figure 28. Alloy1, as well as Alloy1+Hf, appear to have a thinner layer of the desired chromium oxide. Even though all variations of Alloy1 exhibit the formation of non-protective outer oxide grains rich in titanium, and nickel in the case of Alloy1+Si and more so in Alloy1+HfSi, these are for the most part on the surface of a much more protective continuous layer of chromium oxide, as shown in Figure 28.

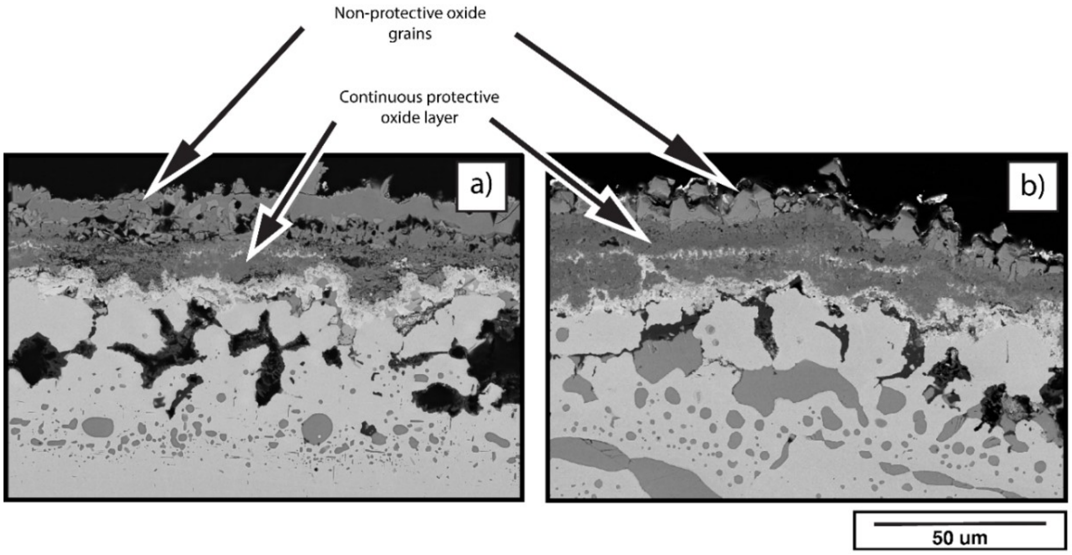

FIGURE 28. Backscattered SEM images highlighting oxide morphology of a) Alloy1+Hf, and b) Alloy1+HfSi.

In order to fully understand the progression of the attack and the underlying mechanisms behind the formation of the corrosion products being observed, a shorter exposure was performed.

4.3.2.2 10-hour Low-Velocity Burner Rig Exposure

The surface of the hot corroded materials showed interesting differences after a 10-hour exposure as seen in Figure 29a. Alloy1 showed a highly uniform oxide with a few anomalies, Alloy1+Hf showed more prominent elemental segregation along the dendrites as well as oxide anomalies. Alloy1+Si exhibited no oxide anomalies, but a high degree of elemental segregation along the dendrites. Alloy1+HfSi showed interesting results where the degree of elemental segregation along the dendrite varied with location, and it did not exhibit any surface anomalies.

Data on the average composition of the oxide formed was collected through EDS, and it is summarized in Figure 29b. At this early stage, the chromium content in the oxide shows no significant differences from one alloy to another. The titanium and nickel contents on the other hand do exhibit different trends, especially in the case of Alloy1+Hf where the nickel content is twice as much as in any of the other alloys, and the amount of titanium present is significantly lower. Since most of the nickel within the oxide is contained in the outer oxide grains, this suggests that during the early stages of attack, outward nickel diffusion is much faster in Alloy1+Hf than in the other three alloys.

Close examination of the oxide in cross-sectional view reveals the different nature of the oxide formed as seen in Figure 30. More importantly, it reveals the substrate’s internal reaction to the hot corrosion attack providing insight to different mechanisms taking place during the early stages of exposure. At this early stage of the attack, no sulfides have formed, and internal attack is limited to oxidation. The differences in oxide morphology and adherence between the different doped alloys can be evaluated by visual inspection of the cross-sections. Other parameters, such as internal oxidation and vertical cracking of the oxide, are harder to evaluate by observation only. Therefore, efforts were focused on quantitative analysis of the hot corrosion attack to facilitate comparison between materials. The parameters measured are summarized in Table 6.

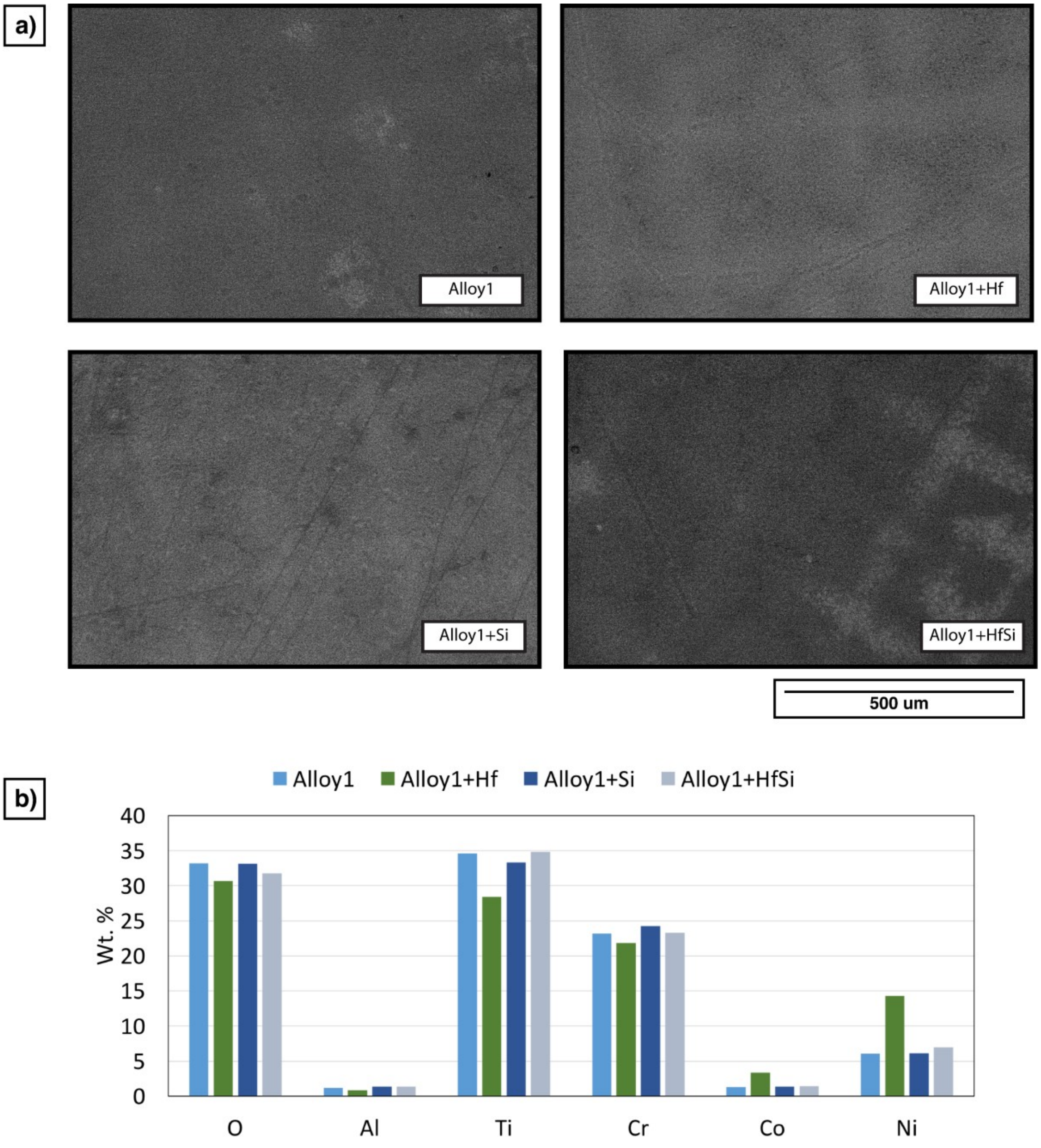

FIGURE 29.a) Backscattered SEM images of the surface Alloy1 and its doped variations after a 10-hour LVBR exposure, and b) average composition of the oxide formed.

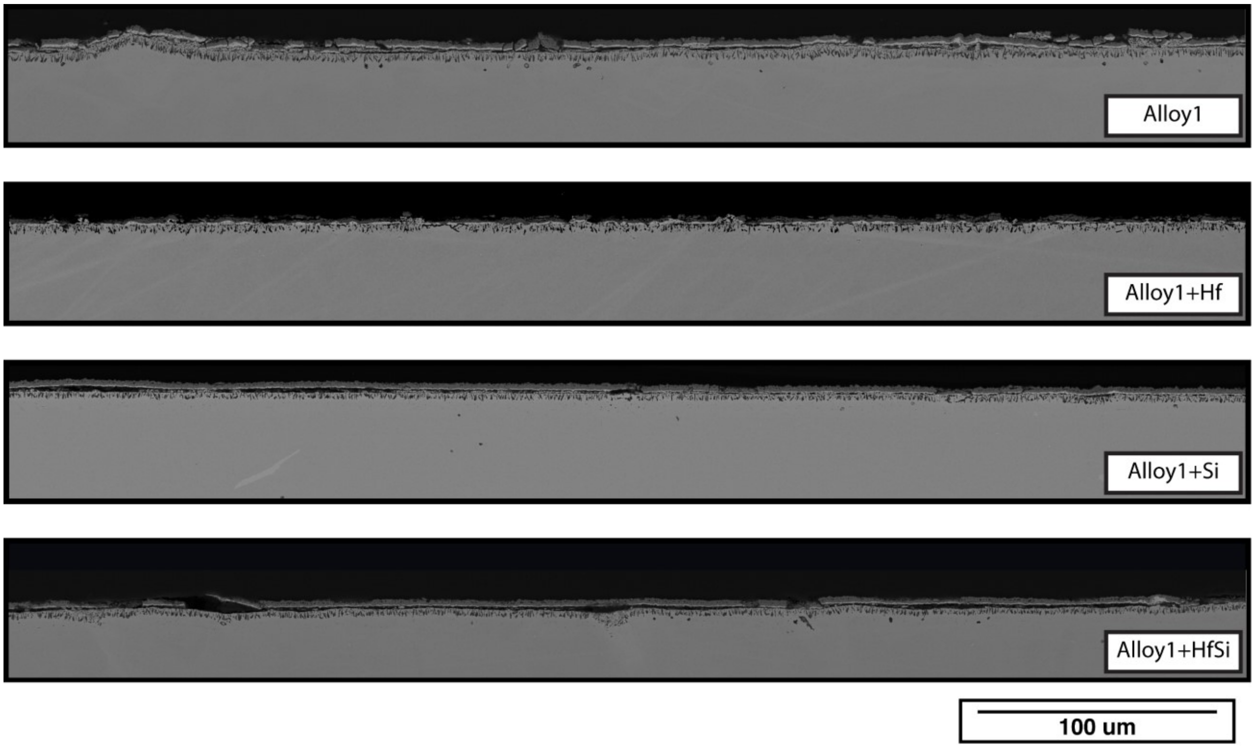

FIGURE 30. Backscattered SEM images of cross-sections of Alloy1 and its doped variations after a 10-hour LVBR exposure.

TABLE 6. Summary of cross-sectional analysis of the oxide formed on Alloy1 and its doped variations after a 10-hour LVBR exposure.

	Alloy1	**St. dev**	**Alloy1+Hf**	**St. dev**	**Alloy1+Si**	**St. dev**	**Alloy1+HfSi**	**St. dev**
Oxide Thickness (µm)	3.39	0.57	2.10	0.58	2.95	0.45	2.73	0.32
Internal Oxidation Depth (µm)	6.89	1.22	5.20	0.96	4.76	0.71	4.51	1.88
Crack to Crack Distance (µm)	15.76	19.34	7.79	4.14	431.18	57.65	85.33	88.15
Delamination %	100	NA	41	NA	100	NA	100	NA

Oxide thicknesses are similar for all four materials. Nevertheless, the variation in thickness along a given oxide can give insight to its quality and ability to protect the alloy from further attack. Alloy1 exhibited the thickest oxide as well as the largest standard deviation pointing to a more non-uniform oxide. The addition of hafnium decreased the oxide thickness the most but did not improve the variations in thickness. This finding is consistent with the proposed theory that hafnium segregates to grain boundaries and slows down diffusion and therefore, the oxidation rate [87]. The addition of silicon results in a small decrease in the thickness of the oxide, likely to due to silicon aiding in the formation of a slightly more protective oxide (less cracking observed), as well as decreased thickness variation. Lastly, the presence of both dopants results in the smallest variation of oxide thickness and an average thickness in between that of Alloy1+Hf and the Alloy1+Si, pointing to the formation of a uniform protective oxide.

Internal oxidation depths can provide insight into the diffusion mechanisms taking place. During any process that involves oxidation, two different processes can take place: internal and external oxidation. Whichever takes place is dependent on which species has the fastest diffusion rate. Internal oxidation happens when oxygen diffuses into the material and oxidizes the metal, while external oxidation happens when a cation diffuses out and is oxidized at the outer oxide interface. However, penetration depth is not all that matters when evaluating internal oxidation, looking at the morphology of the oxides formed is equally important. If the internal oxides form as individual precipitates, then the internal oxidation process is simply depleting the alloy of the oxidized element and contributing to the fast consumption of the substrate. On the other hand, internal oxidation that results in a continuous or semi-continuous layer can provide protection from further oxidation and/or sulfidation. Alloy1 had the deepest internal oxidation with an average penetration depth of about 7 microns, roughly double the thickness of the oxide layer.

The addition of hafnium decreased both the average penetration as well as its standard deviation pointing to a less detrimental internal oxidation process. This decrease in internal oxidation can be attributed to hafnium's ability to reduce diffusion across the oxide's grain boundaries [88]. The addition of silicon decreases the penetration depth even further and the oxide morphology appears more uniform and in the process of forming a continuous layer. The presence of both dopants decreases the penetration depth the most, but it does result in a larger standard deviation than that of all other materials. This is illustrated in Figure 30 where the internal oxidation occurs uniformly across large stretches, but areas of irregular deeper penetration can be observed.

The average distance from vertical crack to vertical crack was calculated as a way to measure the integrity of the oxide layer. Vertical cracks that penetrate the entirety of the oxide layer provide fast diffusion paths for oxygen and sulfur to further consume the underlying substrate. Large cracks can also provide a place for molten salt to accumulate and exacerbate the hot corrosion attack. The crack-to-crack distance in Alloy1 was 15 microns, a relatively small value giving a high frequency of cracks, which can be seen in the many cracks visible along its oxide in Figure 30. The addition of hafnium had a detrimental effect on the integrity of the coating decreasing the crack-to-crack distance to about half that of Alloy1. Alloy1+Si had the largest distance between vertical cracks increasing it by a factor of 27. This is not surprising, since silicon has been showed to improve the hot corrosion resistance of Ni-based materials by extending the stability range of both chromium and aluminum oxide [89]. When both dopants were present, the crack-to-crack distance was only increased by a factor of 5, suggesting that although the beneficial effects of silicon are still present, they are reduced significantly by the presence of hafnium resulting in a net minimal improvement.

A strong oxide/substrate interface is critical for good hot corrosion and oxidation resistance, since delamination, or detachment of the entire oxide at the oxide/substrate interface, is a concern under these conditions. Unfortunately, for the observed samples, three out of the four materials exhibited almost complete delamination of the oxide layer. The exception being Alloy1+Hf, which was able to retain about 40% of the oxide/substrate interface. This does not come as a surprise since hafnium has been shown to increase oxide adhesion [88]. The proposed mechanisms behind this improvement include the formation of hafnium oxide pegs spanning from the oxide layer to the substrate helping to secure it in place, and the segregation of hafnium to grain boundaries that help prevent further diffusion.

4.3.2.3 Effect of Pre-Oxidation on Hot Corrosion Resistance

The exact environment experienced within a turbine is dynamic and impossible to accurately predict. Therefore, it is very important to test materials under varying conditions to cover the entire range of possibilities. Hot corrosion attack is reliant on the presence of outside contaminants, and therefore, depending on the turbine engine application and location, it is possible for materials to experience exposure to oxidation conditions prior to hot corrosion attack. Consequently, understanding the effect that different pre-oxidation conditions have on the hot corrosion resistance of materials is an important step in evaluating new materials.

4.3.2.3.1 Analysis of Oxide formed during Pre-Oxidation Steps

The surface of the oxides formed during the two different pre-oxidation conditions are shown in Figure 31.

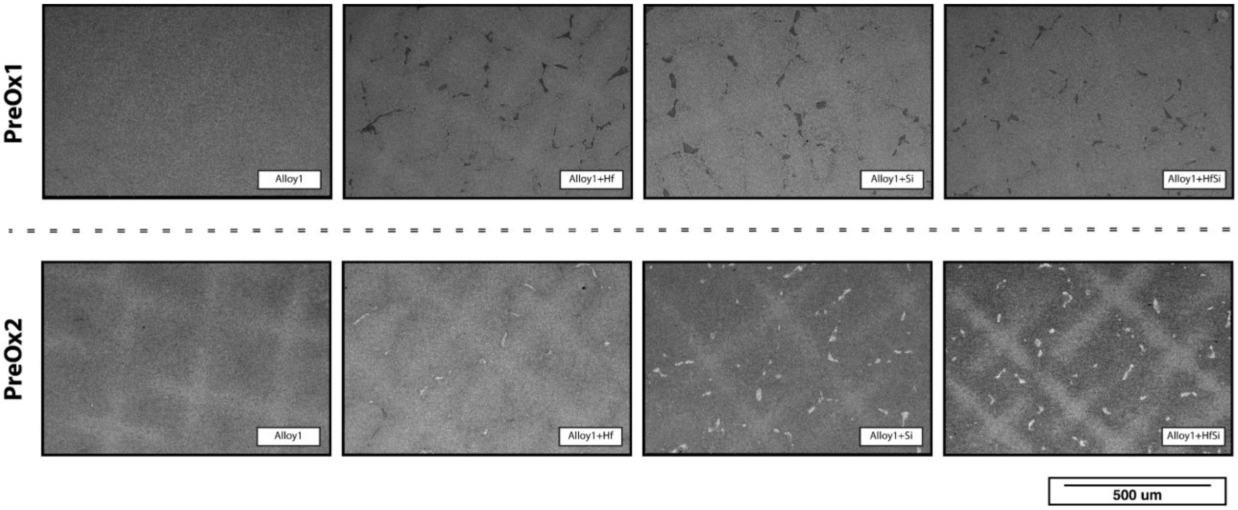

FIGURE 31. Backscattered SEM images of the surface of Alloy1 and its doped variations after two different pre-oxidation treatments.

4.3.2.3.1.1 Pre-Oxidation Condition I – 15 minutes

At this stage, Alloy1 shows a very uniform oxide layer, and no elemental segregation is observed. The three doped variants on the other hand show a very different behavior. In all three cases non-uniform oxides are observed, where the dendritic segregation is mapped onto the oxide, and the interdendritic space forms a different oxide to that of the bulk. Closer examination of the three doped materials revealed that at this early stage, the oxide formation allows for the retention of the γ- γ’ pattern, both along the dendrite core and the interdendritic space as shown in Figure 32. Elemental analysis showed that the darker oxides shown along the interdendritic spaces are titanium rich, consistent with the composition of γ -eutectic observed in the as-processed materials.

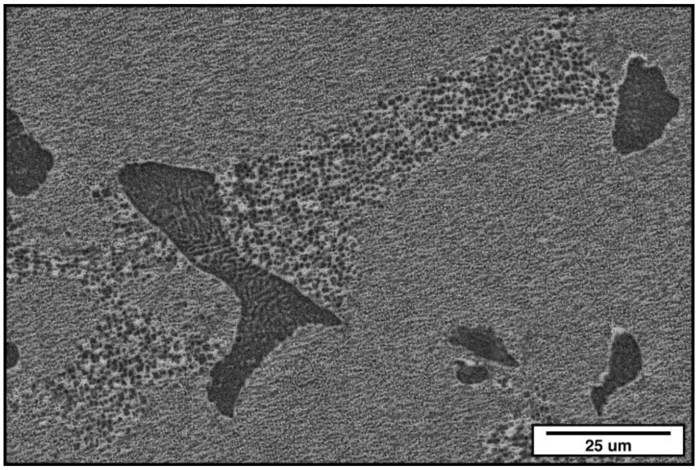

FIGURE 32.Backscattered SEM image of the surface of Alloy1+HfSi after pre-oxidation treatment PreOx1, showing the oxide formed retains the γ – γ' pattern of the substrate.

Short term oxidation of the three doped materials resulted in very similar general behavior. Nonetheless, the presence of hafnium did have a differentiating effect. Both variations containing hafnium exhibited areas where hafnium oxide can be observed surrounded by the overgrowth of titanium oxide grains, as shown in Figure 33. The hafnium oxide can be observed in Figure 33b as the bright phase, while the darker phase is titanium oxide. These hafnium oxide disruptions of the oxide morphology were observed in both materials in similar size and numbers. Even though their presence was not significant, under 10 occurrences in an area of over 30 mm^2, it could offer a weak zone for hot corrosion attack to penetrate the material more rapidly. Alternatively, the overgrowth of titanium oxide in these areas could accelerate delamination of the oxide exacerbating the depletion of viable material.

Examination of oxide cross-sections obtained through focus ion bean revealed that the thickness of the oxide grown ranged from 100 to 200 nm.

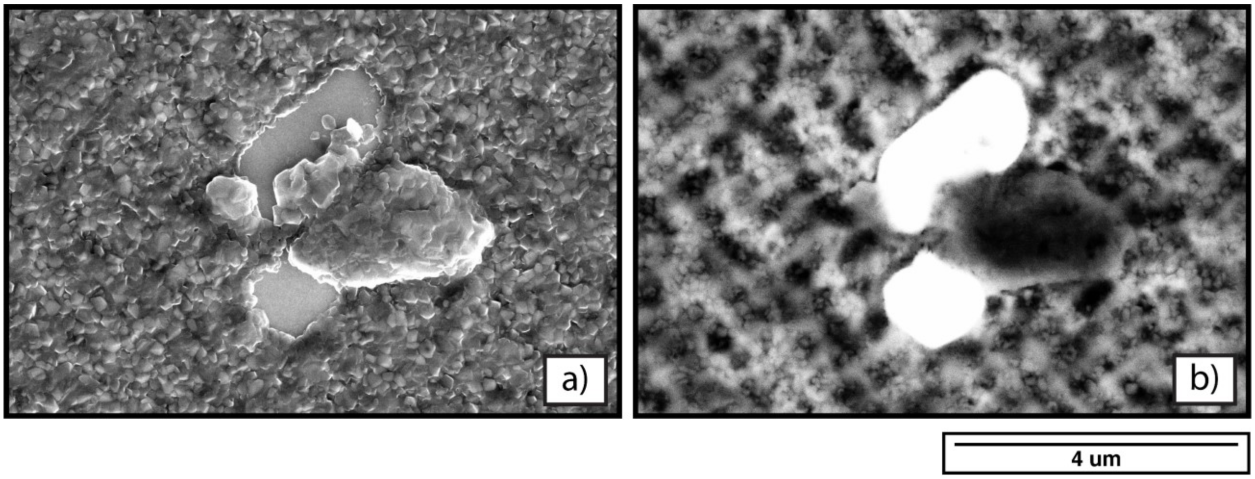

FIGURE 33. SEM images of the oxide formed on the surface of Alloy1+Hf after pre-oxidation treatment PreOx1 imaged under a) secondary mode, and b) Backscattered mode. Areas around hafnium oxide (shown in bright) exhibit extreme growth of titanium oxide (shown in dark).

4.3.2.3.1.2 Pre-Oxidation Condition II – 1 hour

At this longer oxidation time, the oxide formation no longer allows for the retention of the γ- γ' pattern that was seen at the shorter times. Furthermore, the oxide formed on all four materials exhibits dendritic elemental segregation, and the areas previously exhibiting titanium oxide are now exhibiting nickel oxide grains that appear to have grown on the surface of the titanium oxide, as seen in Figure 34a. This was confirmed through STEM work shown in Figure 34b.

The hafnium oxide formations seen in the shorter exposures are no longer present in either material. Examination of oxide cross-sections revealed the oxide thickness to range from 0.5 to 1.7 microns.

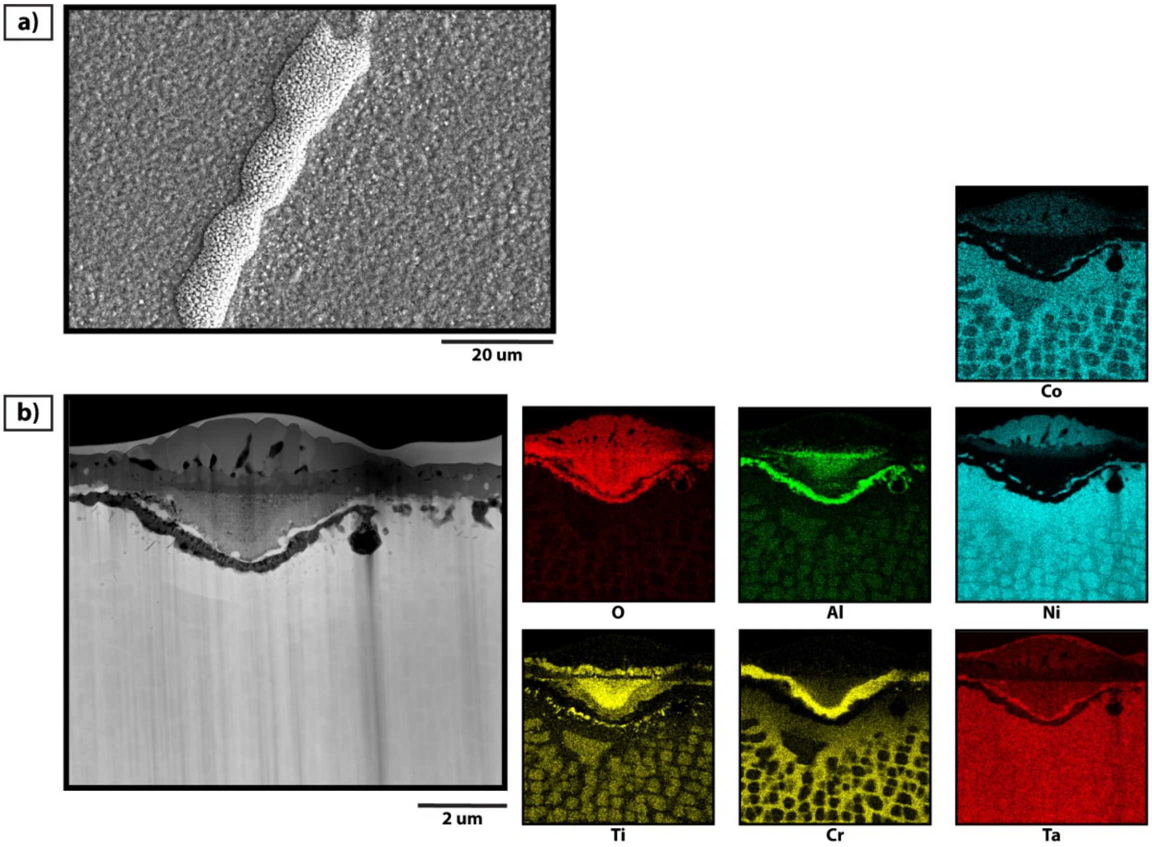

FIGURE 34.a) Secondary SEM image of oxide formed on the surface of Alloy1+Si after pre-oxidation treatment PreOx2, and b) Darkfield STEM image of the oxide cross-section with elemental maps.

4.3.2.3.2 10-hour Low-Velocity Burner Rig Exposure of Pre-Oxidized Samples

The surface of the exposed samples is shown in Figure 35. Dendritic segregation is still visible after exposure, particularly for Alloy1+Si and Alloy1+HfSi. The oxide formed on Alloy1 exhibits the highest degree of uniformity for both pre-oxidation conditions. Alloy1+Hf appears mostly uniform with few anomalies in the case of pre-oxidation condition, PreOx1, but starts to exhibit interdendritic segregation in the case of pre-oxidation condition, PreOx2. The behavior of Alloy1+Si and Alloy1+HfSi is almost indistinguishable for each pre-oxidation condition. In the case of pre-oxidation condition, PreOx1, they both show an oxide with high levels of segregation within the interdendritic space. Pre-oxidation condition, PreOx2, on the other hand, exhibits an oxide with clear dendrite mapping, but no high levels of interdendritic segregation.

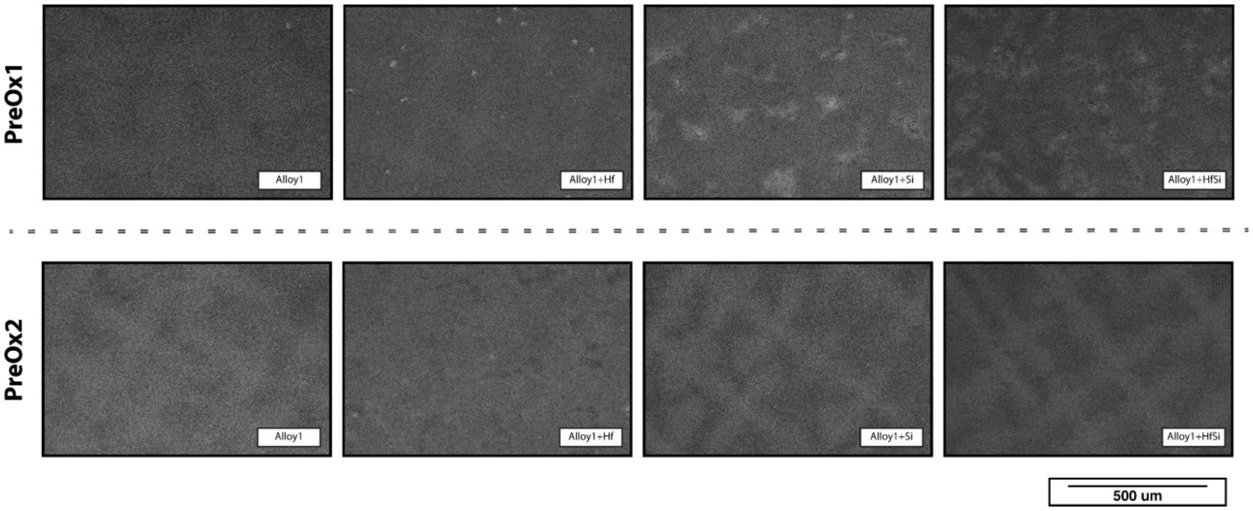

FIGURE 35.Backscattered SEM images of the surface of pre-oxidized samples of Alloy1 and its doped variations after a 10-hour LVBR exposure.

4.3.2.3.2.1 10-hour Hot Corrosion Followed by Pre-Oxidation Condition I – 15 minutes

A short pre-oxidation step, even one where the oxide layer is not allowed to fully form and stabilize, is expected to help improve the hot corrosion resistance of a material, by accelerating the formation of a protective oxide on the surface. Polished cross-sections of the exposed samples are shown in Figure 36. Quantitative analysis of the oxide morphology is summarized in Table 7.

FIGURE 36. Backscattered SEM images of cross-sections of Alloy1 and its doped variations after pre-oxidation treatment PreOx1 followed by a 10-hour LVBR exposure.

TABLE 7. Summary of cross-sectional analysis of the oxide formed on Alloy1 and its doped variations after pre-oxidation treatment PreOx1 followed by a 10-hour LVBR exposure.

	Alloy1	**St. dev**	**Alloy1+Hf**	**St. dev**	**Alloy1+Si**	**St. dev**	**Alloy1+HfSi**	**St. dev**
Oxide Thickness (µm)	3.02	0.73	2.06	0.32	3.14	0.28	2.62	0.36
Internal Oxidation Depth (µm)	8.64	1.41	3.80	1.23	5.23	1.29	4.55	1.16
Crack to Crack distance (µm)	6.45	3.90	11.34	4.32	no cracks	NA	77.96	32.82
Delamination %	59.17	NA	43.87	NA	0.00	NA	31.06	NA

The small improvements provided by the short pre-oxidation step are best exemplified in the decrease of overall delamination percentage in three of the four materials, Alloy1+Hf being the exemption and exhibiting almost no change in it. The distance between vertical cracks decreased for Alloy1 and Alloy1+HfSi, while it increased for Alloy1+Hf and Alloy1+Si. The changes in the crack to crack distance were for the most part minor, except for Alloy1+Si where it resulted in no major vertical cracks that penetrate the entirety of the oxide at all. The depth of internal oxidation was worsened for Alloy1 as well as for Alloy1+Si, improved for the Alloy1+Hf, and had no major change for the Alloy1+HfSi.

The hot corrosion resistance of all four materials measured after a 10-hour exposure showed small improvements when implementing a short 15-minute pre-oxidation step. The benefits obtained from the pre-oxidation step varied by material. In the case of Alloy1 although the delamination percentage decreased, the depth of internal oxidation increased and so did the number of vertical cracks. The hafnium addition on the other hand, experienced a decrease in the number of vertical cracks and the internal oxidation depth, but no change in the delamination behavior. Alloy1+Si experienced a great improvement in the delamination and vertical crack behavior, but it had a small increase in the penetration depth of internal oxidation. Alloy1+HfSi experienced minor variations in the penetration depth and vertical crack behavior, but significant improvements in the delamination behavior.

4.3.2.3.2.2 10-hour Hot Corrosion Followed by Pre-Oxidation Condition II – 1 hour

A longer pre-oxidation time where a more continuous and stable oxide layer is allowed to form, has beneficial effects on all four materials. These effects are easily observed through a visual analysis of the cross-sections’ SEM images, shown in Figure 37. Nonetheless, the same analysis performed in the previous section was applied, and the improvements observed were quantified and are presented in Table 8.

FIGURE 37. Backscattered SEM images of cross-sections of Alloy1 and its doped variations after pre-oxidation treatment PreOx2 followed by a 10-hour LVBR exposure.

TABLE 8.Summary of cross-sectional analysis of the oxide formed on Alloy1 and its doped variations after pre-oxidation treatment PreOx2 followed by a 10-hour LVBR exposure.

	Alloy1	**St. dev**	**Alloy1+Hf**	**St. dev**	**Alloy1+Si**	**St. dev**	**Alloy1+HfSi**	**St. dev**
Oxide Thickness (µm)	2.66	0.61	2.43	0.36	3.05	0.17	2.38	0.30
Internal Oxidation Depth (µm)	4.69	1.79	3.55	1.07	4.31	0.81	3.70	0.92
Crack to Crack distance (µm)	12.82	9.58	no cracks	NA	no cracks	NA	no cracks	NA
Delamination %	23.93	NA	0.00	NA	0.00	NA	0.00	NA

The percentage of delamination decreased to zero in three of the four materials with Alloy1 being the exemption. Even then, delamination decreased from 100% to 24%. The protective oxide formed during the pre-oxidation step was protective enough to reduce the overall internal diffusion of oxygen resulting in smaller penetration depths of internal oxidation for all four materials. Nonetheless, the new internal oxides presented a less uniform morphology, with areas exhibiting deep oxide precipitates, especially Alloy1+Hf and Alloy1+Si. Consequently, the variation in internal oxidation depth did increase for three out of the four materials with Alloy1+HfSi being the exception. The three doped versions of Alloy1 also exhibited great oxide integrity with no major vertical cracks that penetrated the entirety of the oxide. Alloy1 was the exception, experiencing a small decrease in the crack-to-crack distance. The small change in vertical crack formation can be attributed to the decrease in delamination, where in order to maintain the oxide-substrate interface some vertical cracks needed to be formed to relieve stress. Therefore, even though this parameter does not reflect it, the overall quality of the protective oxide did increase, just not to the same degree that it did on the other materials. On the other hand, the thickness of the oxide layers formed experienced little variation both from material to material as well as within each material.

When exposed to the longer pre-oxidation treatment followed by a 10-hour hot corrosion exposure, all four materials showed improved type I hot corrosion resistance. Under these conditions, Alloy1+HfSi resulted in the best performance with the smallest values of internal penetration depth, delamination and number of vertical cracks.

4.4 Conclusions

In summary, a new nickel-based superalloy and three doped variations were evaluated under type I hot corrosion conditions in a low-velocity burner rig as new substrate materials for turbine blades and vanes. The tests included both long-term and short-term exposures as well as pre-oxidized and bare materials. Minor amounts of hafnium and silicon doping, both individually and combined, affected the initial microstructure of the resulting superalloy both macroscopically and microstructurally, and therefore affected their overall performance.

In its as-processed form, Alloy1 exhibited interdendritic segregation with a small fraction of γ-eutectic observed. Its microstructure was composed of highly uniform and cuboidal γ' precipitates. The addition of hafnium to Alloy1 increased interdendritic segregation evidenced by an increase in the presence of γ-eutectic. On the other hand, the addition of silicon, and hafnium and silicon combined, decreased the observed interdendritic segregation. The shape and size of the γ'-precipitates were also affected by each of the different dopants. Hafnium doping results in less cuboidal and slightly smaller precipitates, while silicon doping results in less cuboidal and slightly larger precipitates. The doping of both hafnium and silicon results in less cuboidal precipitates that create highly directional paths in the γ matrix.

During the 500-hour hot corrosion exposure Alloy1 was not able to form a protective oxide, which resulted in extreme internal sulfidation and hot corrosion attack of this superalloy. The presence of hafnium negatively affected the hot corrosion resistance of Alloy1 by promoting further incorporation of titanium, and tantalum in both the sulfides and oxides formed. Additions of silicon increased the hot corrosion resistance through two mechanisms: a) by promoting chromia formation and suppressing the activity of titanium, resulting in a more protective oxide able to slow down internal sulfidation, and b) by promoting a different coarsening behavior of the internal sulfides. Even though it is clear that hafnium and silicon together have a synergistic effect, where the presence of hafnium enhances the effects of silicon and the overall hot corrosion resistance is significantly improved, further work is necessary to establish the specific mechanisms at play.

At shorter exposure times, the trends are similar, with both Alloy1 and Alloy1+Hf showing poor hot corrosion resistance evidenced by oxide delamination and cracking, and deep internal oxidation penetration depths. On the other hand, both Alloy1+Si and Alloy1+HfSi exhibit good oxide properties and material behavior with small differences between the two. At this early stage, Alloy1+Si has better oxide integrity marked by decreased cracking. Given that Alloy1+HfSi exhibited superior hot corrosion resistance during the longer exposure, it is proposed that the mechanisms differentiating the hot corrosion resistance of these two materials come into play during the later stages of attack. More studies are necessary where intermediate times are investigated in order to further understand the bifurcation in their behaviors.

The effects of two pre-oxidation treatments on the hot corrosion resistance of the alloys were also evaluated. In order to measure these effects and compare between alloys four parameters were chosen: oxide thickness, internal oxide penetration depth, oxide adherence, and distance between vertical cracks. It was found that a short 15-minute pre-oxidation step at 900 °C was beneficial to the hot corrosion resistance of all four alloys. The observed benefits varied from alloy to alloy, but oxide adherence was the most improved parameter across all materials. Increasing the pre-oxidation time to one hour increased the hot corrosion resistance of all four alloys further by enhancing all previously observed benefits. In both cases, the best performing alloy was still Alloy1+HfSi.

Further work is needed to fully understand the role of dopants in hot corrosion resistance. The first step is to fully understand the elemental segregation and formation of the $\gamma - \gamma'$ microstructure as a function of dopant and dopant level. More burner rig experiments where intermediate times are explored are needed to map out the materials' evolution. Lastly, specimens need to be evaluated under more dynamic conditions to fully explore the possible turbine environments. This includes, different pre-oxidation times and temperatures as well as implementation of different temperature profiles during hot corrosion exposures.

CHAPTER 5: A Low-Velocity Burner Rig Study of the Type I Hot Corrosion Resistance of Diffusion Coatings

5.1 Introduction

Nickel-based superalloys are currently used for most components in the hot sections of turbine engines [40]. Their mechanical properties at high temperature make them excellent candidates to fulfill this role. However, they are still susceptible to chemical and environmental attacks. Therefore, specialized protective coatings have been put in place to provide a barrier between the substrate and the harsh environment around it [50]. Protective coatings, their composition, microstructure, and deposition methods are an important area of research that continues to grow with every technological advance [51].

In order to perform their jobs as protective coatings they must be tailored to the specific environment they aim to protect against. Therefore, different coatings are developed for use in the many different types of turbines, such as power generation, aero, and marine turbines. In the case of marine turbines, the coatings must withstand corrosive environments created by the presence of salts in the intake air and/or fuel contaminants such as sulfur. High temperatures and the presence of salt contaminants prompt an accelerated oxidation attack known as hot corrosion, where molten salts cause dissolution of the protective oxide layer leading to the eventual penetration and sulfidation-oxidation of the substrate that leads to failure of the part. [25, 12]

The most commonly used coatings in marine turbines are what are known as diffusion coatings. In this case the coating is formed by incorporating aluminum onto the surface through diffusion. This results in a single-phase coating, with β-NiAl having a BCC or b2 structure and being stable over a wide range of compositions [52]. The high concentration of aluminum on the surface makes this coating very efficient at forming an external protective alumina layer. Further studies have focused on several modifications of this coating, with the addition of platinum yielding the best results due to an increase in oxide adhesion [90-93]. Therefore, platinum aluminide coatings have become an industry standard. Drawbacks of diffusion coating include a) limited composition, due to the nature of processing only few elements can be incorporated into the coating, and b) strong interaction with substrates requiring coatings to be tailored to each specific substrate.

This works aims to evaluate the type I hot corrosion resistance of 5 different substrate-coating systems optimized for the high temperature section of gas turbines in a low-velocity burner rig test. The coatings selected include three different types of diffusion coatings: slurry, AEP and pack cementation aluminides. The performance of these three different types of coatings will be assessed and compared in order to determine the best type of coating application process for the selected conditions. The best performing systems will be further analyzed in order to fully understand the coating/substrate interactions and coating degradation mechanisms. These parameters will be evaluated through two different approaches in an effort to not only further understand hot corrosion but to also improve upon current sample evaluation techniques used in the industry.

5.2 Experimental Methods

All samples evaluated were provided by Rolls Royce. Sample geometry and sample preparation are detailed in Chapter 2. The coating-substrate systems are summarized in Table 9.

The exact coating compositions are not provided due to them being proprietary. The compositions of the substrates studied are listed in Table 10.

TABLE 9. Summary of diffusion-based, substrate-coating material-systems tested.

Coating	Substrate
Pt-modified aluminide	CMSX-3
	CM186LC
AEP	IN792Hf
Slurry A	MM002
Slurry B	CMSX-3

TABLE 10. Substrate composition in wt. %

	Ni	Cr	Co	Mo	Al	Ti	Ta	W	Zr	C	B	Hf	Re
CMSX-3	65.7	8	5	0.6	5.6	1	6	8	…	…	..	0.1	…
CM186LC	62.6	6	9	0.5	5.7	0.7	3	8	0.005	0.07	0.015	1.4	3
MM002	60.7	8	10	…	5.5	1.5	2.6	10	0.03	0.15	0.015	1.5	…
IN792Hf	60.1	12.3	8.9	1.8	3.4	3.9	4	4.4	0.05	0.12	0.014	1	

All samples were evaluated in a low-velocity burner rig at 900 °C for 1000 hours with the experimental parameters detailed in Chapter 2. After exposure samples were handled following the procedures detailed in Chapter 2, and corrosion profiles were extracted and analyzed using the protocol described in Chapter 3.

5.3 Results

Five different material systems with diffusion coatings were investigated. Their performance in terms of coating loss due to corrosion attack is summarized in Table 11.

TABLE 11. Material loss and performance summary of all diffusion coatings tested.

	Starting Radius (µm)	Coating Thickness (µm)	Avg Penetration (µm)	Avg Penetration St Dev (µm)	Max Penetration (µm)	Good Coating Remaining (µm)	% Coating Lost
CMSX3 - Pt Aluminide	1607.15	19.65	-4.33	1.3	18.65	23.98	-22.05
IN792 Hf – AEP	1622.80	35.30	17.49	1.7	43.93	17.81	49.54
CM186LC - Pt Aluminide	1608.41	20.91	45.60	101.1	954.44	-24.69	218.05
MM002 – Slurry A	1600.37	12.87	28.76	2.6	82.65	-15.89	223.49
CMSX3 – Slurry B	1602.92	15.42	76.45	83.4	385.83	-61.03	495.90

Two different slurry coatings were tested, and both exhibited extremely poor hot corrosion resistance with the entirety of the coating and a significant part of the substrate being consumed. One AEP coating was tested, and it exhibited poor hot corrosion resistance losing about half of the original coating thickness. The same Pt-modified aluminide coating was evaluated on two different substrates, with one of these systems exhibiting excellent hot corrosion resistance and the other exhibiting poor hot corrosion resistance and penetration of the substrate.

The performance of the two systems with platinum aluminide coatings emphasized how critical the substrate/coating interactions are during long, high-temperature exposures. Furthermore, instead of losing coating material to corrosion, these systems experienced different degrees of swelling. The amount of swelling varied from sample to sample, and within each sample, it also varied with location, both in height along the pin as well as radially around it, with certain areas showing no swelling and others showing up to 20 microns. To explore this swelling effect, as well as the different performances, the two material systems with platinum aluminide coatings were examined closer.

5.3.1 Pre-Exposure Analysis of Platinum Aluminide Coatings

The two systems studied had different composition substrates, shown in Table 10, as well as different microstructures: CMSX-3 is a single crystal, while CM186LC is a directionally solidified cast superalloy. They both had the same type of platinum modified nickel aluminide coating applied to the surface: a low-activity aluminide outwardly grown CVD single phase coating. However, since diffusion coatings interact heavily with the substrate the resulting coatings had minor differences in composition, as shown in Figure 38.

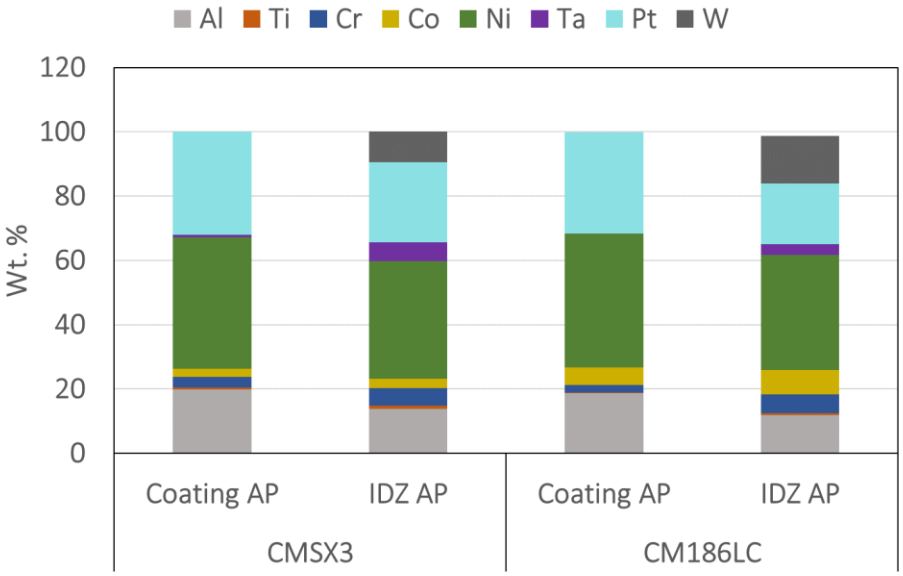

FIGURE 38. Plot of the as-processed (AP) composition of the outer coating and the interdiffusion zone (IDZ) for Pt-modified aluminide coatings deposited on CMSX-3 and CM186LC.

Small differences can be observed mainly in the amount of tantalum, chromium and cobalt that is incorporated into the coating from the substrate. The coating applied to CMSX-3 incorporated tantalum into the coating while its counterpart did not. The CMSX-3 coating also had a higher chromium content and lower cobalt content than the CM186LC coating. These trends are consistent with the composition of each substrate, CMSX-3 has a higher tantalum content as well as a lower cobalt content, and therefore, the resulting coating follows the same trend. The differences in composition are more evident when analyzing the interdiffusion zone, the area where the substrate/coating interactions take place. Similar trends can be observed, the interdiffusion zone (IDZ) in CMSX-3 has a higher tantalum content and lower cobalt content than that of the CM186LC coating, while the chromium contents are comparable. The biggest difference is in the tungsten levels in the two IDZ zones, which is surprising considering both superalloys contain the same levels of tungsten. This can be attributed to the heterogenous nature of CM186LC, where the carbides already present in the alloy facilitate the formation of more carbides and TCP phases along the IDZ.

The initial microstructures of the two platinum aluminides are shown in Figure 39. Both coatings are single phase β-NiAl. Although no major differences are observed in the outer layer of the coating, the compositional differences of the IDZ are apparent. The coating on CM1896LC has a higher tungsten content, which results in a higher concentration of refractory elements segregation and topologically closed pack (TCP) phases, shown in the bright phases along the IDZ in Figure 39.

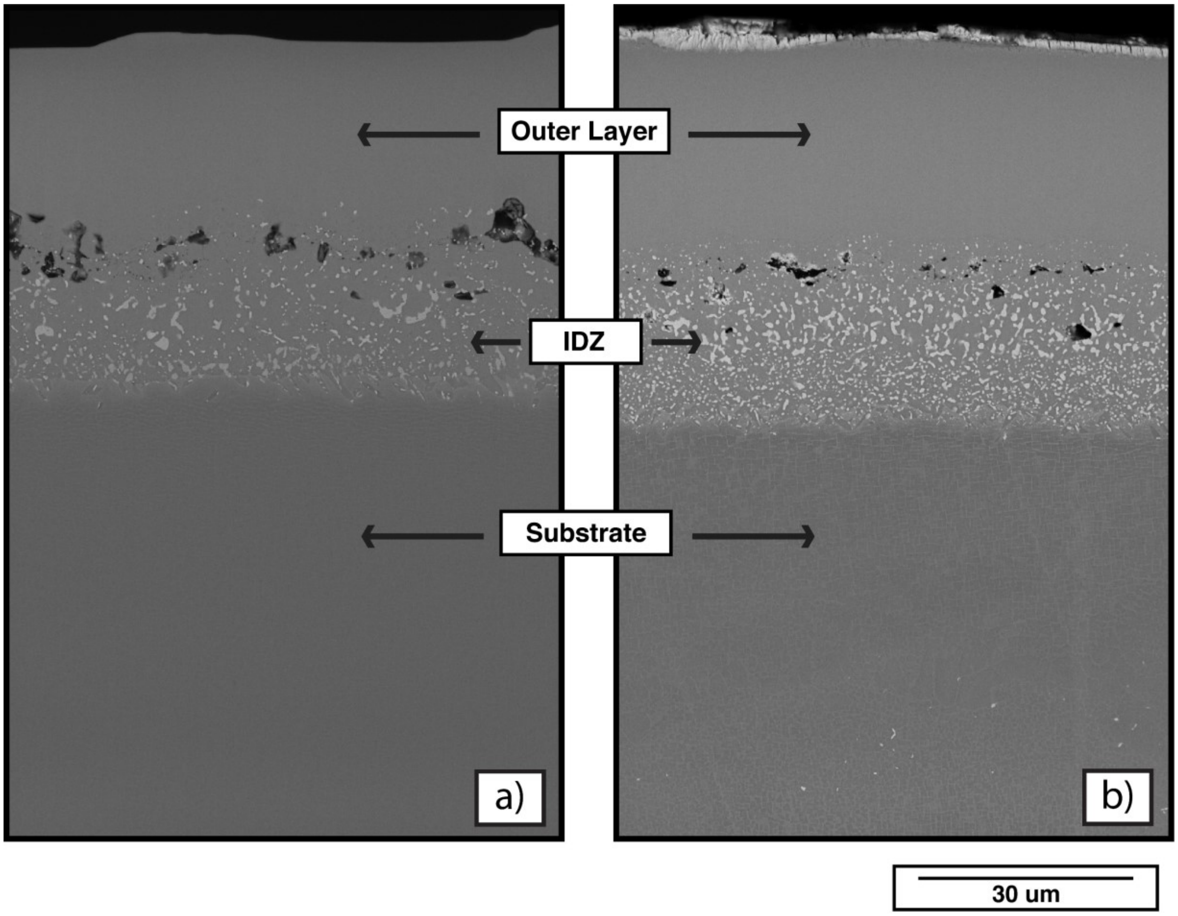

FIGURE 39. Backscattered SEM images of cross-sections showing the initial microstructure of the platinum modified aluminide on a) CMSX-3, and b) CM186LC. In the case of CM186LC more prominent segregation of refractory elements along the interdiffusion zone is observed.

5.3.2 Post-Exposure Analysis of Platinum Aluminide Coatings

After exposure, the two groups exhibited some similarities in general behavior, but differed in extent and rate of corrosion. The CM186LC system, with the directionally solidified substrate, exhibited a higher degree of corrosion, with 6 of the 15 cross-sections analyzed corroding past the coating and into the substrate. Only the 9 cross-sections where coating integrity remained were used to calculate the parameters for comparison to the CMSX-3 system. In this work, the traditional microstructural analysis of the remaining coating was complimented by a statistical study of the corrosion profile extracted through the in-house procedure detailed in Chapter 3.

5.3.2.1 Corrosion Profile

The methods described in Chapter 3 were applied to cross-sections of both Pt-modified aluminide coatings, and corrosion profiles were extracted. These profiles can be seen in blue in Figure 40, where the yellow line represents the original radius of the coating, and the red line represents the coating-substrate interface.

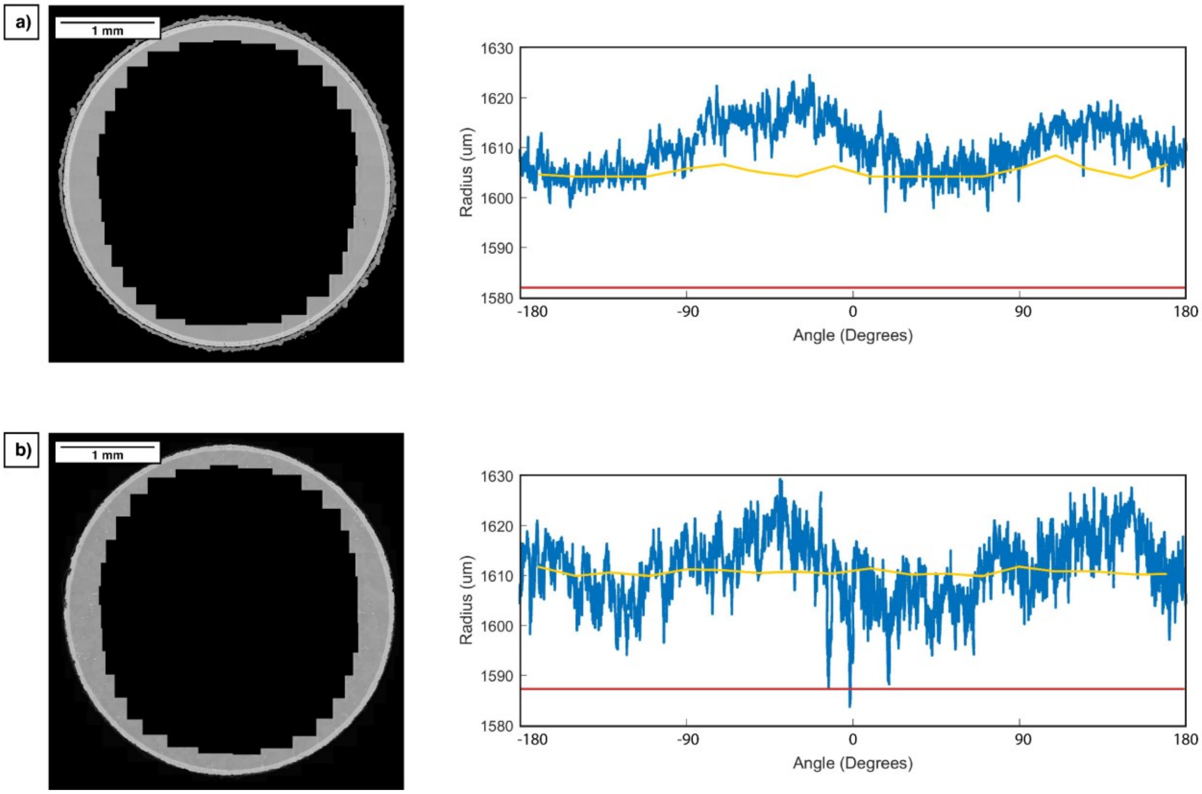

FIGURE 40. Examples of reconstructed images and plot of corresponding corrosion profile for the Pt-modified aluminide coating on a) CMSX-3 and b) CM186LC Extracted corrosion profile shown in blue, sample radius pre-exposure shown in yellow, and substrate/coating interface shown in red.

A notable detail that immediately jumps out of the profiles shown in Figure 40 is the fact that there are certain areas of the coating that did not lose any material to the hot corrosion attack, but instead gained material. This swelling phenomenon could be easily identified and tracked through the new sample analysis protocol, which allowed accurate spatial tracking of the coatings' thicknesses. The visualization of the corrosion profiles was helpful in identifying the swelling phenomenon taking place. However, as data sets, the extracted profiles contain further information about the nature of the hot corrosion attack within each material system, and as such, they were statistically analyzed and probed. The next sections further discuss both a statistical analysis approach to hot corrosion evaluation as well as the conventional microstructural analysis of the exposed samples.

5.3.2.1.1 Parametrization of Corrosion Profile

Parametrization of the corrosion profile can help uncover information regarding the corrosion process that would otherwise be inaccessible with other evaluation protocols. Making use of the image analysis protocol detailed in Chapter 3, three different parameters were extracted for comparison: material loss, percent of cross-section exhibiting swelling, and tortuosity. Each parameter was extracted as an average of all top, middle and bottom cross-sections as well as a total average for all cross-sections in that group. A summary of the extracted parameters is shown in Table 12, and from these values, several conclusions can be reached.

TABLE 12. Summary of the parametrization of the corrosion profiles of the Pt-modified aluminide coatings.

Parameter	**CMSX-3 with Pt-mod Aluminide**	**CM186LC with Pt-mod Aluminide**
Average material loss - Top (µm)	-4.2	-0.68
Average material loss - Middle (µm)	-4.69	-2.65
Average material loss - Bottom (µm)	-4.09	-4.91
Average material loss - Average (µm)	-4.33	-2.75
% Swelled - Top	77.40	56.62
% Swelled - Middle	71.79	67.31
% Swelled - Bottom	75.25	77.10
% Swelled - Average	74.81	67.01
Tortuosity - Top	1.63	1.80
Tortuosity - Middle	1.49	1.56
Tortuosity - Bottom	1.25	1.33
Tortuosity - Average	1.46	1.56

5.3.2.2 Microstructural and Elemental Analysis

Figure 41 shows the microstructure of the remaining coating, IDZ and substrate for both material systems. Although the two coatings exhibited similar behaviors and microstructures in the outer layer of the coating, the two IDZs exhibited significant differences. In order to fully understand the different behaviors in these two systems further work was done to analyze and compare their compositional and phase evolution.

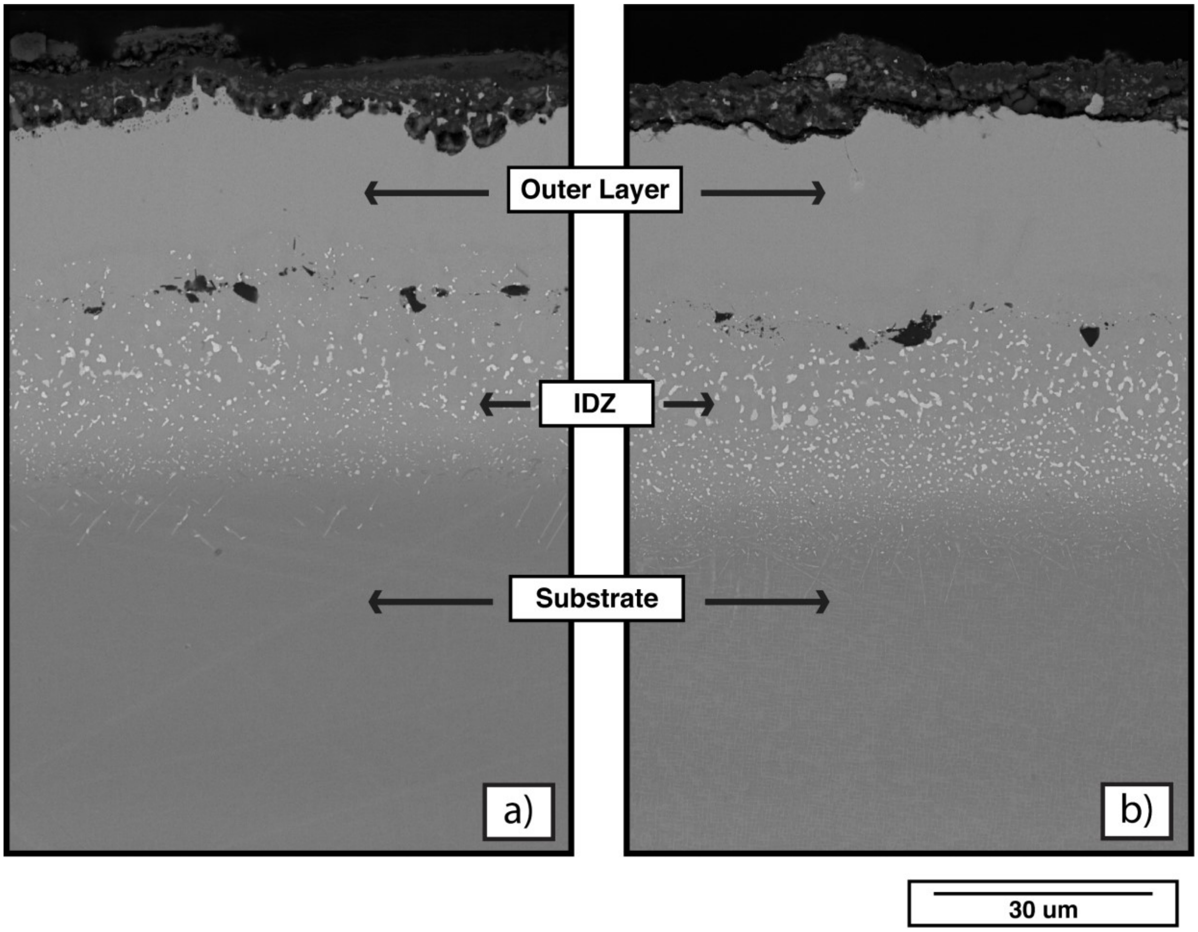

FIGURE 41. Backscattered SEM images of cross-sections showing the post-exposure microstructure of the Pt-modified aluminide on a) CMSX-3, and b) CM186LC.

5.3.2.2.1 Compositional Evolution

The average coating and IDZ compositions pre- and post-exposure were measured through EDS and the differences are shown in Figure 42. A lot can be learned from the different depletion patterns in these two coatings. The coating applied to CMSX-3 was depleted equally of chromium and aluminum, leaving behind a coating extremely nickel rich, with some excess platinum. The coating applied to CM186LC on the other hand, although depleted of both chromium and aluminum, had a higher aluminum depletion than that of chromium. In contrast to CMSX-3, the resulting CM186LC coating was more platinum rich with only some excess nickel.

The two IDZ experienced similar trends with respect to aluminum, chromium and nickel. However, the IDZ in CMSX-3 had a decrease in platinum content while the IDZ in CM186LC had an increase of it. Similarly, the IDZ in CMSX-3 had an increase in tungsten, while the IDZ in CM186LC had a decrease.

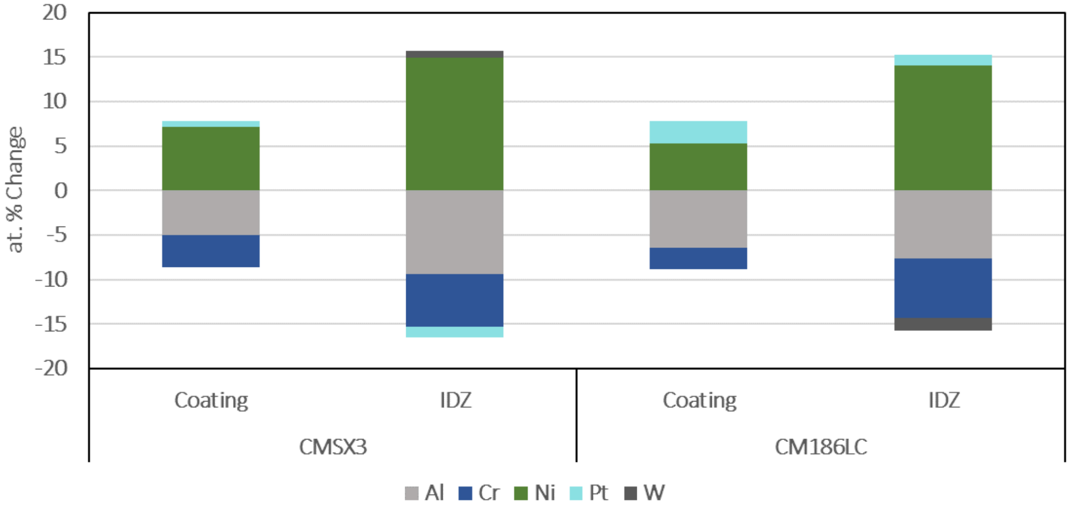

FIGURE 42. Plot of the difference between pre- and post-exposure compositions of the outer coating and the interdiffusion zone (IDZ) of the Pt-modified aluminide coatings deposited on CMSX-3 and CM186LC.

5.3.2.2.2 Coating Swelling

All platinum aluminides that retained coating integrity experienced coating swelling to some degree. A constant among all samples was not only the preferential swelling behavior but also the location of the swelling. The swelling was consistently observed at an angle of -45° and 135° from what was assumed to be the point of gas impingement on the samples, that is the point on the surface of the sample that is tangential to the rotating carousel acting as sample holder. Figure 43 is a schematic showing the location of the observed swelling with respect to the low-velocity burner rig testing environment. During the carousel’s rotation, detailed in Figure 43, there are moments where samples move towards the gas flow creating an effective gas velocity greater than the original gas flow. Due to the geometry of the testing environment and the rotational velocity of the sample holder, certain sample locations end up with a larger effective gas velocity than others. As it can be seen in the magnified insert of Figure 43, the areas where no swelling occurs are moving right into the gas flow when the effective gas velocity is the largest. By contrast, the areas where swelling is observed do not experience impingement during that time, but rather are in a position where the gas is allowed to flow above and below them. The locations with larger effective gas velocities correspond to the areas where material loss was observed. Therefore, the swelling was observed in the areas with the smaller effective gas velocities, where the hot corrosion process has not yet progressed to the same level of attack experienced by the areas where no swelling was observed due to consumption of the coating.

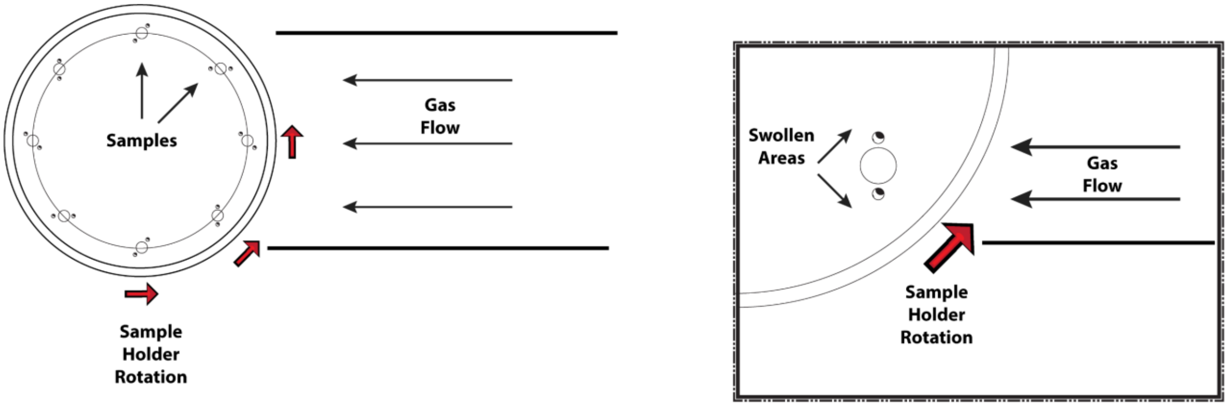

FIGURE 43. Schematic of sample holder rotation inside the exposure chamber.

A potential correlation between crystal structure and the swelling phenomenon (due to potentially enhanced diffusion along certain crystallographic directions) was also explored. However, the presence of this phenomenon on both a single crystal and a DS superalloy, along with the location of the swelling staying constant with respect to sample's location within the exposure chamber proved that the observed swelling was indeed a consequence of the gas flow and not of the crystal structure of the superalloys. The growth direction of TCP phases with respect to the swelling locations was also analyzed, and no correlation was found.

Further studies were performed on the CMSX-3 system to understand the swelling mechanisms. EDS was used to determine compositional differences between swelled areas and non-swelled areas. Analysis was performed on two different cross-sections, where four areas of interest where established within each of the two domains (swollen and non-swollen) for a total of eight areas of interest. Each area was divided into four regions: coating, interdiffusion zone (IDZ), secondary reaction zone (SRZ), and substrate, as shown in Figure 44.

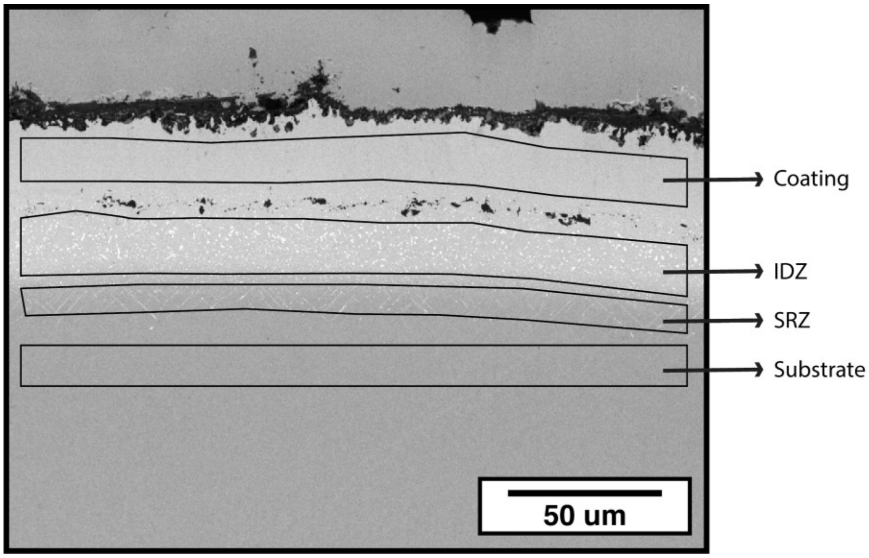

FIGURE 44. Backscattered SEM image of a cross-section showing the areas where elemental analysis was performed on the Pt-modified aluminide coating deposited on CMSX-3.

Compositional data were acquired at these four regions for each area of interest in the two cross-sections. Overall, results show that for the CMSX-3 system, areas that experienced swelling differ from the areas that did not experience swelling only in composition of the coating and IDZ region. The post-exposure compositions were compared to the as-processed material in order to obtain depletion levels, which are summarized in Figure 45.

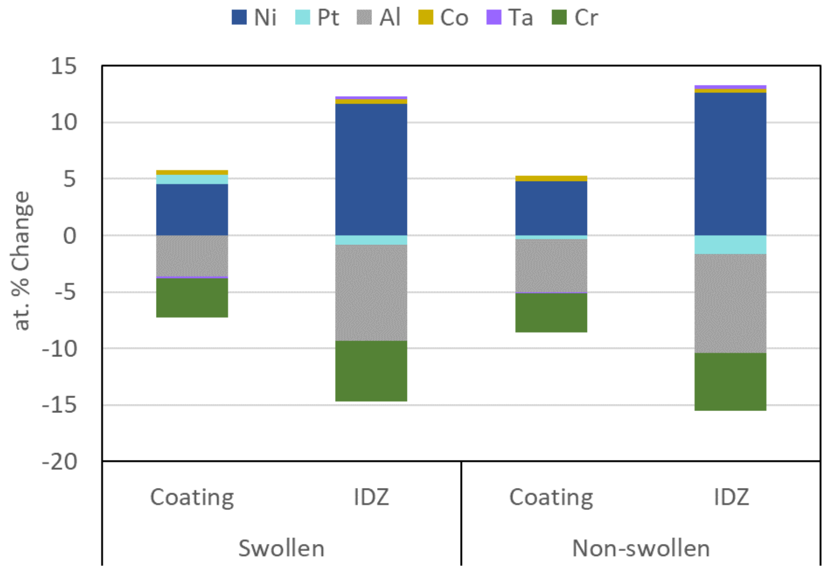

FIGURE 45. Plot of the compositions of swollen and non-swollen areas of the outer coating and the interdiffusion zone (IDZ) of the Pt-modified aluminide coating deposited on CMSX-3.

While the entirety of the coating experienced aluminum and chromium depletion that lead to a platinum and nickel rich coating, the extent of enrichment and depletion varied between swollen and non-swollen areas. Areas of the coating that experienced exacerbated swelling exhibited lower levels of aluminum depletion both in the outer coating as well as the IDZ. They also experienced platinum diffusion from the IDZ to the outer coating with little platinum consumption. The non-swollen areas on the other hand, experienced higher levels of aluminum depletion in both the outer coating and the IDZ, as well as platinum consumption evidenced by the depletion of platinum in both the IDZ and outer coating. Therefore, the differences in the degree of swelling observed can be explained by the different degree of coating consumption and depletion experienced in the different areas.

5.3.2.2.3 Phase Evolution

Close analysis of the exposed samples revealed the presence of both martensite and γ' phases, shown in Figure 46. Both of these phase transformations have been reported and studied in the literature and are consistent with the degradation mechanisms put forth for diffusion coatings [94-97]. During thermal cycling, the coating undergoes a reversible martensitic transformation. Upon cooling, the β-to-martensite phase transformation takes place, and upon heating the martensite-to-β phase transformation occurs [94]. The starting temperature (M_s) for martensite has been estimated to be around 600 °C, but it is highly dependent on the composition of the β phase, with increased nickel and platinum contents increasing the value of the M_s temperature [53]. Therefore, during high temperature exposures where aluminum is constantly being depleted, the increasingly nickel-rich coating experiences an increase in M_s temperature [96]. Coatings also experience a non-reversible phase transformation, where due to aluminum depletion, the β phase transforms to the lower aluminum-containing phase γ' [95]. This transformation is a result of aluminum depletion due to oxide formation as well as coating/substrate diffusion. The presence of the γ' phase is a sign of coating degradation due to it being less protective than the β phase [53]. Although these transformations have been thoroughly studied, most of the work has been carried out on aluminide coatings as bond coats for thermal barrier coatings (TBCs) and not as stand-alone coatings for hot corrosion protection. Therefore, the exposure environments vary from the one presented in this work.

Although the phases were present on both material systems, they were more prominent on the CM186LC system, where γ' was observed in most of the cross-sections analyzed as well as in more than 50% of the circumference of each of the samples. On the other hand, the γ' phase was only observed in less than half of the cross-sections characterized for the CMSX-3 system.

The martensite phase followed the same pattern, where it was more prominent in the CM186LC system than in the CMSX-3. The locations of both of these phases did not correspond to the areas that exhibit swelling nor did they follow any particular pattern around the circumference. However, the location of the γ' phase was consistent, showing up mainly along the IDZ for both material systems. Despite γ' being formed due to the aluminum depletion of the β phase, it shows a darker contrast than β when imaged in backscattered mode. This is due to the difference in platinum content. Although γ' is much lower in aluminum and higher in nickel than β, and therefore expected to show up as the brighter phase, it also has a lower platinum content than β and therefore, appears as the darker phase in Figure 46.

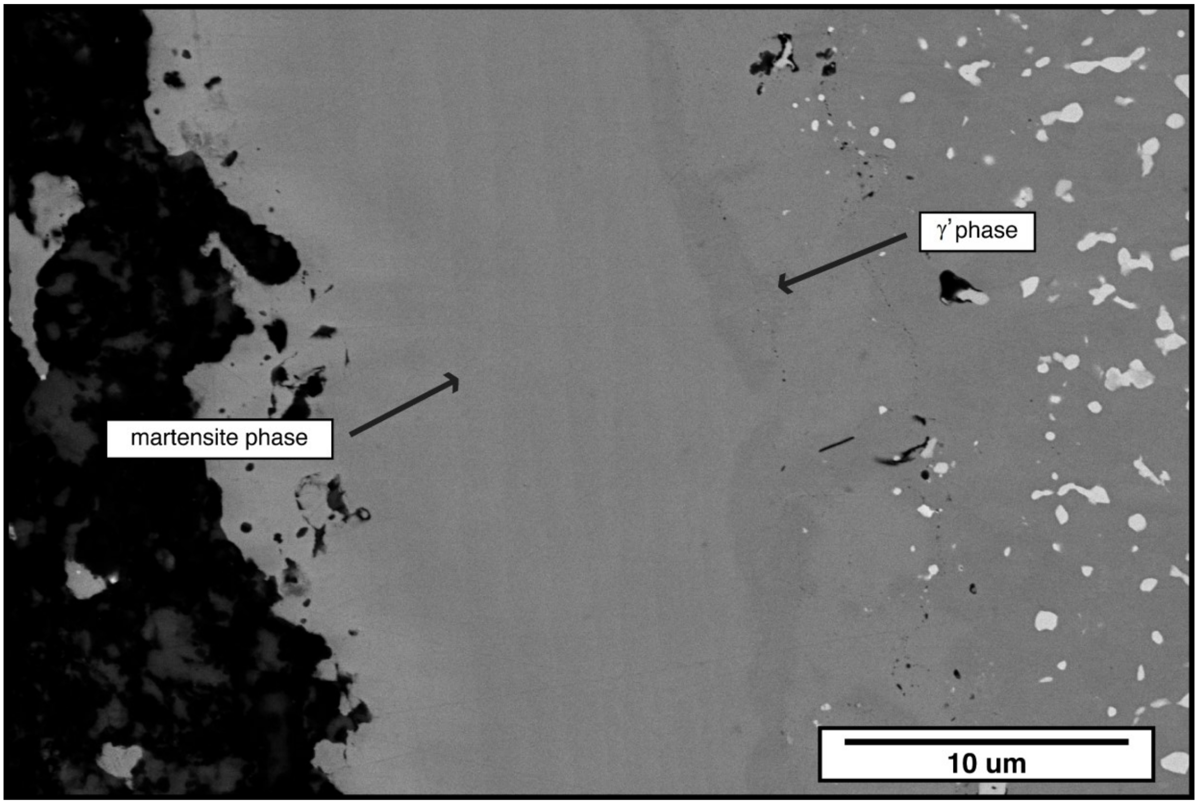

FIGURE 46. Backscattered SEM image of a cross-section of the Pt-modified aluminide coating deposited on CM186LC showing the formation of martensitic and γ' phases in the coating.

5.3.2.2.4 Oxides Formed

The average oxide composition for the two systems is shown in Figure 47. Although no significant differences are observed in the major constituents, the oxide formed on the CMSX-3 system does incorporate a higher content of small alloying elements, mainly titanium (not present in CM186LC's oxide), platinum, and constituents from the salt contaminant such as magnesium.

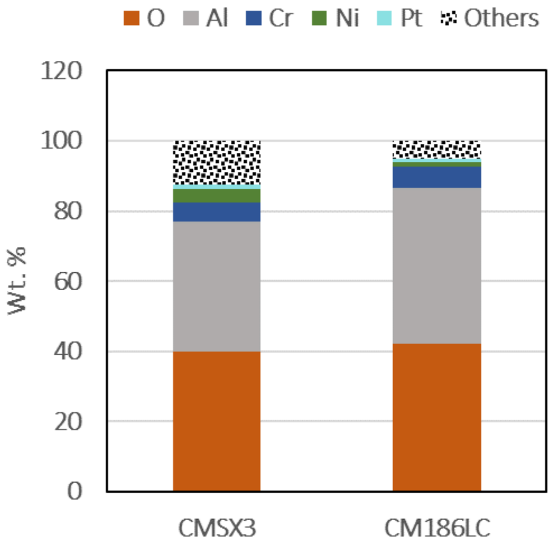

FIGURE 47.Plot of the composition of the oxide formed on the surface of the Pt-modified aluminide coatings deposited on CMSX-3 and CM186LC.

5.4 Discussion

The observations obtained from the two different approaches are consistent with each other, proving that the sample analysis protocol detailed in Chapter 3 is effective at evaluating the hot corrosion resistance of pin shaped samples.

The parametrization of the corrosion profiles facilitates the extraction of statistical parameters, that when appropriately matched to physical properties can help improve our understanding of hot corrosion. From Table 12, the first set of parameters summarizes the average material loss for top, middle, bottom, and all cross-sections. This parameter represents the differences between the average radius pre-exposure, and the average radius post-exposure. Material loss for all cross-sections is negative for both groups, indicating that instead of losing material to corrosion, the samples increased in average radius, or swelled during exposure. The CMSX-3 system experienced more uniform and more extensive swelling than that of the CM186LC system. The average material loss for the CMSX-3 system does not show any trend across the height of the pin, while the CM186LC system shows an increase in swelling from top to bottom of the pin. Because the observed swelling was not uniform around the entire pin, the percent of the cross-section exhibiting swelling was also calculated. This parameter follows a similar pattern as material loss. The CMSX-3 system exhibits swelling across a higher percentage of the cross-section as well as uniformity across the height of the pin. On the other hand, the CM186LC system exhibits an increase in the percent of the cross-section exhibiting swelling moving down the length of the pin and a lower overall percentage when compared to the CMSX-3 system.

Tortuosity, which is the ratio of the total length of the corrosion profile and the corresponding arc length, was calculated as a measure of the extent of corrosion, and quality of the coating/oxide interface. The CM186LC system exhibited larger values of tortuosity, but both groups followed the same trend with decreasing tortuosity down the length of the pin.

The CM186LC system is the more corroded material set, with only 9 cross-sections maintaining coating integrity. Based on these results, it is proposed that the pin shaped samples with Pt-modified aluminide coatings initially experience swelling that is uniform along the length of the pin and around the circumference of the pin, as seen in the CMSX-3 system. After the initial swelling stage ends, the corrosion-consumption stage begins, as seen in the CM186LC system. During this stage, the coating material experiences material loss due to corrosion. This corrosion-consumption stage is non-uniform along the length of the pin, with the top experiencing a more exacerbated process, and non-uniform along the circumference of the pin. The height dependency of the corrosion-consumption could suggest uneven distribution of the salt contaminant in the gas flow. On the other hand, the non-uniformity of both the swelling step as well as the corrosion-consumption is believed to be linked to the effective gas flow velocity.

Both the values for material loss and percent of cross-section exhibiting swelling support the mechanism explained above. Based on the trends shown in tortuosity values, it is proposed that the corrosion-consumption stage decreases the interface quality, marked by a higher tortuosity value. The top cross-sections, the ones that have experienced exacerbated corrosion-consumption, exhibit higher values of tortuosity and therefore, a more pitted surface. The bottom cross-sections on the other hand, have lower tortuosity values and therefore, retain a better surface morphology. Even though both groups show comparable tortuosity values, the CM186LC system does show higher overall values which is consistent with our proposed mechanism.

This proposed mechanism is consistent with what has been reported in literature [53], as well as the microstructural observations presented in this work. The first stage where swelling takes place can be explained by the large differences in aluminum and nickel contents between the coating and the substrate, which makes this type of coating-substrate system chemically unstable. The coating in question contains about 40 at. % aluminum, while the substrates contain only about 12 at.%. This type of concentration gradient along with the high temperatures experienced during use and/or experimental exposures enhance the diffusion between the substrate and the coating. Consequently, during the first stages of exposure nickel diffuses outward from the substrate to the coating which results in both an increase of the coating's thickness as well as an enrichment of nickel within the coating. This step is largely influenced by the microstructure of the IDZ and/or SRZ and consequently the substrate. The presence of TCP phases and high concentration of precipitates can slow down the outward diffusion of nickel and therefore limit the extent of swelling [98]. In the case of the material systems presented in this work, the increased elemental segregation observed in the CM186LC's IDZ is expected to result in slower outward diffusion of nickel when compared to the CMSX-3 system. This explains the significant platinum enrichment experienced by the coating in the CM186LC system, shown in Figure 42. The coating is being depleted of aluminum and chromium during the oxidation/corrosion process. While at the same, time the outward diffusion of nickel from the substrate to the coating is slowed down, leaving behind a platinum-rich coating. The CMSX-3 system, on the other hand, shows a coating that is nickel-rich, which is consistent with uninhibited outward diffusion of nickel taking place during the exposure.

While the general notion of swelling in diffusion coatings can be explained by the outward diffusion of nickel from the substrate to the coating, and the differences in swelling extent between the two systems can be explained by the microstructure of the IDZs, more work needs to be done in order to fully understand the variations in coating thickness along the circumference of the sample. The observed non-uniformity of the coating thickness, or "preferential swelling" attributed to non-uniform hot corrosion attack due to differences in effective gas velocity is not fully understood. Therefore, detailed understanding of the mechanisms behind the particular phenomena requires further studies.

The statistical analysis of the corrosion profile concluded that the two material systems experienced different extents of attack, with the CM186LC system experiencing more advanced attack. This notion is supported by the data on the compositional evolution of the coating shown in Figure 42 along with microstructural analysis of the coating and is in agreement with what has been reported in the literature [53]. The microstructural analysis of the two different material systems revealed that although the martensite and the γ' phase, both of which are evidence of coating degradation, are present on both material systems they are more prominent in the CM186LC system. The increased presence of these two phases can be explained by the differences in their compositions. Figure 48a shows a phase diagram for the Ni-Al-Pt system at 1100 °C where the pre- and post- exposure coating compositions for both systems have been mapped [99].

The slowed nickel diffusion taking place in the CM186LC system causes the composition of the coating to move towards a lower aluminum and higher platinum direction, moving towards the phase boundary and into the β-γ' domain. The CMSX-3 system on the other hand, moves almost exclusively along a path where platinum content is constant. This takes the coating composition towards the edge of β phase boundary. Being so close to the boundary, it is expected to observe the transformation to γ' where local composition variations can result in further nickel enrichment due to substrate interdiffusion and/or consumption due to oxidation. The few observations of γ' in the CMSX-3 are consistent with the expected small variations in local chemistry. Although the data presented corresponds to lower temperature exposures, Figure 48b [100] shows that at lower temperature the above observations still apply.

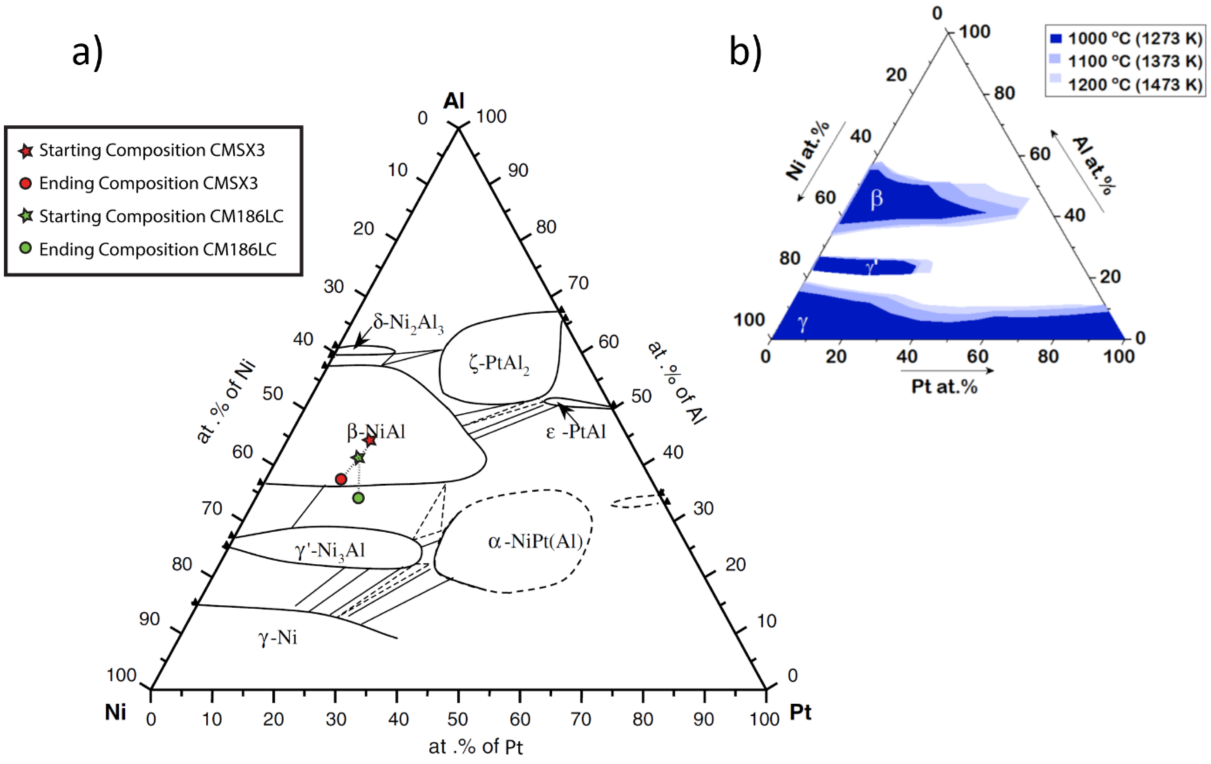

FIGURE 48. a) Ternary phase diagram for Ni-Al-Pt at 1100 °C system with the starting and ending compositions of the Pt-modified aluminide coatings deposited on CMSX-3 and CM186LC [99], and b) solid solubility limits in the γ, γ' and β phases as a function of temperature [100].

5.5 Conclusions

The hot corrosion resistance of five substrate-coating material systems comprised of commercially available nickel-based superalloys and diffusion coatings was evaluated. The best performing systems were the platinum aluminide diffusion coatings on two different nickel-based superalloys. Further analysis of these two systems revealed that the different compositions and microstructures of the substrates strongly influenced the overall coating performance when evaluated under type I hot corrosion conditions in a burner rig testing facility.

It was shown that a statistical approach focused on the parametrization and analysis of corrosion profiles can facilitate the matching of physical properties to statistical parameters and therefore improve our understanding of hot corrosion. Based on the data collected through this approach, and supported by phase and elemental analysis, it was proposed that the pin shaped samples with Pt-modified aluminide coatings initially experience swelling that is uniform along the length of the pin, and around the circumference of the pin. The swelling can be explained by the outward diffusion of nickel during the initial stages of exposure. After the initial swelling stage ends, the corrosion-consumption stage begins where the coating material experiences material loss due to corrosion. This corrosion-consumption stage is non-uniform along the length of the pin, with the top experiencing a more exacerbated process, as well as around the circumference of the pin. The height dependency of the corrosion-consumption is attributed to uneven distribution of the salt contaminant in the gas flow, while the non-uniformity around the circumference is attributed to differences in the effective gas flow velocity. Further work is needed to fully understand the relationship between effective gas flow velocity and the enhanced hot corrosion attack observed.

Of the two materials systems evaluated, the system with CM186LC, a DS superalloy, as a substrate experienced exacerbated attack when compared to the system with CMSX-3, a single crystal superalloy, as the substrate. This was attributed to the segregation of refractory elements and formation of TCP phases in the IDZ of the CM186LC system, which hindered the outward diffusion of nickel. Slow nickel diffusion combined with aluminum depletion resulted in a platinum-rich coating more susceptible to phase degradation evidenced by the higher presence of both γ’ and martensite phases.

CHAPTER 6: A Low-Velocity Burner Rig Study of the Type I Hot Corrosion Resistance of Overlay Coatings

6.1 Introduction

Nickel-based superalloys are currently used for most components in the hot sections of turbine engines [40]. Their mechanical properties at high temperature makes them excellent candidates to fulfill this role. However, they are still susceptible to chemical and environmental attacks [50]. Therefore, specialized protective coatings have been put in place to provide a barrier between the substrate and the harsh environment around it. Protective coatings, their composition, microstructure, and deposition methods are an important area of research that continues to grow with every technological advance [51].

In order to perform their jobs as protective coatings, the coating materials must be tailored to the specific environment they aim to protect. Therefore, different coatings are developed for use in the many different types of turbines, such as power generation, aero, and marine turbines. In the case of marine turbines, the coatings must withstand corrosive environments created by the presence of salts in the intake air and/or fuel contaminants such as sulfur. High temperatures and the presence of salt contaminants prompt an accelerated oxidation attack known as hot corrosion, where molten salts cause dissolution of the protective oxide layer leading to the eventual penetration and sulfidation-oxidation of the substrate that leads to failure of the part [12, 25].

The most commonly used coatings in marine turbines are what are known as diffusion coatings and have been discussed in the previous chapter. The second type of coatings provide enhanced hot corrosion resistance, as well as flexibility for compositional variation, and are known as overlay coatings or MCrAlY coatings [63]. In this case M stands for the main element, which in the case of marine turbines, is usually nickel, cobalt or both nickel and cobalt. As indicated by the name, these coatings also contain chromium, aluminum and yttrium, and they often include smaller additions of alloying elements, such as hafnium, silicon, tantalum, etc. [66]. Overlay coatings can be applied through various processes such as: APS, EB-PVD and LPPS [62]. LPPS results in superior microstructure and performance but has a higher cost. Consequently, overlay coatings can be applied to substrates with minimal interaction with them, resulting in a coating whose chemical and mechanical behavior are thought to be largely independent of the substrate.

The goal of this work is to evaluate coating-substrate compatibility of new candidate coatings on both commercially available substrates as well as potential new substrate superalloys. This work also aims to investigate the effect, if any, that substrates have on the hot corrosion resistance of overlay coatings. With those goals in mind, the type I hot corrosion resistance of 14 different substrate-coating systems optimized for the high temperature section of gas turbines will be evaluated in a low-velocity burner rig test. Among the substrate-coating systems chosen, 4 will be comprised of both a new substrate superalloy as well as a new coating, while the remaining 10 systems will be comprised of new coatings on commercially available substrates. Through this matrix of materials, coating performance will be evaluated in order to select the best performing coatings. Coating-substrate compatibility of new substrates will be assessed by comparison with that of commercially available substrates.

6.2 Experimental Methods

The details of the substrate-coating systems are summarized in Table 13. The substrate compositions are provided in Table 14. The exact composition is given for commercially available substrates, while only a maximum allowed is provided for new substrate materials due to proprietary restrictions. The exact coating compositions or names are not provided due to proprietary restrictions.

TABLE 13. Summary of overlay-based, substrate-coating materials-system tested.

Coatings	NiCrAlY-mod	NiCrAlY-mod+Al	CoCrAlY+Al	CoCrAlY-Pt	CoCrAlY	NiCoCrAlY-mod
Substrates	IN792Hf	IN792Hf	CMSX4	CMSX-4	Alloy-X	CM939
	MM247	MM247	CM939	CM939		
	Alloy1+Si	Alloy1+HfSi	Alloy-X			
	MM002					

*TABLE 14. Substrate composition in wt. % *For Alloy1 and Alloy-X only maximum wt.% is provided.*

	Ni	Cr	Co	Mo	Al	Ti	Ta	W	Zr	C	B	Hf	Re	Nb
CMSX-3	65.7	8.0	5.0	0.6	5.6	1.0	6.0	8.0	…	…	..	0.1	…	…
CMSX-4	61.7	6.5	9.0	0.6	5.6	1.0	6.5	6.0	…	…	…	0.1	3	
CM939	48.2	22.5	19.0	0.0	1.9	3.7	1.4	2.0	0.1	0.15	0.01	0	0	1
CM186LC	62.6	6.0	9.0	0.5	5.7	0.7	3.0	8.0	0.005	0.07	0.015	1.4	3	…
IN792Hf	60.1	12.3	8.9	1.8	3.4	3.9	4.0	4.4	0.05	0.12	0.014	1		
MM002	60.7	8.0	10.0	…	5.5	1.5	2.6	10.0	0.03	0.15	0.015	1.5	…	…
MM247	59.7	8.4	10.0	0.7	5.5	1.0	3.0	10.0	0.05	0.15	0.015	1.5		
Alloy1	65.0	15.0	12.0	5.0	6.0	6.0	7.0	5.0	0	0	0	0	0	0
Alloy-X	60.0	25.0	25.0	0.0	4.0	5.0	4.0	4.0	0	0	0	0	0	1

The sample geometry and sample preparation are detailed in Chapter 2. All samples were evaluated in a low-velocity burner rig at 900 °C for 1000 hours with the experimental parameters detailed in Chapter 2. After exposure, samples were prepared following the procedures detailed in Chapter 2, and corrosion profiles were extracted and analyzed using the protocol described in Chapter 3.

6.3 Results and Discussion

Fourteen different materials systems with overlay coatings were investigated. Their performance was evaluated both quantitatively and qualitatively. Quantitative analysis was achieved through direct measurements of coating material loss, expressed as a fraction of the original coating thickness. Qualitative analysis was done through cross-sectional analysis of exposed samples where phase and elemental analyses were performed.

6.3.1 Material Loss

The performance of all materials tested is summarized in Table 15. The different materials systems are ranked by the percent of coating lost to the hot corrosion attack.

In contrast to the diffusion coatings studied in the previous chapter, the overlay coatings studied here exhibited mostly uniform hot corrosion attack that lead to a net material loss, with no coating swelling taking place. This is consistent with the application process of overlay coatings not relying on substrate diffusion and a composition that is closer to that of the substrate. Figure 49a shows an example of a corrosion profile for the best performing system, CoCrAlY-Pt on CMSX-4, and Figure 49b shows and example of a corrosion profile for the worst performing coating, NiCrAlY-mod on IN792Hf.

TABLE 15. Material loss and performance summary of all overlay coatings tested.

Substrate	Coating	Starting Radius (µm)	Coating Thickness (µm)	Avg Depth (µm)	Avg Depth St Dev (µm)	Max Depth (µm)	Good Coating Remaining (µm)	% Coating Lost
CMSX4	**CoCrAlY/Pt**	1803.48	215.98	9.34	2.7	72.69	206.64	4.32
IN792Hf	**NiCrAlY-mod+Al**	1823.98	236.48	11.15	2.6	83.60	225.33	4.72
MM247	**NiCrAlY-mod+Al**	1827.48	239.98	12.76	2.1	61.01	227.22	5.32
CM939	**NiCoCrAlY-mod**	1755.27	167.77	10.33	7.9	87.18	157.44	6.16
CM939	**CoCrAlY/Pt**	1798.15	210.65	15.89	9.2	67.90	194.76	7.54
Alloy-X	**CoCrAlY**	1729.28	141.78	13.39	1.6	90.89	128.40	9.44
CMSX4	**CoCrAlY+Al**	1804.83	217.33	21.22	1.0	79.67	196.11	9.76
CM939	**CoCrAlY+Al**	1809.30	221.80	24.39	11.8	91.19	197.41	10.99
Alloy-X	**CoCrAlY+Al**	1805.27	217.77	26.56	16.8	118.64	191.20	12.20
MM002	**NiCrAlY-mod**	1797.60	210.10	27.44	1.7	105.96	182.66	13.06
Alloy1+HfSi	**NiCrAlY-mod+Al**	1827.35	239.85	31.36	1.0	89.58	208.49	13.07
Alloy1+Si	**NiCrAlY-mod**	1792.18	204.68	26.94	8.0	92.62	177.73	13.16
MM247	**NiCrAlY-mod**	1828.75	241.25	41.39	0.9	90.66	199.86	17.16
IN792Hf	**NiCrAlY-mod**	1819.67	232.17	40.93	1.7	88.24	191.23	17.63

6.3.2 Coating Case Studies

Because overlay coatings are applied on the surface of substrates using spraying processes rather than developed through diffusion processes, the historical consensus has been that substrates have little effect on the coating's performance [51]. The large pool of materials evaluated in this work included different substrates with the same coating exhibiting different hot corrosion resistance motivating additional analysis of specific coating systems. Therefore, three coatings have been selected as case studies for further analysis. All three of these coatings were applied on multiple substrates that led to different performances in at least one of the substrates, and two of the three selected coatings were the top performing coatings. The CoCrAlY-Pt system was selected because it was the best performing coating when applied to CMSX-4 but experienced a decrease in performance when applied to CM939. The NiCrAlY-mod+Al coating was the second and third best performing coating when applied to commercially available substrates IN792Hf and MM247. However, its performance decreased when applied to the new candidate substrate material Alloy1+HfSi. Lastly, the NiCrAlY-mod coating was also selected as a case study despite its lower rank for two reasons: a) the best performing coating is a modification of this coating, therefore understanding its hot corrosion resistance will help further understand the behavior of the better performing NiCrAlY-mod+Al, and b) the performance of the coating varied significantly among the different substrates.

Appendix B contains examples of reconstructed images and plots of corresponding corrosion profiles for the coating/substrate systems not included in the case studies below.

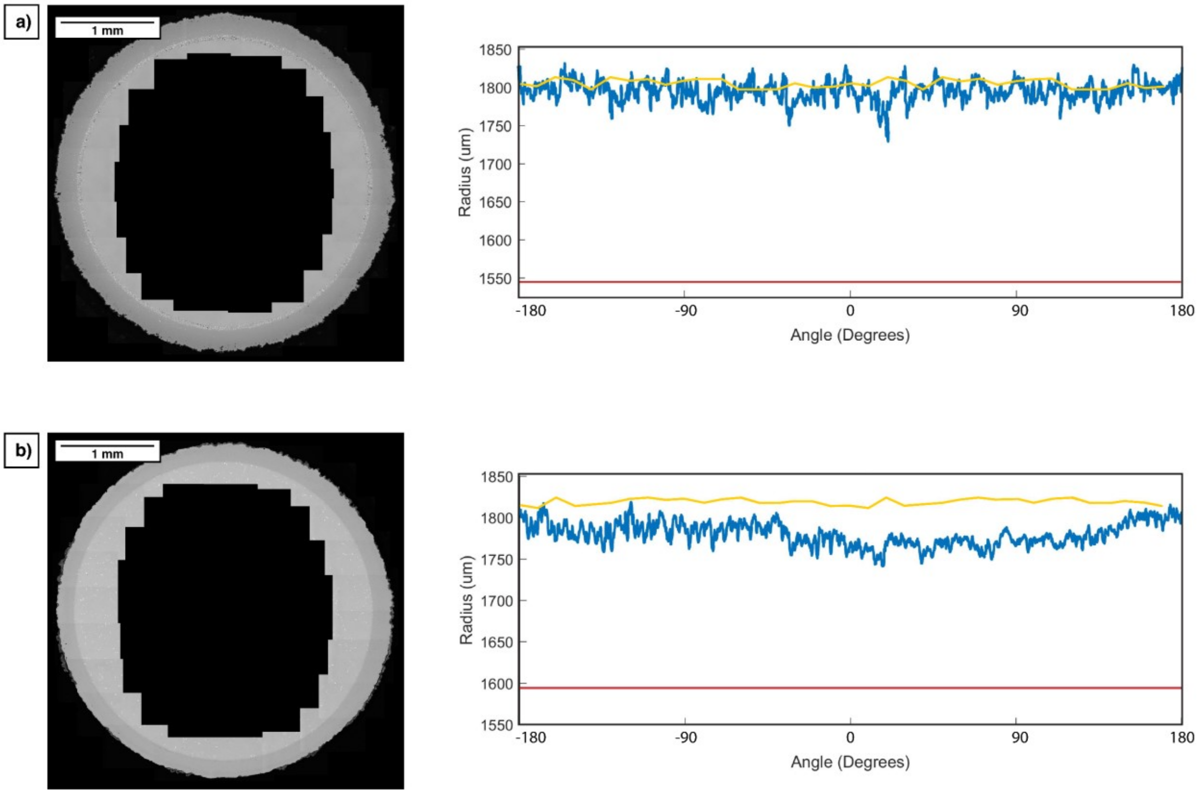

FIGURE 49. Examples of reconstructed images and plot of corresponding corrosion profile for a) the best performing overlay coating, CoCrAlY-Pt on CMSX-4, and b) worst performing overlay coating, NiCrAlY-mod on IN792Hf. Extracted corrosion profile shown in blue, sample radius pre-exposure shown in yellow, and substrate/coating interface shown in red.

6.3.2.1 NiCrAlY-mod

The same NiCrAlY-mod overlay coating was applied to four different substrates, one single crystal and three directionally solidified substrates. Three of the substrates used are commercially available superalloys (IN792Hf, MM247, and MM002), while the fourth substrate is a new candidate substrate material discussed in Chapter 4 (Alloy1+Si). The microstructure of all four coating/substrate systems is shown in Figure 50. The four materials were processed in two different batches, and although the same commercial process was used, each batch resulted in a slightly different microstructure. Alloy1+Si and MM002 were applied the coating in batch A, while IN792Hf and MM247 were applied the coating in batch B. Although the average coating composition remained the same, the overall microstructure changed. The coating produced in batch A has a much finer grain size structure as well as a more uniform distribution of all alloying elements evidenced by the decreased presence of the yttrium rich precipitates observed in the coating processed in batch B. The different microstructures obtained in the two processing batches are shown in Figure 51. Furthermore, substrates containing carbides of refractive elements saw more segregation of these elements at the coating/substrate boundary, as seen in Figure 50.

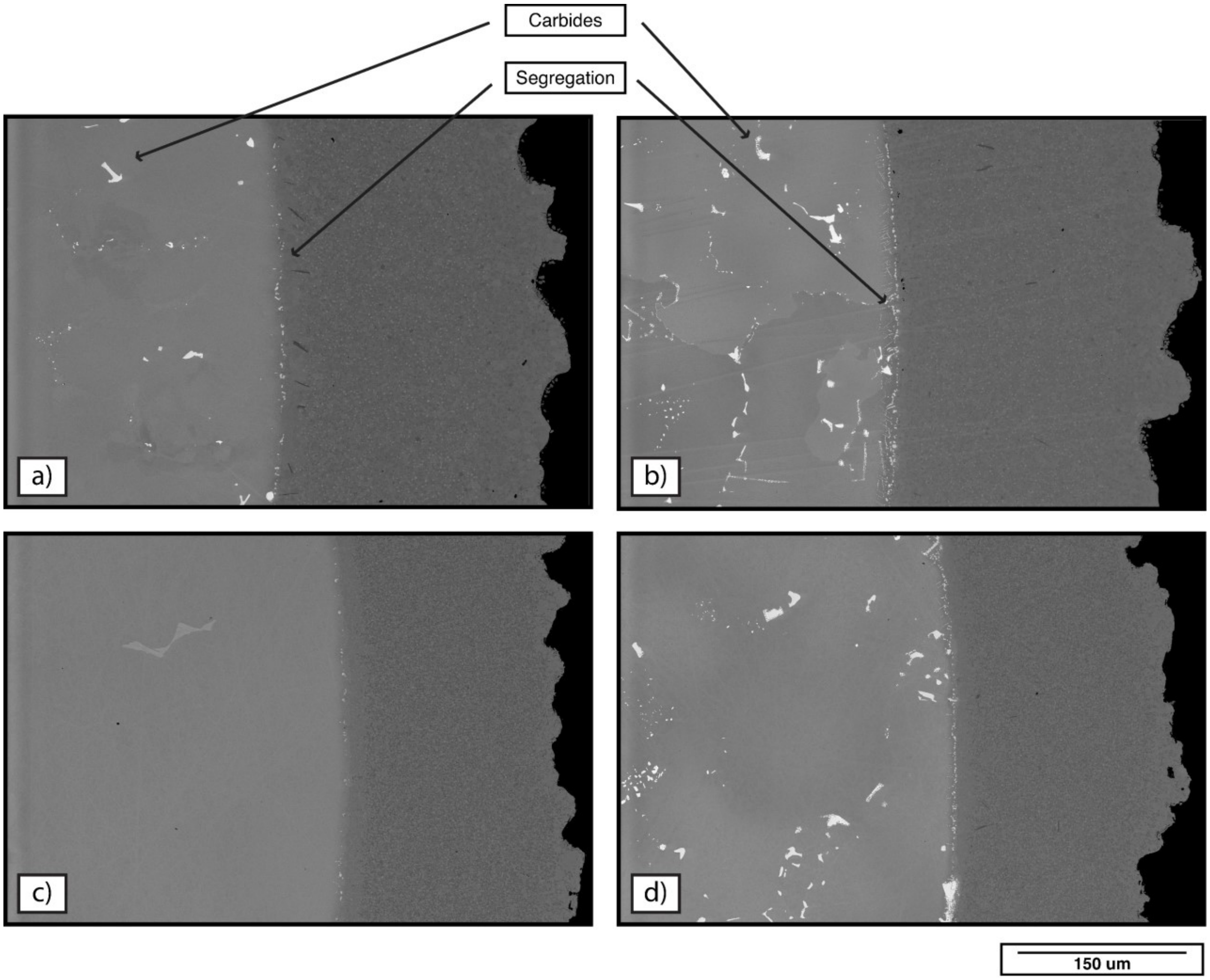

FIGURE 50. Backscattered SEM images of cross-sections showing the initial microstructure of the NiCrAlY-mod coating on a) IN792Hf, b) MM247, c) Alloy1+Si, and d) MM002.

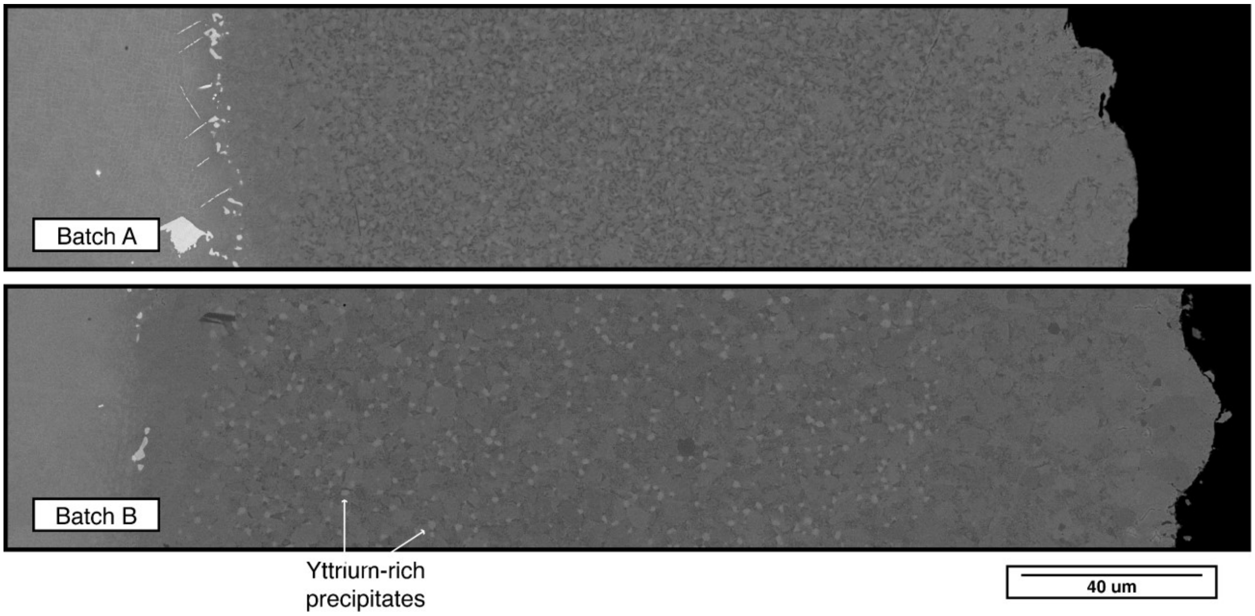

FIGURE 51. Microstructure of the NiCrAlY-mod coating obtained through two different processing batches. Batch A shows finer structure with more uniform distribution of yttrium, while Batch B shows coarser structure with the presence of yttrium rich precipitates.

After exposure the fine grain microstructure of batch A has coarsened, and the overall microstructure of the two batches share several similarities as shown in Figure 52. However, there were small changes that shed light to the potential attack mechanisms behind the differences in performance among these four systems. The most notable one is the presence of yttrium and nickel rich sulfides near the oxide-coating interface in the coatings from batch B (IN792Hf and MM247), which exhibited the worst hot corrosion resistance. These sulfide pockets can be seen in Figure 53.

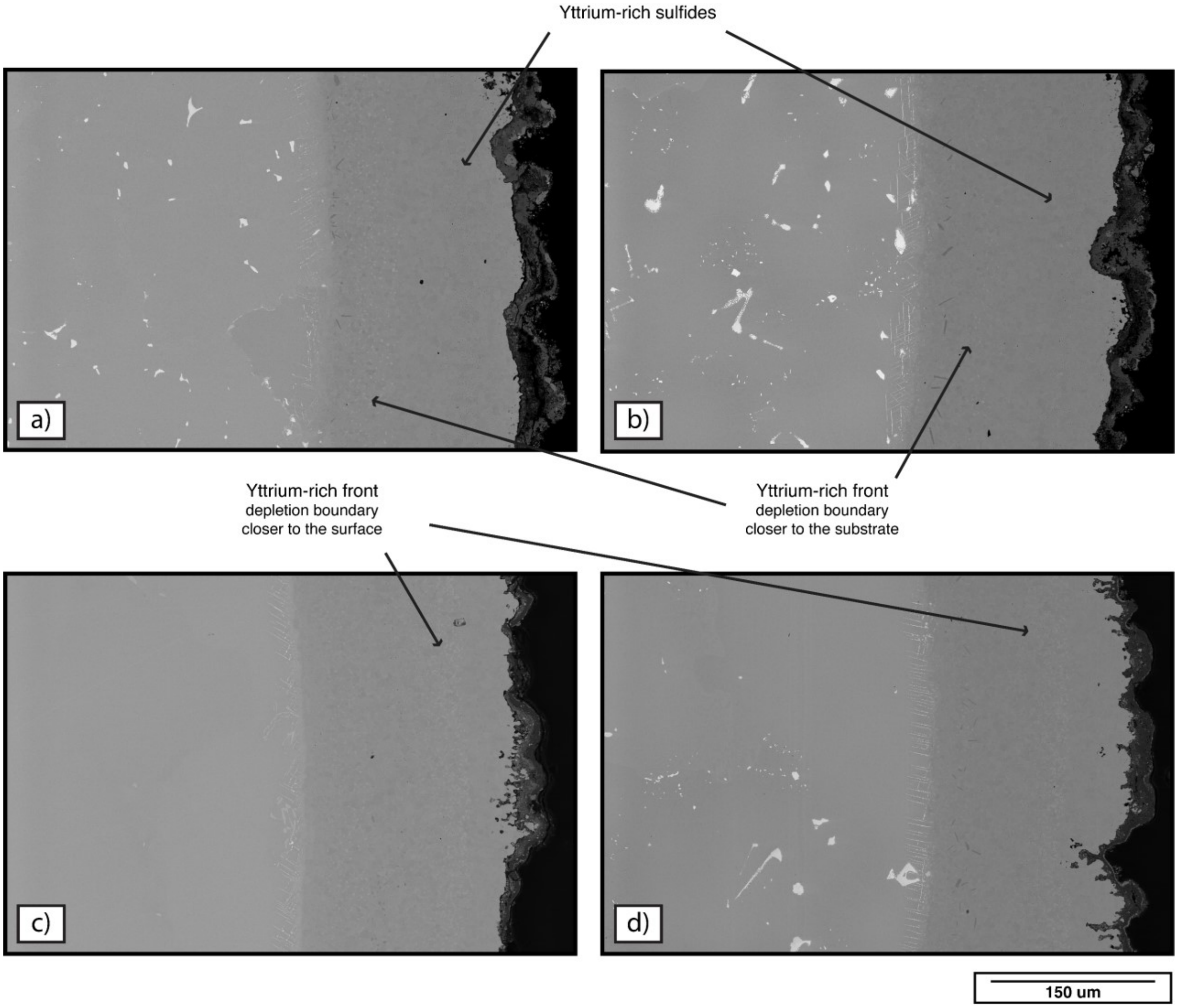

FIGURE 52. Backscattered SEM images of cross-sections showing the post-exposure microstructure of the NiCrAlY-mod coating on a) IN792Hf, b) MM247, c) Alloy1+Si, and d) MM002.

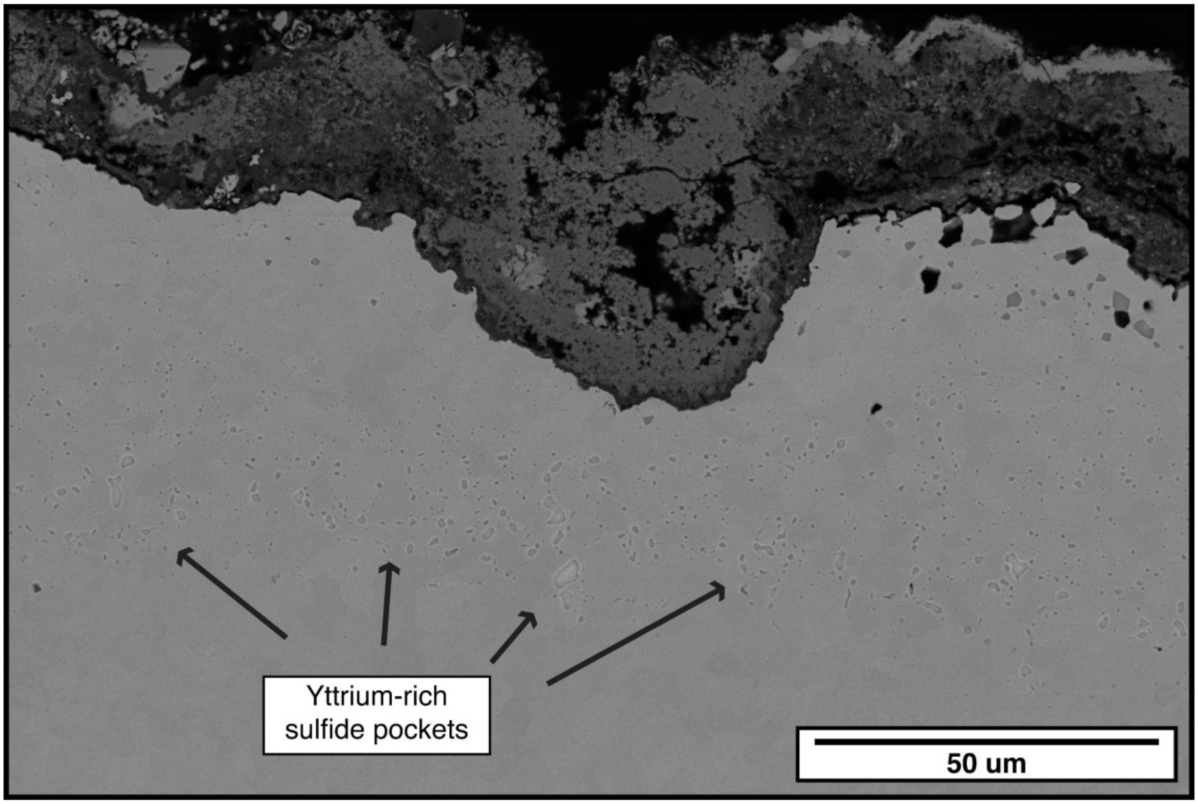

FIGURE 53.Backscattered SEM images of a cross-section showing the presence of yttrium-rich sulfides in the post-exposure microstructure of the NiCrAlY-mod coating on MM247.

The presence of sulfur rich pockets not only supports the quantitative data discussed above, but it provides an explanation for the difference in material loss. The two material systems that had the higher coating loss percentage also have higher content of sulfur within the coating. This is evidence of higher internal diffusion of sulfur and therefore, a less effective coating.

The average coating composition pre- and post- exposure were measured through EDS and the difference between the two is shown in Figure 54a. Although all four material systems experienced the same trends with increased nickel content and decreased chromium and aluminum content, the amount by which these elements changed are different. In the two best performing materials, the coatings from batch A (Alloy1+Si and MM002), with only 13%

coating loss, changes in composition remained under 5% wt. On the other hand, the two systems that experienced a higher percentage of coating loss (17%) also experienced a more drastic change in coating composition, loosing over 10% chromium and increasing the nickel content by a similar amount. The change in aluminum remains small and constant among all four systems.

The average composition of the oxide formed was also evaluated and is shown in Figure 54b. Similarly, certain trends can be observed among the materials with similar performances. The two best performing materials incorporate higher amounts of aluminum into the oxide formed, while keeping the nickel content at a minimum. Their counterparts on the other hand had lower levels of aluminum and higher levels of chromium and nickel. This can be attributed to the oxidation-consumption process that takes place in the more advanced stages of hot corrosion attack. In this case, aluminum oxide has been consumed by the hot corrosion attack leaving behind a more chromium and nickel rich oxide and a more depleted coating.

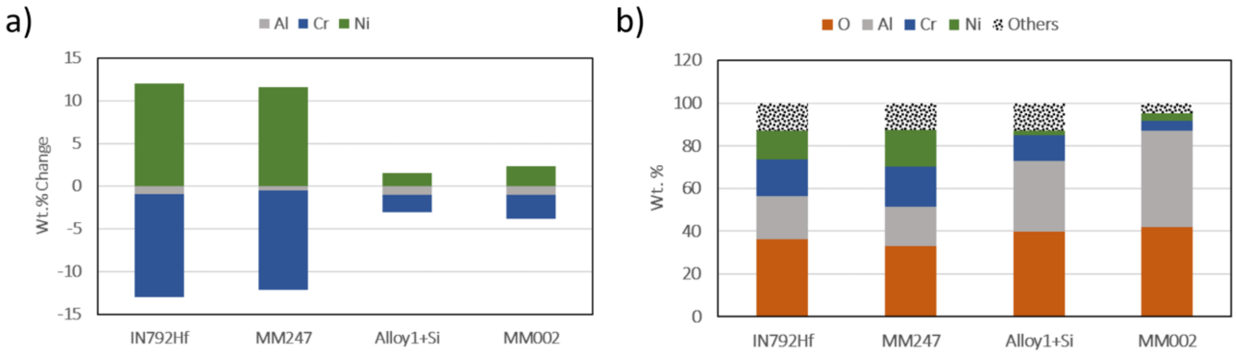

FIGURE 54. Plots of a) the difference between pre- and post-exposure compositions of the NiCrAlY-mod coatings, and b) The composition of the oxide formed on the surface of the NiCrAlY-mod coatings.

The new candidate substrate material exhibited coating compatibility comparable to that of the commercially available substrates. This is evidenced by the similarities in the interdiffusion zones. The new substrate did not experience increased formation of detrimental phases or disproportionate elemental segregation along the boundary.

A detail worth noticing is the location of the yttrium rich front in all systems. In the case of MM002 and Alloy1+Si, it is located much closer to the oxide/coating interface. While in the case of MM247 and IN792Hf, it is further away from the oxide, and closer to the coating/substrate interface, as shown in Figure 52. This yttrium rich front marks the boundary between the depleted area of the coating, where the composition and microstructure have deviated from the original due to the depletion of certain elements to form the protective oxide, and the remaining intact coating. The different depletion depths match the compositional data discussed previously, where MM002 and Alloy1+Si have both a smaller depletion depth as well as a smaller change in overall coating composition. MM247 and IN792Hf, on the other hand, experience a deeper depletion depth accompanied by a larger change in overall coating composition. The MM247 and IN792Hf systems experience an accelerated attack due mainly to the increase in inward sulfur diffusion caused by the formation of a less protective oxide layer.

6.3.2.2 NiCrAlY-mod+Al

The next coating of interest is a modification of the previously discussed NiCrAlY-mod coating. In this case, an aluminizing step is applied to the surface of the NiCrAlY-mod creating a multilayer system. The initial microstructures of the three different material systems incorporating the NiCrAlY-mod +Al coating are shown in Figure 55. In this case, the substrates investigated include three of the four analyzed in the NiCrAlY-mod case, Alloy1+HfSi, IN792Hf and MM247. However, in this case, it is Alloy1 with both dopants that is being analyzed instead of the silicon doped only. Although the coating application is a two-step process, the resulting microstructure is a three-layer one. As previously mentioned, the application of the overlay coating is through low-pressure plasma spraying, which does not rely on interactions with the substrate. The aluminum enrichment of the surface, on the other hand, is done through a proprietary process that relies on the internal diffusion of aluminum, and therefore substrate interactions are critical. Consequently, the resulting microstructure of the as processed materials exhibits three different layers: the outermost is the aluminizing step, the middle layer is the area where interdiffusion between the aluminizing and the NiCrAlY-mod coating has taken place, and the innermost layer is the area of the coating that did not experience significant changes due to the aluminizing interdiffusion. Due to the importance of diffusion in the coating processing, minor differences in the initial microstructure of the coatings can be observed. The coating applied to IN792Hf and MM247 share the same microstructure but differ from that of the coating applied to Alloy1+HfSi. The coating applied to the DS superalloys has a much smoother surfaces that, although exhibiting sinusoidal behavior, lacks the hard edges present in the Alloy1+HfSi coating. Furthermore, the outermost aluminum enriched layer is thinner and more aluminum rich in the DS alloys while thicker and more spread out in the single crystal. The coating applied to Alloy1+HfSi also exhibits higher degree of yttrium segregation evidenced by the increased presence of yttrium rich precipitates, as seen in Figure 55d.

It is also worth pointing out that, unlike the previous case, the starting NiCrAlY-mod microstructure is consistent across all three systems and corresponds to the finer structure seen in batch A of the NiCrAlY-mod coatings. Therefore, the differences observed among these three systems arise from the final aluminizing step, and not from the spraying step of the coating application process.

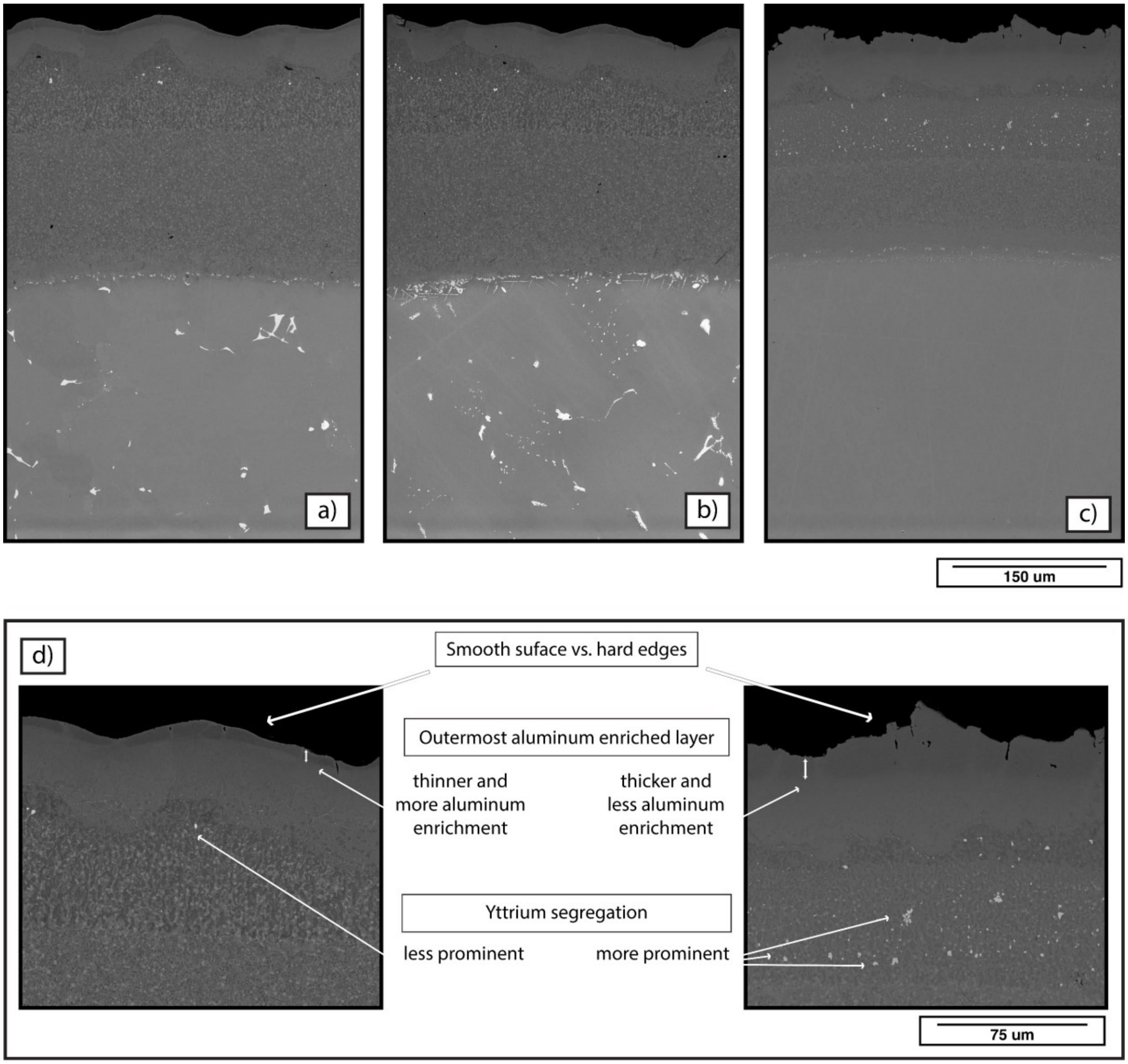

FIGURE 55.Backscattered SEM images of cross-sections showing the initial microstructure of the NiCrAlY-mod+Al coating on a) IN792Hf, b) MM247, and c) Alloy1+HfSi. e) microstructural differences between the NiCrAlY-mod+Al coating applied to Alloy1+HfSi (shown on the right) and the one applied to MM247 (shown on the left) and IN792Hf.

The post-exposure behavior of this NiCrAlY-mod+Al coating on the different substrates is shown in Figure 56. Alloy1+HfSi, the system that differed in microstructure from the other two systems, had the worst performance losing 13% of the original thickness of the coating. The two DS superalloys, on the other hand, only lost around 5% of the original thickness of the coating. The post-exposure microstructure retains the three-layer structure of the as-processed coating. However, the nature of these layers differs slightly. The outermost layer is now the depleted zone, where the coating has lost enough of the oxidized elements to lose its original structure. The innermost layer has now been affected by the interdiffusion with the substrate that has taken place during the long-term, high temperature exposure. Therefore, the middle layer is the area that retains the most resemblance to the original coating microstructure, experiencing the least effect from the oxidation-driven depletion and the substrate interdiffusion. Therefore, the thickness of this middle layer provides a measurement of the coating's lifetime. In the case of the Alloy1+HfSi coating, it is clear from Figure 56c) that the coating has experienced significant depletion and has a much shorter lifetime than the other two coatings.

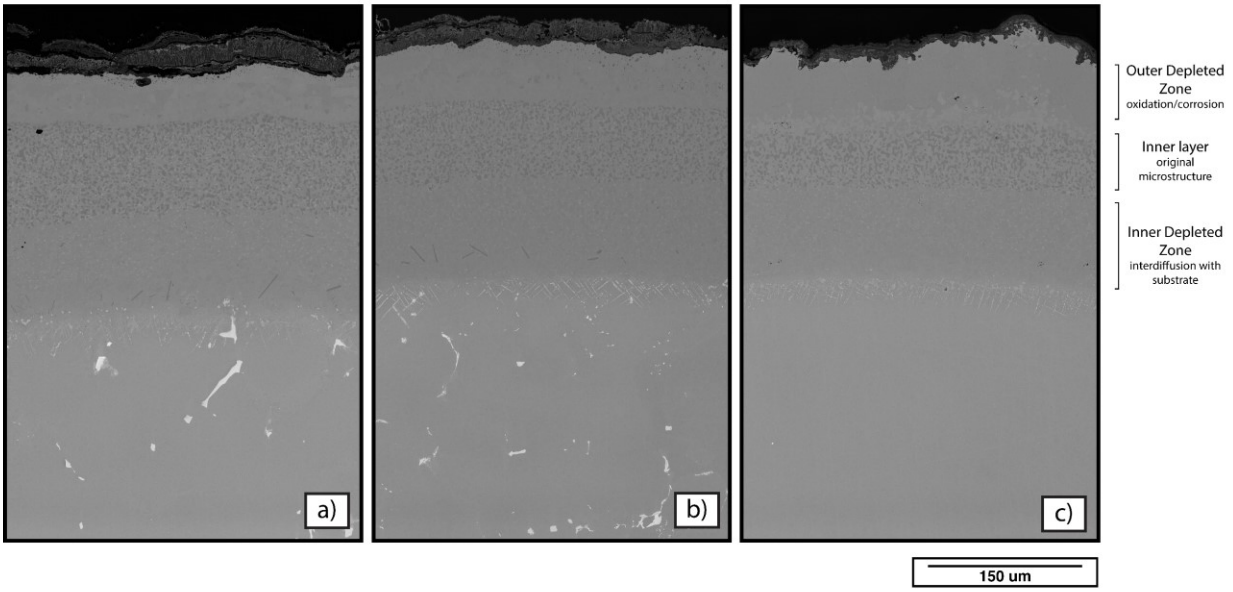

FIGURE 56.Backscattered SEM images of cross-sections showing the post-exposure microstructure of the NiCrAlY-mod+Al coating on a) IN792Hf, b) MM247, and c) Alloy1+HfSi.

The analysis of the change in coating composition revealed no clear trends differentiating the different levels of coating loss, shown in Figure 57a. The two best performing systems (MM247 and IN792Hf) lie on opposite ends of the compositional change spectrum with Alloy1+HfSi being right in the middle. Therefore, no insight was gained from the depletion trends in the coatings. However, analysis of the oxide layer did reveal important differences among these groups. Compositional contrast obtained through backscattered imaging reveals that the oxide formed on the better performing systems has a very particular structure. The oxide layer formed has a layered structure, where the layers lie perpendicular to the coating surface and alternate from an aluminum oxide rich in nickel, to an aluminum oxide low in nickel content. Figure 58 shows the layered structure of the oxide formed on the MM247 system, where the bright layers along the oxide represent the nickel rich oxide. The different oxide morphology is also manifested in the difference in oxide composition shown in Figure 57b. The graph shows that the coatings applied to MM247 and IN792Hf incorporate more than 20 wt.% of nickel into the oxide layer, while the coating applied to Alloy1+HfSi only incorporated a tenth of that.

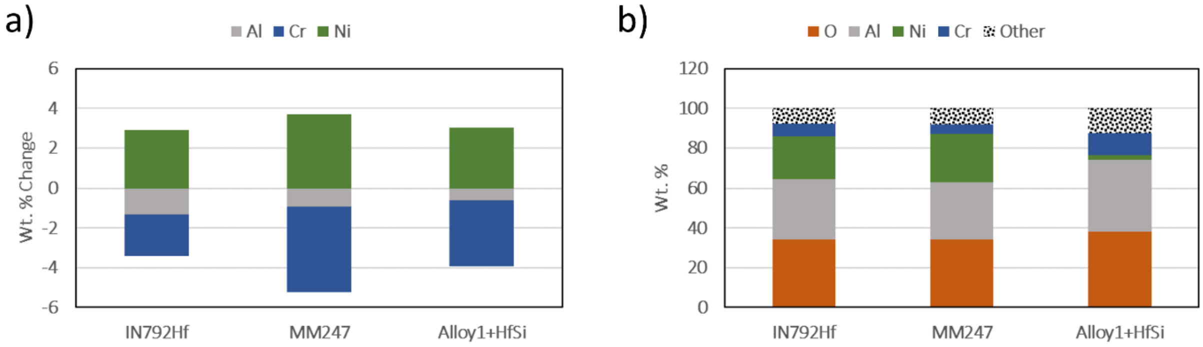

FIGURE 57. Plots of a) the difference between pre- and post-exposure compositions of the NiCrAlY-mod+Al coatings, and b) The composition of the oxides formed on the surface of the NiCrAlY-mod+Al coatings.

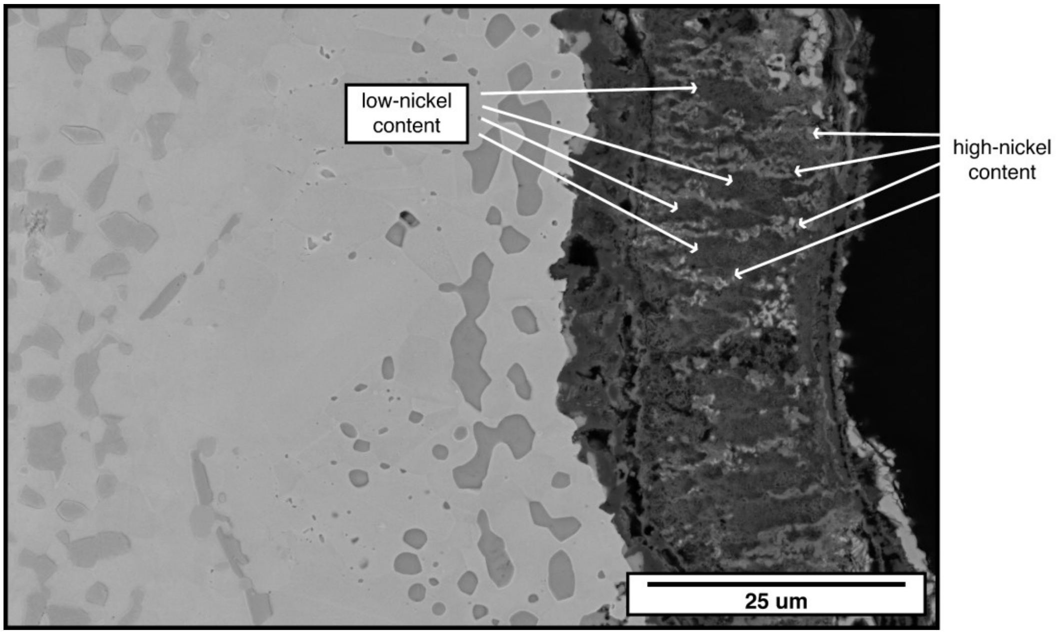

FIGURE 58. Backscattered SEM image of a cross-section showing the layered structured of the oxide formed on the NiCrAlY-mod+Al on MM247.

Therefore, the mechanism behind the difference in hot corrosion performance for the aluminum modified NiCrAlY-mod coating is the formation of a more protective oxide with a distinct layered structure. Alloy1+HfSi fails to form such an oxide and therefore experiences an exacerbated attack. It is no surprise that this substrate-coating system formed an oxide with different microstructure and composition given that its as-processed microstructure differed from the other two. The exact same aluminizing step applied to these three different systems resulted in two different coating microstructures and therefore different coating performance. It is proposed that the difference in substrate composition sets up chemical potentials that develop into different diffusion patterns. The specific source of microstructural differences has yet to be identified and its complete understanding will require a methodical study of the aluminizing parameters.

6.3.2.3 CoCrAlY-Pt

In the case of the platinum-modified CoCrAlY coating, two different substrates were studied: CMSX-4, a single crystal, and CM939 a directionally solidified superalloy. The two substrates of interest differ not only in their microstructure, but also differ greatly in their composition, shown in Table 14.

The initial microstructure of the two overlay coatings was quite different, as seen in Figure 59. The coating deposited on CMSX-4 shows a large fraction of porosity present all throughout the thickness of the coating. While there is virtually no porosity present on the coating deposited on CM939. Differences in porosity could arise from small changes in spraying parameters or different heat treatment temperatures and/or times. The samples provided were sprayed by the same manufacturer with the same commercial process, and the source of this difference is still being investigated and will require a methodical study of spraying and heat treatment parameters.

Quantitative analysis of the post-exposure samples shows that the single crystal CMSX-4 outperformed the DS CM939, with percent coating losses of 4% and 8% respectively. A cross-section view of the coatings revealed subtle differences in microstructures, Figure 60. The depletion zones and the bulk of the coating show no major differences, given that the initial porosity seen in the CMSX-4 coating, differentiating the two systems, is no longer present. The IDZ on the other hand looks very different for these two systems. This is to be expected, given that the different composition substrates setup different chemical potentials for each element and therefore, different diffusion patterns. The IDZ in the CMSX-4 is much more compact and with a higher content of not only refractory elements but also platinum segregation.

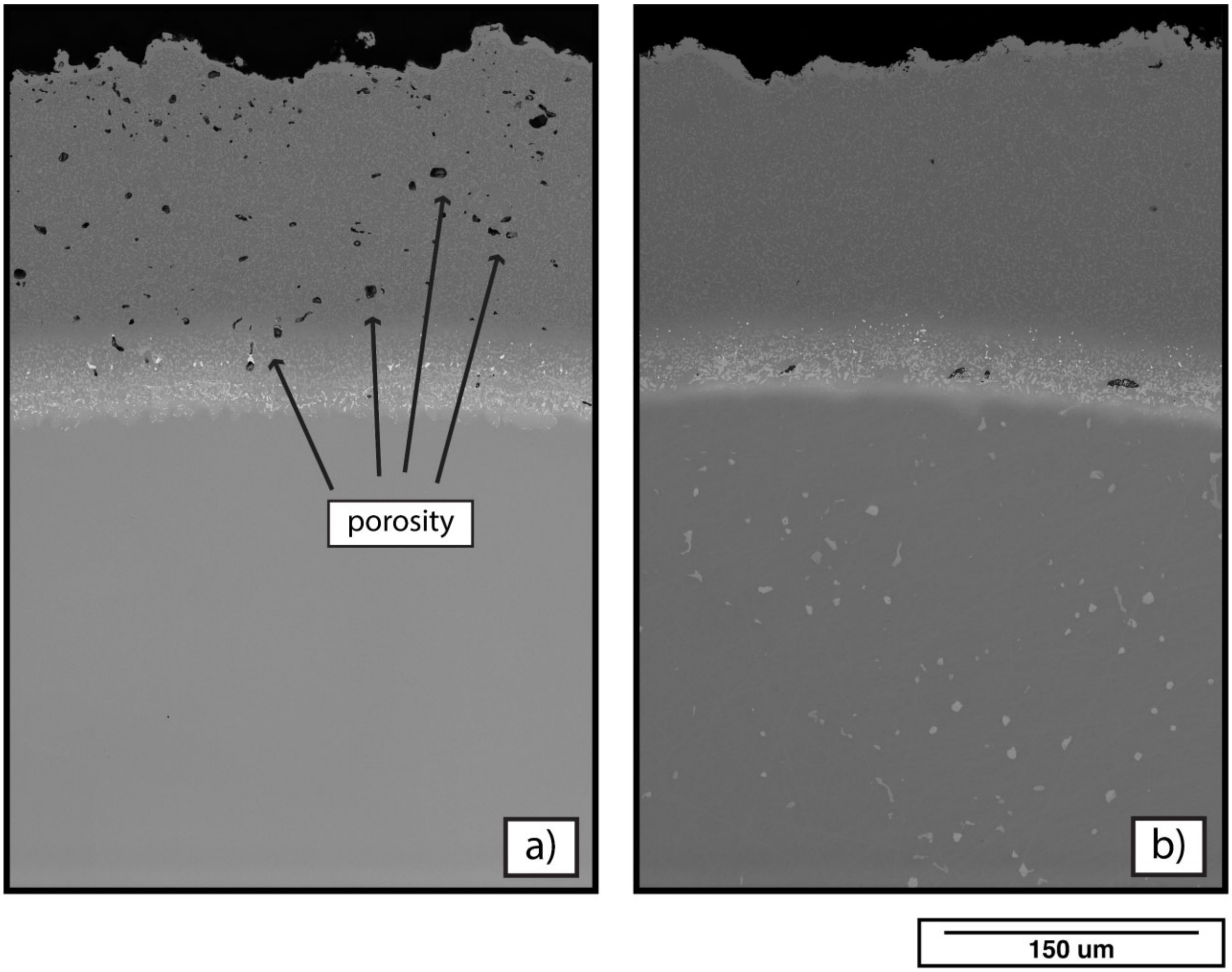

FIGURE 59. Backscattered SEM images of cross-sections showing the initial microstructure of the CoCrAlYPt coatings on a) CMSX-4, b) CM939.

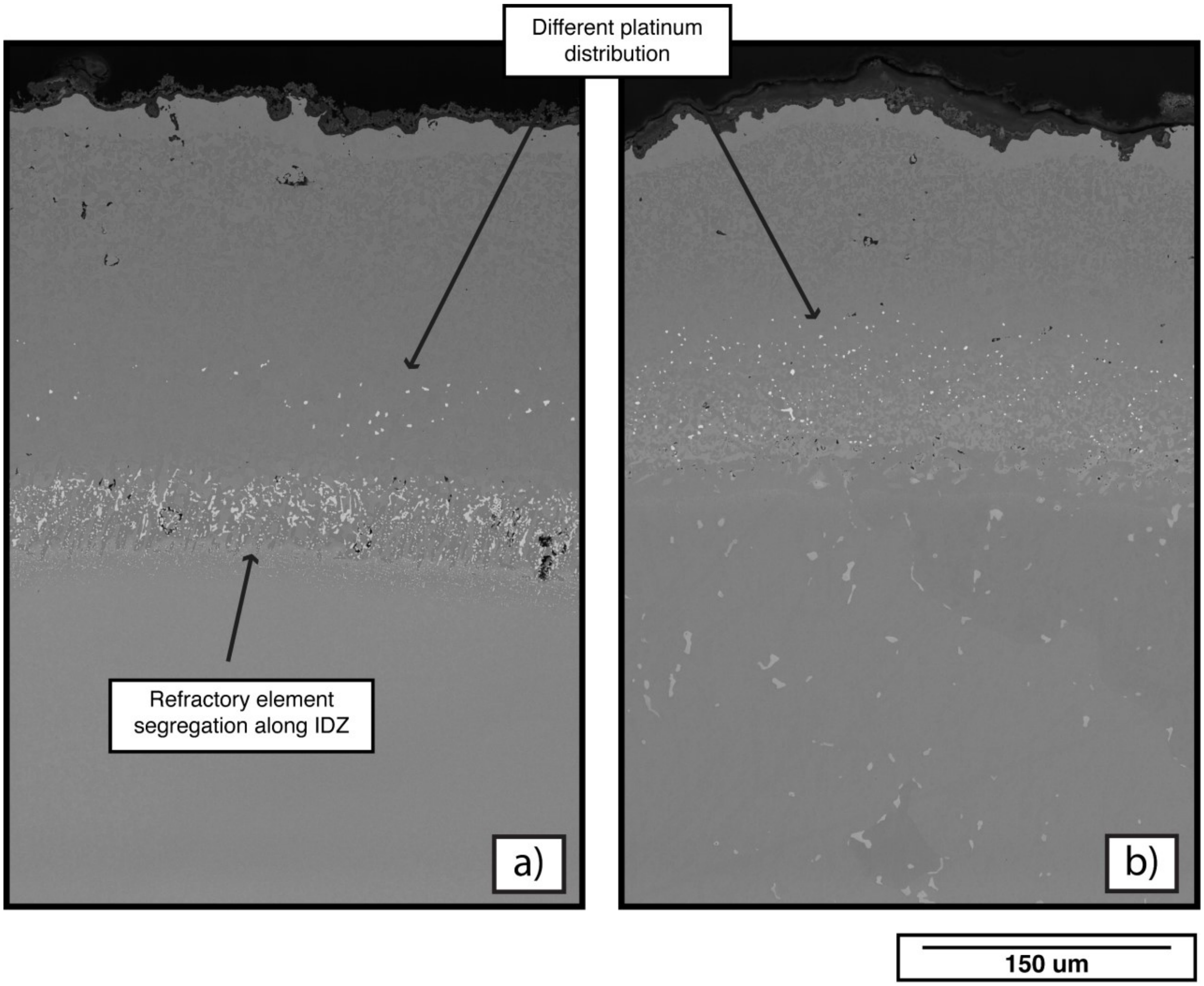

FIGURE 60. Backscattered SEM images of cross-sections showing the post-exposure microstructure of the CoCrAlYPt coatings on a) CMSX-4, b) CM939.

The compositional analysis of the pre- and post- exposure coatings summarized in Figure 61a shows that the same coating on two different substrates undergoes a very different compositional evolution during the LVBR exposure. Although both coatings were depleted in aluminum, chromium and cobalt, the degree of depletion differed with CMSX-4 experiencing higher depletion levels. Furthermore, the resulting coating in CMSX-4 was very rich in nickel with small amounts of tantalum and platinum. On the other hand, the coating on CM186LC did not include any tantalum, and although nickel-rich, it had a higher amount of platinum than that found in the CMSX-4 coating. Depletion pattern differences did not have a major effect on the composition of the oxide formed as only small differences in the chromium and cobalt content were observed as well as in some other minor elements such as salt constituents and yttrium. This comparison is summarized in Figure 61b.

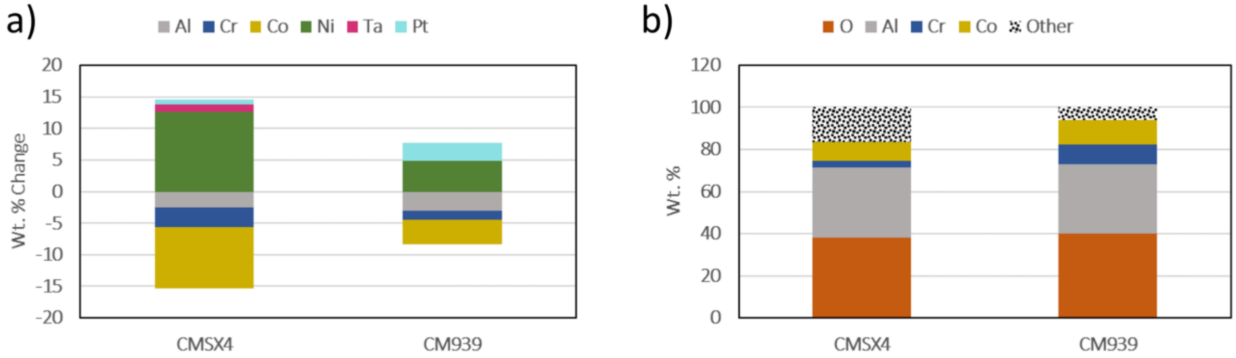

FIGURE 61. Plots of a) the difference between pre- and post-exposure compositions of the CoCrAlY-Pt coatings, and b) The composition of the oxides formed on the surface of the CoCrAlY-Pt coatings.

While the as-processed coatings differ mainly in the presence of porosity, the post-exposure coatings differ from one another in the size and elemental segregation of the IDZ. Due to the inconsistencies found in the microstructure of the as-processed coatings, it is unclear if the porosity present in the CMSX-4 system played a significant role in the coating's microstructural and elemental evolution and consequently, its performance. Further work is needed to fully understand the source and role of the observed porosity. Nonetheless, the differences in IDZ between the two systems suggest that substrate/coating interdiffusion is a dominant factor defining the different coating performances and microstructure. It is possible for the observed porosity to have exacerbated this effect, and for a porosity-controlled coating to display the same type of hot corrosion resistance when applied to the two substrates studied here. More work focused on the relationship between processing, final coating microstructure, and performance is needed.

6.4 Conclusions

The hot corrosion resistance of fourteen different substrate-coating systems was evaluated under type I hot corrosion conditions in a low-velocity burner rig. A total of six different coatings were evaluated on a total of nine different substrates, four of which were new candidate materials for improved turbine operations. The best performing system was a platinum-modified CoCrAlY coating on the single crystal CMSX-4. This same coating applied to a CM939 experienced a decrease in performance marked by higher material loss. Closer examination of these two systems revealed differences in the as-processed coatings, with the better performing system exhibiting higher porosity throughout the coating. Due to this discrepancy in microstructures, the source of the differing hot corrosion resistances cannot be isolated and solely attributed to the substrates themselves. Therefore, more work is needed to understand both the presence of porosity and the effect, if any, that different substrates have on the performance of this particular coating. Nonetheless, the difference in IDZ microstructure and performance point to different degrees of coating compatibility that ultimately resulted in different degrees of hot corrosion resistance.

A modified NiCrAlY, although not high performing, was selected for further studies due to its similarity to the second-best performing coating, as well as due to the variation in hot corrosion resistance observed across different substrates. Closer examination revealed that even though all four systems were commercially sprayed with the same coating, two different microstructures were obtained. One fine-grained microstructure with smaller degree of elemental segregation, and one coarser microstructure with increased presence of yttrium rich precipitates. The coating with finer microstructure had enhanced hot corrosion resistance while the coarser structured coating experienced higher material loss and increased inward diffusion of sulfur.

The second-best performing coating was an aluminized modification of the NiCrAlY-mod. The coating applied to three different substrates, showed two different microstructures and levels of hot corrosion resistance. The outer or aluminized part of the coating exhibited different microstructures in the as-processed condition which was attributed to the aluminizing step relying on interdiffusion to form the outermost layer of the coating. It was this difference in the outer layer that ultimately determined the different hot corrosion resistance exhibited by the materials. Two of the three systems formed a protective layered oxide that slowed down the attack. When applied to the new candidate material Alloy1+HfSi the oxide lacked the layered structure and was not able to prevent the attack.

In summary, although some differences in the degree of material loss were observed between systems that shared the same coating but differed in substrate, there was enough variation in the as-processed microstructure due to potential processing variances that the substrate/coating interaction could not be isolated as the unique source of the different degrees of hot corrosion observed. Furthermore, no significant differences in coating-substrate compatibility were observed among the new substrate alloys in the case of overlay-only coatings. The overlay coating that incorporates a diffusion step did show evidence of potential compatibility issues with the outermost diffusion layer. However, as it is the expectation with any diffusion coating the last step of this coating will require more fine-tuning for each specific system it is applied to. Future work must be done in collaboration with industry so that the variation in microstructure and composition obtained from commercial processes, from one batch to the next, can be quantitatively analyzed. Subsequently, the hot corrosion resistance and overall performance of a given material system can be expressed as a function of the already established commercial variation.

CHAPTER 7: Summary and Future Outlook

7.1 Summary

The goal of this work was to aid in the development of better performing materials for higher operating turbine temperatures by contributing to the understanding of hot corrosion. With that in mind, several efforts were put forth to test and evaluate the hot corrosion resistance of both substrate materials and protective coatings. This section summarizes what was presented in this work and provides some insight to the future of this field.

7.1.1 Sample Assessment Protocol

Prior to any experimentation, it was established that current procedures for the evaluation of hot corrosion attack on burner rig exposed samples are based on antiquated techniques due for an upgrade to match technological advances. Several shortcomings of current sample evaluation procedures were highlighted: only about a quarter of the sample’s interface is accounted for, which might not be representative of the entire sample, and the measurements collected are done so through the approximation of the circumference as a straight line. In addressing the concerns listed, a new way of assessing and analyzing corrosion resistance of cylindrical shaped samples exposed to burner rig experiments was developed. The focus of the new procedure was to obtain high magnification details of the corrosion profile while still retaining information of the sample as a whole, which was achieved through the stitching of multiple high-resolution SEM images. The new protocol proved to deliver more accurate and more complete information regarding the corrosion of burner rig samples. Image processing and analysis was used to extract a one-pixel thick line corresponding to the corrosion profile, which allowed measurements to be performed at every point around the circumference on the sample. This large data pool was used for visualization of the corrosion front, which revealed previously unexplored aspects of the attack, such as overall and local shape, uniformity, tortuosity, etc.

Details regarding the nature of the corrosion attack were made easily accessible through the new sample analysis protocol. It is our goal that results obtained from this type of analysis can aid in the search for improved gas turbine materials as well as in the development of the necessary testing techniques.

7.1.2 Evaluation of New Substrate Materials in Type I Hot Corrosion Conditions

A new nickel-based superalloy and three doped variations were evaluated under type I hot corrosion conditions in a low-velocity burner rig as new substrate materials for turbine blades and vanes. The tests included both long-term and short-term exposures as well as pre-oxidized and bare materials. Minor amounts of hafnium and silicon doping, both individually and combined, affected the initial microstructure of the resulting superalloy both macroscopically and microstructurally.

In its as-processed form Alloy1, exhibited interdendritic segregation with a small fraction of γ-eutectic observed. Its microstructure was composed of highly uniform and cuboidal γ’ precipitates. The addition of hafnium to Alloy1 increased interdendritic segregation evidenced by an increase in the presence of γ-eutectic. On the other hand, the addition of silicon, and hafnium and silicon combined decreased the observed interdendritic segregation. The shape and size of the γ’-precipitates were also affected by each of the different dopants. Hafnium doping results in less cuboidal and slightly smaller precipitates, while silicon doping results in less cuboidal and slightly larger precipitates. The doping of both hafnium and silicon results in less cuboidal precipitates that create highly directional paths in the γ matrix.

During the 500-hour hot corrosion exposure, Alloy1 was not able to form a protective oxide, which resulted in extreme internal sulfidation and hot corrosion attack of this superalloy. The presence of hafnium negatively affected the hot corrosion resistance of Alloy1 by promoting further incorporation of titanium, and tantalum in both the sulfides and oxides formed. Additions of silicon increased hot corrosion resistance through two mechanisms: a) by promoting chromia formation and suppressing the activity of titanium, resulting in a more protective oxide able to slow down internal sulfidation, and b) by promoting a different coarsening behavior of the internal sulfides. Even though it is clear that hafnium and silicon together have a synergistic effect, where the presence of hafnium enhances the effects of silicon and the overall hot corrosion resistance is significantly improved, further work is necessary to establish the specific mechanisms at play.

At shorter exposure times, the trends are similar, with both Alloy1 and Alloy1+Hf showing poor hot corrosion resistance evidenced by oxide delamination and cracking and deep internal oxidation penetrations. On the other hand, both Alloy1+Si and Alloy1+HfSi exhibit good oxide properties and material behavior with small differences between the two. At this early stage, Alloy1+Si has better oxide integrity marked by decreased cracking of the oxide. Given that Alloy1+HfSi exhibited superior hot corrosion resistance during the longer exposure, it is proposed that the mechanisms differentiating the hot corrosion resistance of these two materials come into play during the later stages of attack. More studies are necessary where intermediate times are investigated in order to further understand the bifurcation in their behaviors.

The effects of two pre-oxidation treatments on the hot corrosion resistance of the alloys were also evaluated. In order to measure these effects and compare between alloys, four parameters were chosen for evaluation: oxide thickness, internal oxide penetration, oxide adherence, and distance between vertical cracks. It was found that a short 15-minute pre-oxidation step at 900 °C was beneficial to the hot corrosion resistance of all four alloys. The observed benefits varied from alloy to alloy, but oxide adherence was the most improved parameter across all materials. Increasing the pre-oxidation time to one hour increased the hot corrosion resistance of all four alloys further by enhancing all previously observed benefits. In both cases the best performing alloy was still Alloy1+HfSi.

Further work is needed to fully understand the role of dopants in hot corrosion resistance. The first step is to fully understand the elemental segregation and formation of the $\gamma - \gamma'$ microstructure as a function of dopant. More burner rig experiments where intermediate times are explored are needed to map out the materials' evolution. Lastly, specimens need to be evaluated under more dynamic conditions to fully explore the range of possible turbine environments. This includes, different pre-oxidation times and temperatures as well as implementation of temperature profiles during hot corrosion exposures.

7.1.3 Type I Hot Corrosion Resistance of Diffusion Coatings

The hot corrosion resistance of five substrate-coating material systems comprised of commercially available nickel-based superalloys and diffusion coatings was evaluated. The best performing systems were the platinum aluminide diffusion coatings on two different nickel-based superalloys. Further analysis of these two systems revealed that the different compositions and microstructures of the substrates strongly influenced the overall coating performance when evaluated under type I hot corrosion conditions in a burner rig testing facility.

It was shown that a statistical approach focused on the parametrization and analysis of corrosion profiles can facilitate the matching of physical properties to statistical parameters and therefore improve our understanding of hot corrosion. Based on the data collected through this approach, and supported by phase and elemental analysis, it was proposed that the pin shaped samples with diffusion coatings initially experience swelling that is uniform along the length of the pin, and around the circumference of the pin. The swelling can be explained by the outward diffusion of nickel during the initial stages of exposure. After the initial swelling stage ends, the corrosion-consumption stage begins where the coating material experiences material loss due to corrosion. This corrosion-consumption stage is non-uniform along the length of the pin, with the top experiencing a more exacerbated process, as well as around the circumference of the pin. The height dependency of the corrosion-consumption is attributed to uneven distribution of the salt contaminant in the gas flow, while the non-uniformity around the circumference is attributed to differences in the effective gas flow velocity. Further work is needed to fully understand the relationship between effective gas flow velocity and the enhanced hot corrosion attack observed.

Of the two materials systems evaluated, the system with CM186LC, a DS superalloy, as a substrate experienced exacerbated attack when compared to the system with CMSX-3, a single crystal superalloy, as the substrate. This was attributed to the segregation of refractory elements and formation of TCP phases in the IDZ of the CM186LC system, which hindered the outward diffusion of nickel. Slow nickel diffusion combined with aluminum depletion resulted in a platinum-rich coating more susceptible to phase degradation evidenced by the higher presence of both γ' and martensite phases.

7.1.4 Type I Hot Corrosion Resistance of Overlay Coatings

The hot corrosion resistance of fourteen different substrate-coating systems was evaluated under type I hot corrosion conditions in a low-velocity burner rig. A total of six different coatings were evaluated on a total of nine different substrates, four of which were new candidate materials for improved turbine operations. The best performing system was a platinum-modified CoCrAlY coating on the single crystal CMSX-4. This same coating applied to a CM939 experienced a decrease in performance marked by higher material loss. Closer examination of these two systems revealed differences in the as-processed coatings, with the better performing system exhibiting higher porosity throughout the coating. Due to this discrepancy in microstructures, the source of the differing hot corrosion resistances cannot be isolated and solely attributed to the substrates themselves. Therefore, more work is needed to understand both the presence of porosity and the effect, if any, that different substrates have on the performance of this particular coating. Nonetheless, the difference in IDZ microstructure and performance point to different degrees of coating compatibility that ultimately resulted in different degrees of hot corrosion resistance.

A modified NiCrAlY, although not high performing, was selected for further studies due to its similarity to the second-best performing coating, as well as due to the variation in hot corrosion resistance observed across different substrates. Closer examination revealed that even though all four systems were commercially sprayed with the same coating, two different microstructures were obtained: one fine-grained microstructure with smaller degree of elemental segregation, and one coarser microstructure with increased presence of yttrium rich precipitates. The coating with finer microstructure had enhanced hot corrosion resistance while the coarser structured coating experienced higher material loss and increased inward diffusion of sulfur.

The second-best performing coating was an aluminized modification of the NiCrAlY-mod. The coating applied to three different substrates, showed two different microstructures and levels of hot corrosion resistance. The outer, or aluminized part of the coating, exhibited different microstructures in the as-processed condition, which was attributed to the aluminizing step relying on interdiffusion to form the outermost layer of the coating. It was this difference in the outer layer that ultimately determined the different hot corrosion resistance exhibited by the materials. Two of the three systems formed a protective layered oxide that slowed down the attack. When applied to the new candidate material Alloy1+HfSi, the oxide lacked the layered structure and was not able to prevent the attack.

In summary, although some differences in the degree of material loss were observed between systems that shared the same coating but differed in substrate, there was enough variation in the as-processed microstructure due to potential processing variances that the substrate/coating interaction could not be isolated as the unique source of the different degrees of hot corrosion observed. Furthermore, no significant differences in coating-substrate compatibility were observed among the new substrate alloys in the case of overlay-only coatings. The overlay coating that incorporates a diffusion step did show evidence of potential compatibility issues with the outermost diffusion layer. However, as it is the expectation with any diffusion coating, the last step of this coating will require more fine tuning for each specific system it is applied to.

7.2 Future Outlook

The ever-changing energy needs of our society make the field of turbine materials one of constant evolution and discovery. New technology advancements coupled with better understanding of the turbine environment and materials' requirements has led to an age of highly specialized substrate and coating materials. It is therefore crucial for the advancement of the field to ensure the materials development and testing techniques and protocols are always aligned with not only our energy needs but also our environmental needs.

In this work evaluation and analysis of the type I hot corrosion resistance of new candidate substrate materials was presented. The hot corrosion resistance was evaluated on both bare and pre-oxidized specimens to evaluate the effects of different pre-oxidized conditions. Although type I hot corrosion testing is central to the evaluation of marine turbine materials, it is not enough for current technology. Historically, hot corrosion has been studied and addressed as being either type I or type II hot corrosion. Consequently, industry has developed materials that offer protection for each type of hot corrosion individually, but none that perform under both conditions. Mixed mode testing aims to explore the performance of existing materials when exposed to thermal profiles that cycle temperatures, and therefore cycle between type I, type II and oxidation conditions. Studying materials under this type of dynamic conditions will help further understand the type of degradation observed in field blades and vanes that are removed for inspection whose degradation cannot always be reproduced in the lab. A second burner rig with an improved temperature range and temperature control was developed in order to allow for more dynamic mixed mode testing. During mixed mode exposures, rather than exposing samples to a constant temperature, like in type I conditions, samples are exposed to temperatures as low as 650 °C and as high as 1100 °C all in one cycle. A sample temperature profile is shown in

Figure 62. Furthermore, the specific temperature steps, times at each temperature, heating/cooling rates, etc. are all parameters that need to be explored and experimented with, in order to determine the synergistic effects of mixed mode.

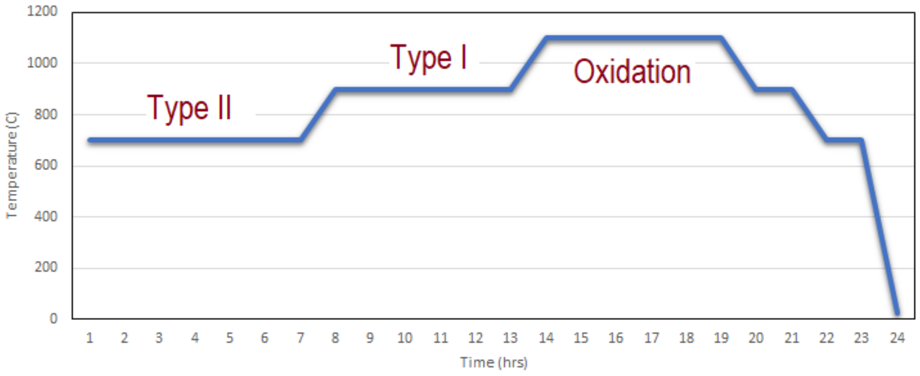

FIGURE 62. Example of a mixed mode temperature profile.

Since mixed mode testing has not been studied in depth before, it is crucial to establish reference points for evaluating mechanisms, rate, and extent of corrosion under mixed mode conditions. A more detailed and more specialized data processing and data analysis method needs to be developed. Evaluating samples under mixed mode conditions is something that has not been done before, making the resulting microstructure and morphology of attack unknown. Without this previous knowledge, data processing of relevant parameters cannot be properly performed. Therefore, relevant information regarding the attack front, nature, shape and extent needs to be identified so that existing data processing and analysis methods can be modified accordingly.

This work also presented a survey of different protective coatings that were evaluated under type I hot corrosion conditions. A big disconnect is often found between academic research, where samples analyzed are frequently produced in a lab under conditions that are often not scalable or practical, and materials development in industry, where the bulk of work is done on performance-based evaluation of commercially produced materials and not on the understanding of such performance. This work tried to bridge this disconnect by performing in-depth analysis of materials systems comprised of commercially processed substrates and coatings. It was found in more than one case that commercially produced materials often result in small variations of either microstructure or composition that can often skew results when doing an in-depth detailed analysis of not only performance, but microstructural and compositional analysis. It is therefore crucial to focus on closing the gap between in-depth analysis of non-commercial systems, and performance-only evaluations of commercial systems. It is proposed that future work should focus on evaluating and understanding the source of variations in commercially processed materials and try to minimize it. This requires a systematic study where casting processes, heat treatments, spraying, and diffusion-based applications used commercially are all evaluated in search for areas that can introduce minor fluctuations to the process and result in small variations in microstructure and/or composition. This study can then help establish a range of microstructures and/or compositions for each material system which can then be used to establish a range of hot corrosion resistance and overall performance for each system. This is an important step in bridging the gap between academia and industry research, because it enables the development of not only improved processing parameters-to-performance correlations but also the understanding behind each performance.

REFERENCES

[1] Y. Niu, F. Gesmundo, F. Viani, et al. The corrosion of Ni_3Al in a combustion gas with and without Na_2SO_4–NaCl deposits at 600–800°C. Oxidation of Metals. 1994.

[2] Budget Item Justification, Office of Secretary of Defense, Department of Defense Corrosion Program, March 2014.

[3] R. Carlin. Total ownership cost reduction. Office of Naval Research Naval S&T Partnership Conference, 2010.

[4] J. Stringer. Hot Corrosion of High-Temperature Alloys. Annual Review of Materials Science 7:1, pp. 477-509, 1977.

[5] R.A. Rapp, Y.S Zhang. Hot corrosion of materials — fundamental studies. JOM, 46 (12), pp. 47-55, 1994.

[6] F.S. Pettit, C.S Giggins. Corrosion of Metals and Alloys in Mixed Gas Environments at Elevated Temperatures. Oxidation of Metals, vol 14, issue 5. pp 363-413, 1980.

[7] D.J. Wortman, R.E. Fryxell, K.L. Luthra, P.A. Bergman. Mechanism of low temperature hot corrosion: Burner rig studies. Thin Solid Films, Volume 64, Issue 2, pp. 281-288, 1979.

[8] Glenn Research Center, National aeronautics and space administration, https://www.grc.nasa.gov/www/k-12/airplane/turbparts.html.

[9] Rolls Royce. The Jet Engine. Wiley 2015.

[10] F.S. Pettit and G. W. Goward, Coatings for High Temperature Applications, Applied Science Publishers, 1983.

[11] R. Bhargava, C.B. Meher-Homji. Parametric analysis of existing gas turbines with inlet evaporative and overspray fogging, Proceedings of ASME TURBOEXPO 2001, Amsterdam, The Netherlands, Paper 2002-30560, 2002.

[12] D.A. Shifler. Hot corrosion: a modification of reactants causing degradation, Materials at High Temperatures, 35:1-3, 225-235, 2018.

[13] D.A. Shifler. The Influence of Fuel Carbon Residue on Hot Corrosion. Proceedings Tri-Service Corrosion Conference January 14-18, 2002, San Antonio, TX, DoD Tri-Service Corrosion Committee, 2002.

[14] D.A. Shifler. Effects of Fuel Dye on the Hot Corrosion Resistance of Marine Gas Turbine Materials. CORROSION/2001, paper 167, NACE International, Houston, TX, 2001.

[15] D.A. Shifler, D.M. Aylor. Considerations for the Testing of Materials and Components in Seawater, CORROSION/2002, paper 217, Houston, TX, 2002.

[16] D.A. Shifler, L.F. Aprigliano, D. Groghan. Evaluating Materials and Fuels Using an Atmospheric-Pressure Low-Velocity Burner Rig: Factors to Consider to Avoid Unintended Consequences. ASME. Turbo Expo: Power for Land, Sea, and Air, Volume 5: Manufacturing Materials and Metallurgy; Marine; Microturbines and Small Turbomachinery; Supercritical CO2 Power Cycles. 2012.

[17] D.A. Shifler, D.M. Russom, B.E. Rodman. Performance Evaluation of High Temperature Coatings for Hot Section Turbine Components. ASME. Turbo Expo: Power for Land, Sea, and Air, Volume 5: Turbo Expo 2005.

[18] A.D. Foster, et al. Fuels flexibility in heavy-duty gas turbines. General Electric Reference Document. GER-3428a

[19] MIL-F-16884L. Military Specification Fuel, Naval Distillate (NATO F-76), (23 October 2006).

[20] MIL-F-16884J. Military Specification Fuel, Naval Distillate (31 May 1995).

[21] MIL-F-16884 N. Military Specification Fuel, Naval Distillate (NATO F-76), (2014 Apr 22).

[22] C. Levi, J. Hutchinson, M. Vidal-Sétif, C. Johnson. Environmental degradation of thermal-barrier coatings by molten deposits. MRS Bulletin, 37(10), 932-941, 2012.

[23] J.A Goebel, F.S. Pettit, Goward. Mechanisms for the Hot Corrosion of Nickel-Base Alloys. Metallurgical Transactions, 4: 261, 1973.

[24] J.A. Goebel, F.S. Pettit. Na_2SO_4-induced Accelerated Oxidation of Nickel. Metallurgical Transactions, Volume 1, Issue 7, pp.1943-1954, 1970.

[25] F. Pettit. Hot Corrosion of Metals and Alloys. Oxidation of Metals 76, 1–21, 2011.

[26] W. T. Reid. External Corrosion and Deposits in Boilers and Gas Turbines, Elsevier, New York, 1971.

[27] A. U. Seybolt, Transactions of the Metallurgical Society of AIME 242, 1955 (1968).

[28] N. S. Bornstein and M. A. DeCrescente, Transactions of the Metallurgical Society of AIME 245, 1947 (1969).

[29] N. S. Bornstein and M. A. DeCrescente, Metallurgical Transactions 2, 2875 (1971).

[30] R. A. Rapp and K. S. Goto, in Molten Salts, eds. J. Braunstein and J. R. Selman (The Electrochemical Society, 9, Pennington, NJ, 1981), p. 81.

[31] R.A. Rapp. Hot corrosion of materials: a fluxing mechanism? Corrosion Science, 44(2), 209–221, 2002.

[32] X. Zheng, Rapp J. Electrochem 1993 2857.

[33] K Lutrha Metall Trans 1982 1647.

[34] K Lutrha Metall Trans 1982 1647.

[35] K Lutrha Metall Trans 1982 1843.

[36] N. Otsuka, R.A. Rapp. Hot corrosion of Pre-oxidized Ni by a Thin Fused Na_2SO_4 film at 900°C. J. Electrochem. Soc., 137 (1), pp. 46-52, 1990.

[37] D.J. Wortman, R.E. Fryxell, Bessen II. A theory for accelerated turbine corrosion at intermediate temperatures. Proceedings of the Third Conference on Gas Turbine Materials in a Marine Environment, Session V, Paper No. 11; Bath, England; 1976.

[38] R. H. Barkalow and F. S.Pettit, On the oxidation mechanisms for hot corrosion of CoCrAlY coatings in marine gas turbines. Proceedings of the 14th Conference on Gas Turbine Materials in a Marine Environment (Naval Sea Systems Command, Annapolis, MD, 1979).

[39] K. T. Chiang, F. S. Pettit, G. H. Meier, in High Temperature Corrosion, NACE-6, ed. R. A. Rapp (National Association of Corrosion Engineers, Houston, TX, 1983), p. 519.

[40] T. Pollock, S. Tin. Nickel-Based Superalloys for Advanced Turbine Engines: Chemistry, Microstructure and Properties Journal of Propulsion and Power, vol.22 no.2 (361-374), 2006.

[41] R. Schafrik, R. Sprague, Saga of Gas Turbine Materials: Part III. Advanced Materials and Processes, Vol. 162, pp. 27–30, May 2004.

[42] J.R. Davis. ASM Specialty Handbook – Heat Resistant Materials. II Series, 1997.

[43] M. Durand-Charre. The Microstructure of Superalloys, Gordon and Breach, Amsterdam, 1997.

[44] F.L. VerSnyder, M.E. Shank. Development of Columnar Grain and Single Crystal High-Temperature Materials Through Directional Solidification, Materials Science and Engineering, Vol. 6, No. 4, pp. 213–247, 1970.

[45] W.R. Freeman, Jr., Chapter 15, Superalloys II, C.T. Sims, N.S. Stoloff and W.C. Hagel, Ed., John Wiley & Sons, p411-439, 1987.

[46] B.J. Piearcey and F.L. VerSnyder, J. Aircr., Vol 3 (No.5), p 390, 1960.

[47] M. Gell. The Science and Technology of Single Crystal Superalloys, Proc. Japan-U.S. Seminar on Superalloys. International Iron and Steel Institute, 1984.

[48] M. Gell, D.N. Duhl, A.F. Giamei. The Development of Single Crystal Superalloy Turbine Bades. Proc. Fourth Internation Symp. on Superalloys. American Society for Metals, pp 205-214, 1980.

[49] J.J Jackson, M.J. Donachie, R.J. Henricks, M. Gell. The Effects of Volume % of Fine γ' on Creep in DS MAR M 200 Hf. Metal Trans. A. Vol 8, 1977.

[50] N. Eliaz, G. Shemesh, R.M. Latanision, Hot corrosion in gas turbine components, Engineering Failure Analysis, vol 9, Issue 1, 31-43, 2012.

[51] R. Sivakumar, et al. High temperature coatings for gas turbine blades: a review. Surf. Sci. Techn., 37, 139-160, 1989.

[52] A.J. Bradley, A. Taylor. An X-ray analysis of the nickel–aluminum system. Proc R Soc Lond.159, 56–72, 1937.

[53] D.K. Das. Microstructure and high temperature oxidation behavior of Pt-modified aluminide bond coats on Ni-base superalloys, Progress in Materials Science, Vol. 58, Issue 2, 151-182, 2013.

[54] J. Angenete, K. Stiller, E. Bakchinova. Microstructural and microchemical development of simple and Pt-modified aluminide diffusion coatings during long term oxidation at 1050 °C. Surface & Coatings Technology - SURF COAT TECH. 176. 272-283, 2004.

[55] G.W. Goward, D.H. Boone. Mechanisms of formation of diffusion aluminide coatings on nickel-base superalloys, Oxidation Metals. 3, 475-494 1971.

[56] B.G. McMordie. Oxidation resistance of slurry aluminides on high temperature titanium alloys, Surf Coatings Technol. 49, 18-23, 1991.

[57] A.J. Rasmussen, A. Agüero, M. Gutierrez, M.J.L. Östergaard. Microstructures of thin and thick slurry aluminide coatings on Inconel 690, Surf Coatings Technol 202, 1479-1485, 2008.

[58] X. Montero, M.C. Galetz, M. Schütze. Low-activity aluminide coatings for superalloys using a slurry process free of halide activators and chromates, Surf Coatings Technol. 222, 9-14, 2013.

[59] P.C. Patnaik, J.P. Immarigeon. High Temperature Protective Coatings for Aero Engine Gas Turbine Components. Aeronautical Note NAE-AN-42, NRC NO 26475, 1986

[60] J.A. Snide, W.J Shulz. Engine Depot Maintenance Repair Technology. AGARD Conference Proceedings No. 317. 1981.

[61] P. Fauchais, A. Vardelle, B. Dussoubs, Quo vadis thermal spraying? J. Therm. Spray Technol. 10, 44–66, 2001.

[62] A. Scrivani, U. Bardi, L. Carrafiello, A. Lavacchi, F. Niccolai, G. Rizzi, A comparative study of high velocity oxygen fuel, vacuum plasma spray, and axial plasma spray for the deposition of CoNiCrAlY bond coat alloy, J. Therm. Spray Technol. 12, 504–507, 2003.

[63] M.T. Pace, R.C. Thomson. Oxidation of MCrAlY coatings on Ni based superalloys, Energy Materials, vol 2, Issue 3, 181- 190, 2007.

[64] K.S. Chan, N.S. Cheruvu, G.R. Leverant, Coating life prediction under cyclic oxidation conditions, Vol. 4 Manuf. Mater. Metall. Ceram. Struct. Dyn. Control. 1997

[65] M. C. Galetz. Coatings for Superalloys, Superalloys, Mahmood Aliofkhazraei, IntechOpen (November 25th 2015).

[66] A.R. Nicoll, et al. 'The effect of alloying additions on M-Cr-Al-Y systems - An experimental study. Thin Solid Films, 95, 21-34, 1992.

[67] J.L. Smeggil J. L. Some comments on the role of yttrium in protective oxide scale adherence Mater. Sci. Eng., 87, 261-265, 1987.

[68] Czech et al. Improvement of MCrAlY coatings by additions of rhenium. Surf. Coat. Techn., 68, 17-21, 1994.

[69] S.R.J. Saunders, J.R. Nicholls. Hot salt corrosion test procedures and coating evaluation. Thin Solid Films. Volume 119, Issue 3, 1984.

[70] W.C. Fang, R.A. Rapp. Electrochemical Reactions in a Pure Na_2SO_4 Melt. J. Electrochem. Soc., 130, 2335, 1983.

[71] M. Zahiri Azar, T. Gheno, B. Gleeson, et al. Initial Stages of Na_2SO_4-Induced Degradation of β-Ni–36Al at 700°C: I-Intrinsic Behavior. Oxid Met, 2017.

[72] P. Steinmetz, C. Duret & R. Morbioli. Laboratory tests for hot-corrosion studies, Materials Science and Technology, 2:3, 262-271, 1986.

[73] G.H. Meier, F.S. Pettit, High-temperature corrosion of alumina-forming coatings for superalloys, Surface and Coatings Technology, Volumes 39–40, Part 1, pp 1-17, 1989.

[74] H. von E. Doering, P.A. Bergman, Construction and Operation of a Hot-Corrosion Test Facility, Materials Research and Standards, 9, No. 9, 35, 1969.

[75] G.C. Booth, R.L. Clarke, Evaluation of Corrosion Resistance of Coated Superalloys in Rig Tests, Materials Science and Technology, v. 2, 272, March 1986.

[76] S. Le Roux, F. Deschaux-Beaume, T. Cutard, P. Lours. Quantitative assessment of the interfacial roughness in multi-layered materials using image analysis: Application to oxidation in ceramic-based materials. Journal of the European Ceramic Society 35, 1063–1079, 2015.
[77] ASD Source. http://www.asdsource.com/source_detail_small/1642/chromalloy_.htm
[78] T.N. Rhys-Jones, Coatings for blade and vane applications in gas turbines, Corrosion Science, Volume 29, Issue 6, pp 623-646, 1989.
[79] E. Lang (Ed.), Role of Active Elements in the Oxidation Behaviour of High Temperature Metals and Alloys, Elsevier, Amsterdam 1989.
[80] D. Young, High Temperature Oxidation and Corrosion of Metals, Elsevier, Amsterdam 2008.
[81] B. A. Pint, Oxid. Met. 45, 1, 1996.
[82] J. Quadakkers, L. Singheiser, Mater. Sci. Forum, 369–372, 77, 2001.
[83] B. Pint, in: W. Gao, Z. Li (Eds.), Developments in High-Temperature Corrosion and Protection of Materials, Chapter 13, Woodhead Publishing in Materials, Cambridge, England 2008.
[84] D. P. Whittle, J. Stringer, Philos. Trans. R. Soc. Lond. 295, 309, 1980.
[85] J. Stringer, Mater. Sci. Eng. A 1989, 120, 129.
[86] S. Chevalier. What did we learn on the reactive element effect in chromia scale since Pfeil's patent?. Materials and Corrosion, 65: 109-115, 2014.
[87] J. D. Kuenzly and D. L. Douglass, Oxidation of Metals 8, 139, 1974.
[88] T. Gheno, B.C. Zhou, A. Ross, et al. A Thermodynamic Approach to Guide Reactive Element Doping: Hf Additions to NiCrAl. Oxid Met, 87: 297, 2017.
[89] H.W. Grünling, R. Bauer. The role of silicon in corrosion-resistant high temperature coatings. Thin Solid Films. Volume 95, Issue, pp 3-20, 1982.
[90] G.R. Krishna, D.K. Das, V. Singh, S.V. Joshi. Role of Pt content in the microstructural development and oxidation performance of Pt–aluminide coatings produced using a high-activity aluminizing process. Mater Sci Eng A. 251:40–7, 1998.
[91] H.M, Tawancy, A. UI-Hamid, N.M Abbas, M.O. Aboelfotoh. Effect of platinum on the oxide-to-metal adhesion in thermal barrier coating systems. J Mater Sci. 43:2978–89, 2008.

[92] N. Vialas, D. Monceau. Effect of Pt and Al content on the long-term, high temperature oxidation behavior and interdiffusion of a Pt-modified aluminide coating deposited on Ni-base superalloys. Surf Coat Technol. 201:3846–51, 2006.

[93] A.L. Purvis, B.M. Warnes. The effects of platinum concentration on the oxidation resistance of superalloys coated with single-phase platinum aluminide. Surf Coat Technol. 146–147:1–6, 2001.

[94] M.W. Chen, M.L. Glynn, R.T. Ott, T.C. Hufnagel, K.J. Hemker. Characterization and modeling of a martensitic transformation in a platinum modified diffusion aluminide bond coat for thermal barrier coatings. Acta Mater. 51:4279–94, 2003.

[95] D. Pan, M.W. Chen, P.K. Wright, K.J. Hemker. Evolution of a diffusion aluminide bond coat for thermal barrier coatings during thermal cycling. Acta Mater.51:2205–17, 2003.

[96] Y. Zhang, J.A. Heynes, B.A. Pint, I.G. Wright, W.Y. Lee. Martensitic transformation in CVD NiAl and (Ni, Pt)Al bond coatings. Surf Coat Technol. 163–164:19–24, 2003.

[97] A.M. Karlsson. On the mechanical response in a thermal barrier system due to martensitic phase transformation in the bond coat. J Eng Mater Technol.125:346–52, 2003.

[98] M. Zielińska, J. Sieniawski, M. Yavorska, M Motyka. Influence of Chemical Composition of Nickel Based Superalloy on the Formation of Aluminide Coatings, Archives of Metallurgy and Materials, 56(1), 193-197, 2011.

[99] S. Hayashi, S.I. Ford, D.J. Young, D.J. Sordelet, M.F. Besser, B. Gleeson, α-NiPt(Al) and phase equilibria in the Ni–Al–Pt system at 1150 °C, Acta Materialia, Volume 53, Issue 11, pp. 3319-3328, 2005.

[100] S. Santra. Phase Stability, Structure and Thermodynamics of Modified Ni- and Fe-Aluminides, Diffusion Foundations, Vol. 13, pp. 1-55, 2017

Appendix A: Direct comparison and accuracy evaluation of sample assessment protocols

In order to properly compare the accuracy of the two sample assessment protocols discussed in chapter 3 samples exposed to two different combustion environments were analyzed using both methods. The combustion environments differed in the type of fuel utilized. The traditional diesel fuel was used for *Condition I*, while a synthetic fuel with higher water vapor was used for *Condition II*. The first combustion environment resulted in uniform attack, while the second environment produced non-uniform deep penetrations. The analysis of varying hot corrosion attack morphologies allows for a better evaluation of the sample assessment protocols.

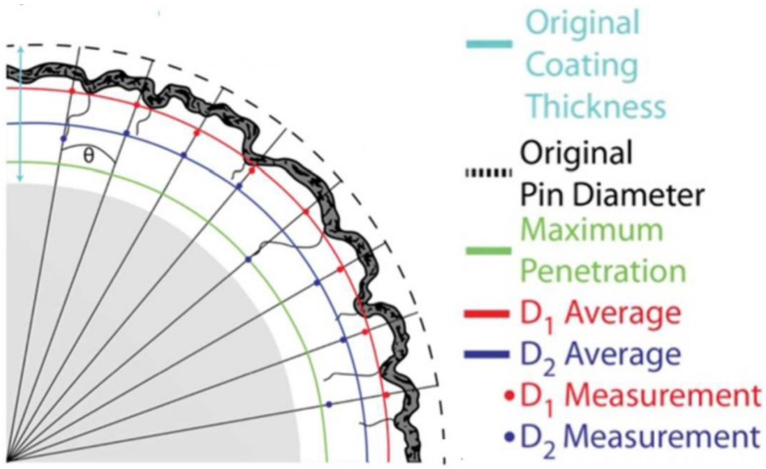

FIGURE A1. Schematic of the different values measured when comparing the two sample analysis methods.

For each sample, and for each analysis method three parameters were obtained. Figure 63 shows a schematic of the parameters measured, and the results are summarized in Table 16. For comparison purposes, and to highlight the differences between individual parameters rather than averages, the values in Table 16 correspond to direct measurements from one cross-section. However, the results presented are representative of all the samples evaluated.

TABLE A1. Summary of sample assessment protocol comparison.

	Condition I		**Condition II**	
	Previous Method	**New Method**	**Previous Method**	**New Method**
Average Radial Loss (um)	7.13	1.9	18.6	14.1
Average Radial Penetration (um)	7.13	6.1	18.6	21.3
Deepest Radial Penetration (um)	13.01	15.8	18.7	38.9

Direct numerical comparisons show that measurements performed through the previous method fail to identify the differences between average radial loss and average penetration values. Results also reveal a large disagreement between methods, emphasizing the fact that unaccounted data (since the previous method only measures 25% of the sample's circumference) can have a significant effect on the final result. Furthermore, not only does the new method provide more accurate numerical values, it also provides enough data to reconstruct and visualize the corrosion attack across the entire sample.

Appendix B: Reconstructed images and corrosion profiles for coating/substrate systems with overlay coatings

An example of a reconstructed backscattered SEM image with its corresponding cartesian plot of the extracted corrosion profile is provided for the five coating/substrate material systems presented in chapter 6 that were not included in the case studies.

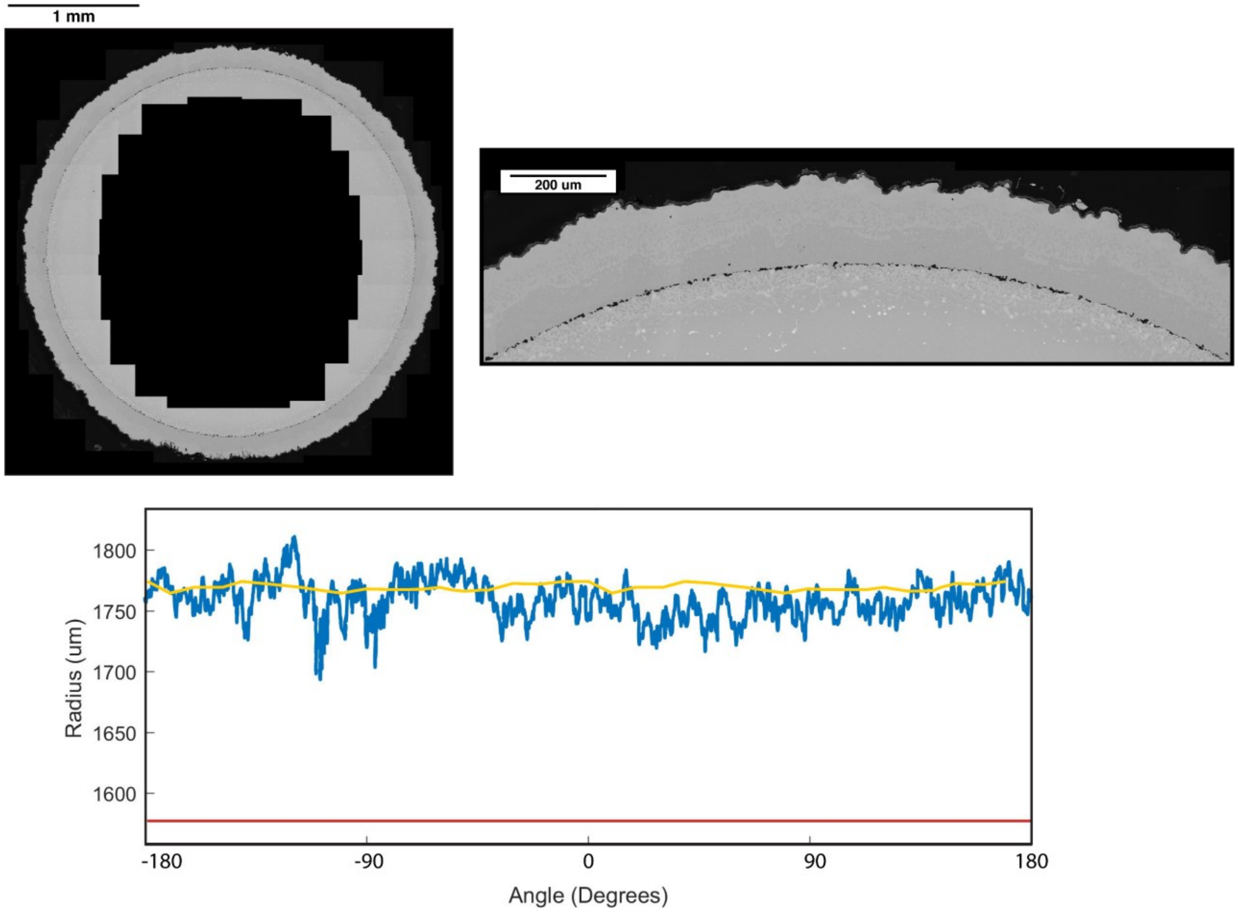

FIGURE B1. Example of reconstructed image and plot of corresponding corrosion profile for the NiCoCrAlY-mod coating on CM939. Extracted corrosion profile shown in blue, sample radius pre-exposure shown in yellow, and substrate/coating interface shown in red.

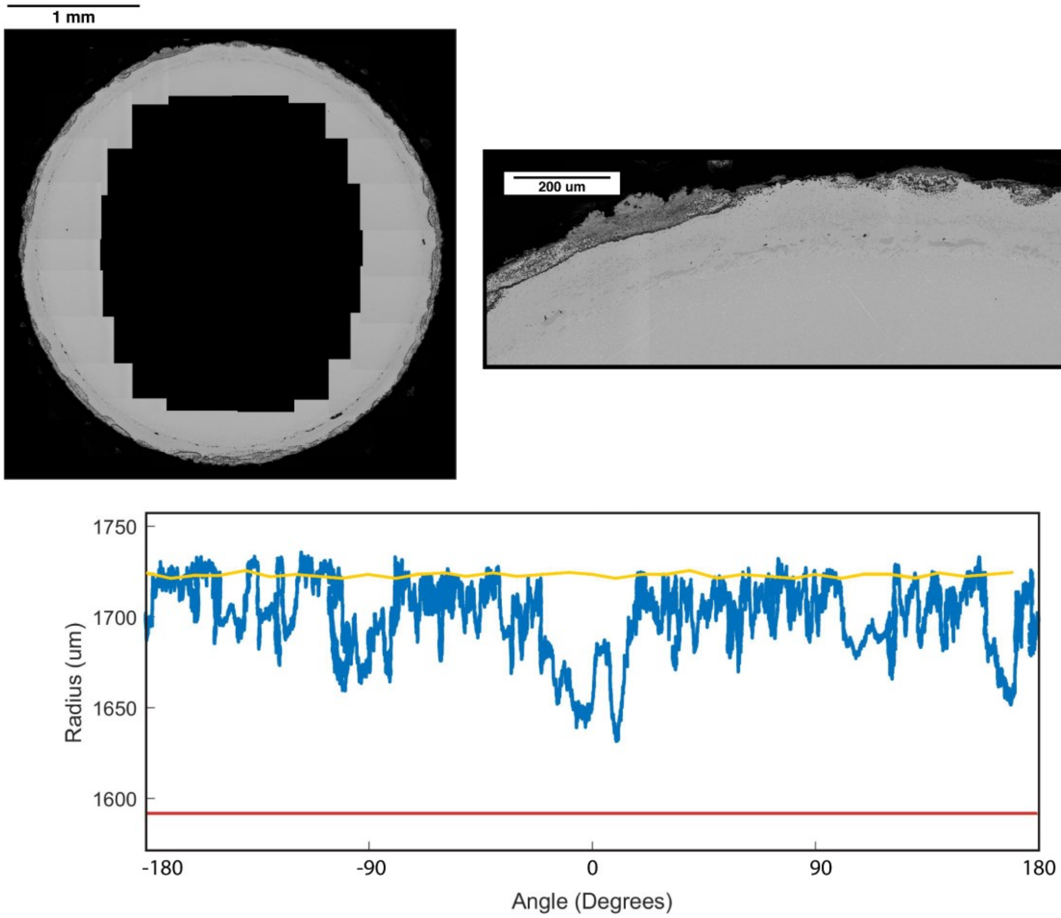

FIGURE B2. Example of reconstructed image and plot of corresponding corrosion profile for the CoCrAlY coating on Alloy-X. Extracted corrosion profile shown in blue, sample radius pre-exposure shown in yellow, and substrate/coating interface shown in red.

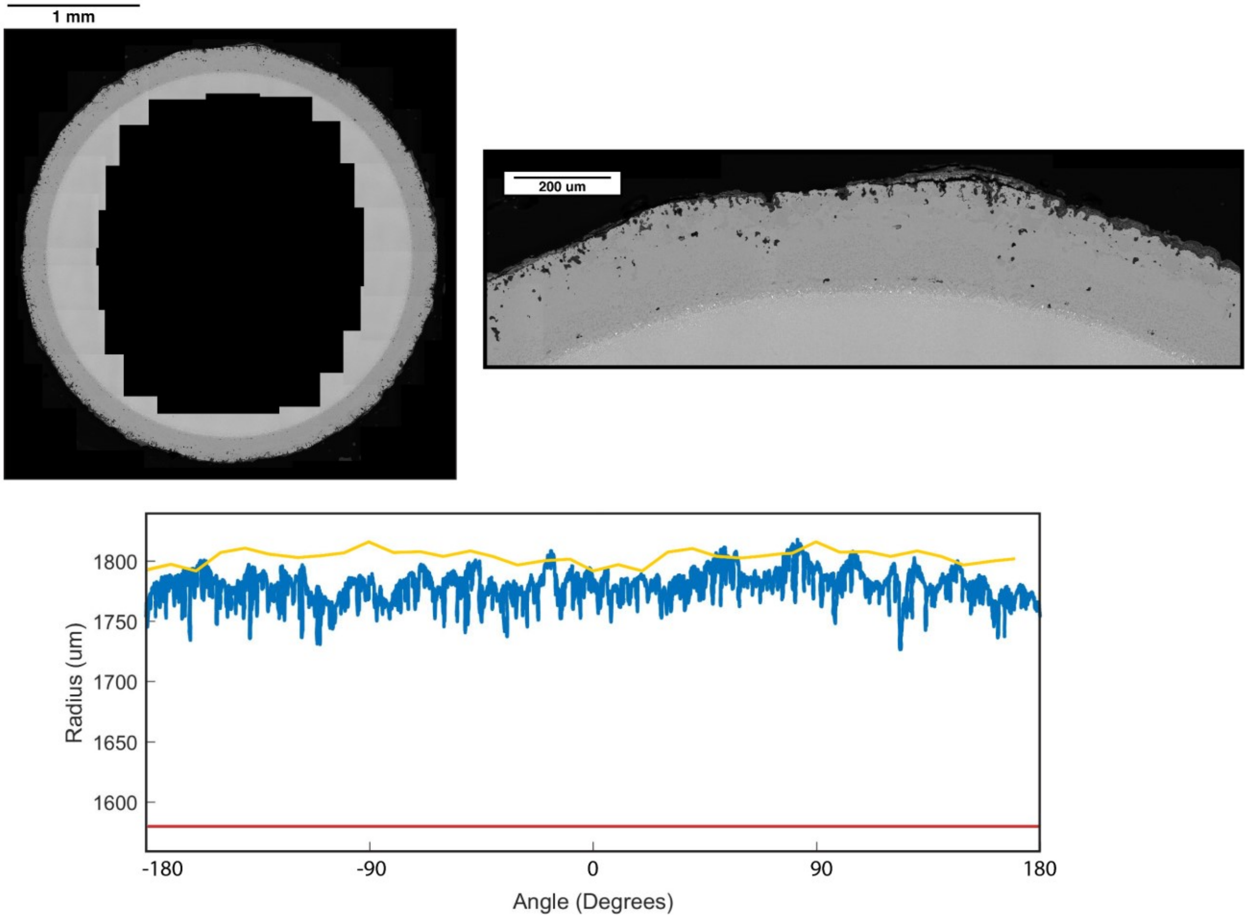

FIGURE B3. Example of reconstructed image and plot of corresponding corrosion profile for the CoCrAlY+Al coating on CMSX-4. Extracted corrosion profile shown in blue, sample radius pre-exposure shown in yellow, and substrate/coating interface shown in red.

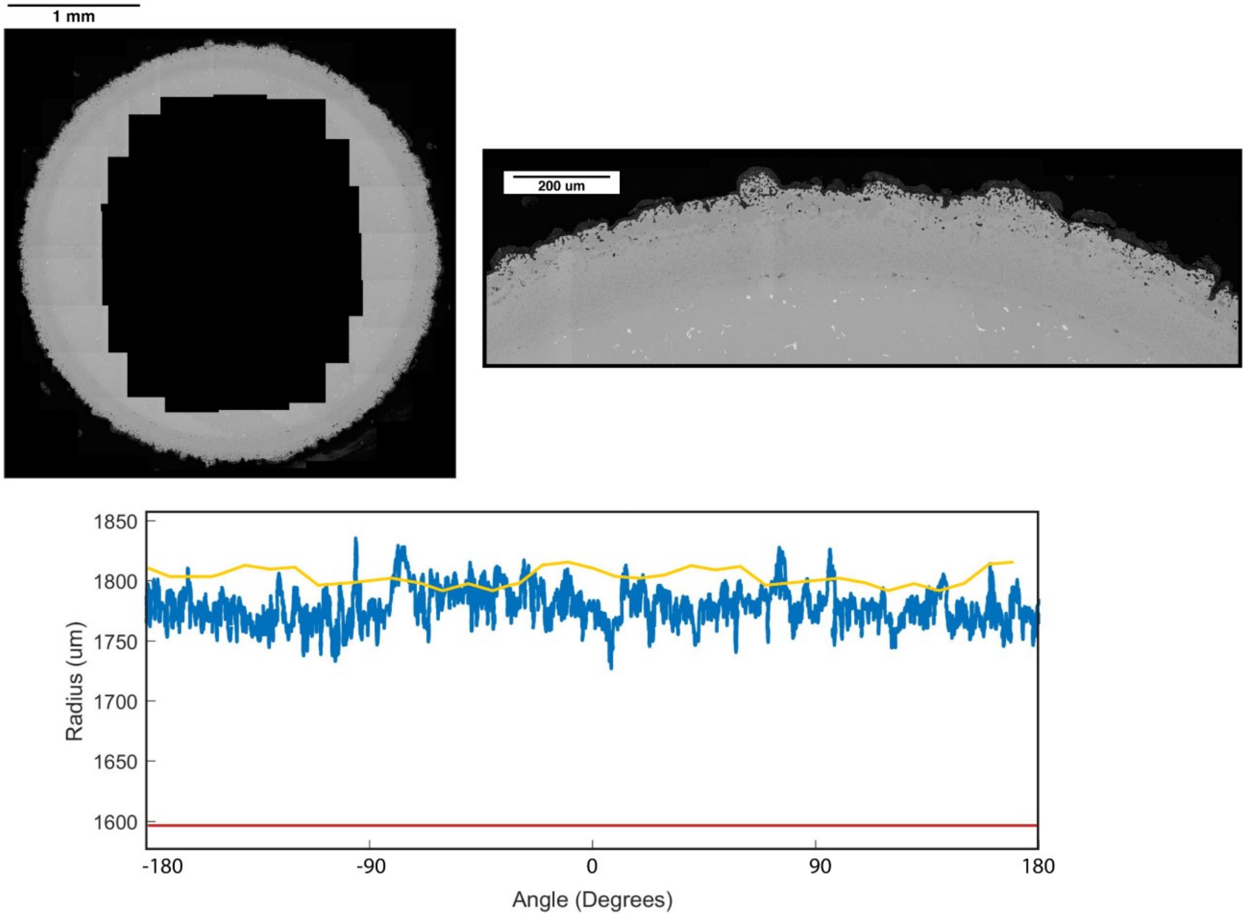

FIGURE B4. Example of reconstructed image and plot of corresponding corrosion profile for the CoCrAlY+Al coating on CM939. Extracted corrosion profile shown in blue, sample radius pre-exposure shown in yellow, and substrate/coating interface shown in red.

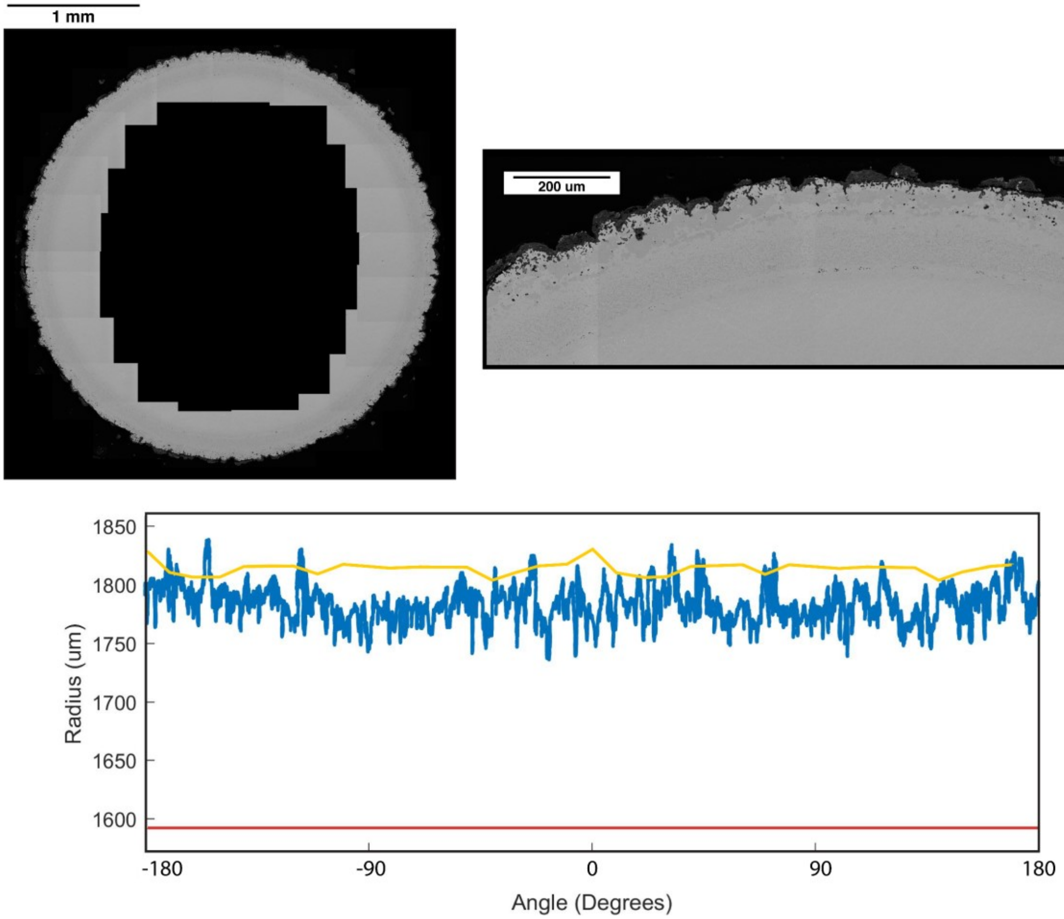

FIGURE B5. Example of reconstructed image and plot of corresponding corrosion profile for the CoCrAlY+Al coating on Alloy-X. Extracted corrosion profile shown in blue, sample radius pre-exposure shown in yellow, and substrate/coating interface shown in red.